TABLE OF CONTENTS

Page

LIST OF TABLES

Page

LIST OF FIGURES

Page

LIST OF ABREVIATIONS AND ACRONYMS

1-D	One-dimensional
3-D	Three-dimensional
AM	Additive manufacturing
APDL	ANSYS parametric design language
BCC	Body centered cube
DMLS	Direct metal laser sintering
DOF	Degree of freedom
ECC	Edge centerd cube
F2BCC	Face centered cube + body centered cube
FE	Finite element
FEA	Finite element analysis
FEM	Finite element method
HEL	Homogeneous equivalent law
HEM	Homogeneous equivalent medium
MT	Martensitic transformation
NiTi	Nickel Titanium
Nitinol	Nickel Titanium Naval Ordnance Laboratory
RVE	Representative volume element
SE	Superelasticity
SLM	Selective laser melting
SMA	Shape memory alloy
SME	Shape memory effect

TKDH	Tetrakaidecahedron
UCFEM	Unit cell finite element method
VC	Vertex cube

LIST OF SYMBOLS

E_A [GPa]	Young's modulus of austenite
E_M [GPa]	Young's modulus of martensite
σ [MPa]	Stress
ε	Strain
σ_{ms} [MPa]	Martensite start stress
σ_{mf} [MPa]	Martensite finish stress
σ_{as} [MPa]	Austenite start stress
σ_{af} [MPa]	Austenite finish stress
ε_L	Maximum transformation strain in Ansys
α	Tension-compression asymmetry
ν	Poisson's ratio
Δ [mm]	Displacement
δ [mm]	Displacement increment
e [mm]	Element size
D [mm]	Strut diameter
T [K]	Temperature
T_0 [K]	Thermodynamic equilibrium temperature
T^* [K]	Effective temperature
M_s [K]	Martensite start temperature
M_f [K]	Martensite finish temperature
A_s [K]	Austenite start temperature
A_f [K]	Austenite finish temperature

ΔH [J]	Enthalpy of transformation
ΔS [J/K]	Entropy of transformation
N	Number of regions in the domain
Φ	Volume fraction of martensite
β [Pa/K]	Clausius-Clapeyron coefficient

INTRODUCTION

Shape memory alloys (SMAs) have been the focus of extensive research in the past few decades. The unique properties of SMAs have made them a suitable choice in a wide variety of industries, including aerospace, automotive, robotics, oil and gas, surgical instruments and biomedical implants (Jani, Leary et al. 2014). These materials exhibit two main behaviors: shape memory effect (SME) and superelasticity (SE), also known as pseudoelasticity. SME is observed when the material recovers its original shape by heating above a certain temperature, after initially being deformed at a lower temperature. SE refers to the ability of these materials to undergo large reversible deformation at a constant temperature. The magnitude of superelastic strains can reach 11% (Duerig, Pelton et al. 1999), which is significantly higher than the elastic deformation of conventional metals such as steel, for which a strain of approximately 0.1% is usually considered reversible. These two characteristics both stem from the crystallographic structure of the material and a process known as martensitic transformation (MT), a diffusionless phase transformation between two crystallographic states of austenite and martensite. The austenite (or parent) phase has a cubic crystal structure, and is stable at higher temperatures, while the martensite phase has a monoclinic crystal structure, and is stable at lower temperatures. The MT can be induced by both temperature variation and stress. The martensite phase can have multiple variants, theoretically 24 of them, marked by austenite-martensite interface planes known as habit planes. In absence of stress, different variants of martensite form a self-accommodating twinned arrangement. In case of stress-induced MT, however, martensite becomes de-twinned under the stress, i.e. it reorients into different combinations of favorable variants, in order to accommodate the applied strain (Otsuka and Wayman 1999, Popov and Lagoudas 2007). This leads to large macroscopic deformation. If the material is heated above a certain temperature, the martensite transforms into austenite, recovering the deformation; this constitutes SME. However, if the material is in austenite phase, it can directly transform to de-twinned martensite phase under stress and transform back to austenite upon unloading, hence, exhibiting pseudoelastic behavior. Figure 0.1 illustrates the schematic phase transformation between these two states.

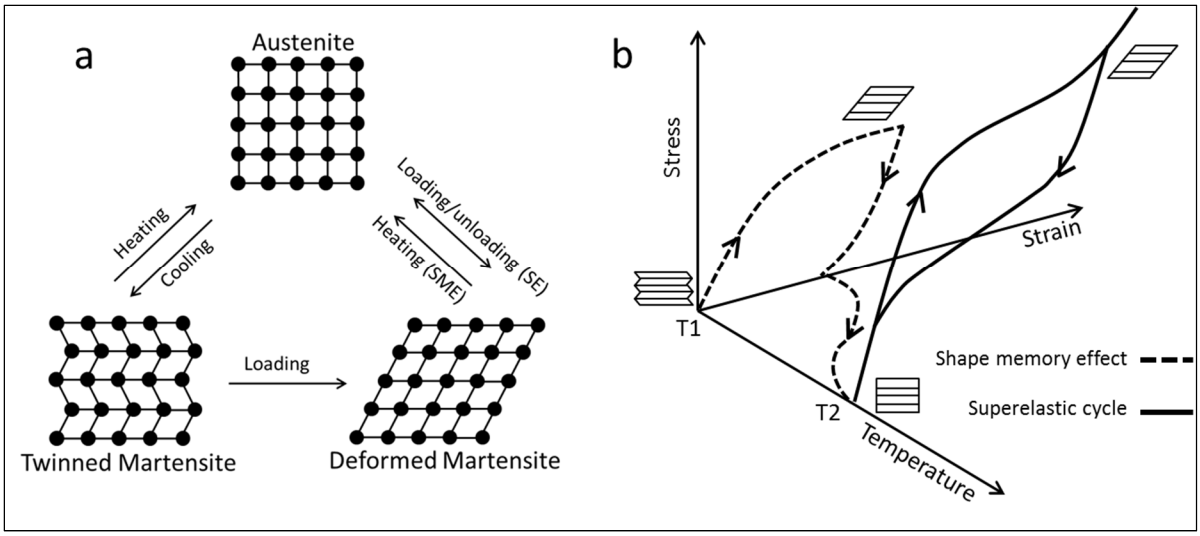

Figure 0.1 (a) Martensite transformation of an SMA, caused by temperature change (SME) or by stress (SE) (b) Stress-strain-temperature curve of SME and SE behaviors

Another feature of some SMAs is their ability to exhibit two-way shape memory effect (TWSME) which, unlike other SMA behaviors, is not and inherent property of the SMA, and is rather acquired through applying special loading cycles or training in a certain temperature range in order to accumulate unrecovered strains in the material. A trained SMA is able to undergo two-way transformations between martensite and austenite, when subjected to temperature changes, hence generating macroscopic strains, without the need for mechanical loading (Cisse, Zaki et al. 2016).

Several types of alloys exhibit shape memory properties, including Nickel-Titanium (NiTi or Nitinol), iron-based alloys, such as Fe–Mn–Si, and copper-based alloys, such as Cu–Zn–Al. Despite their relatively higher cost, NiTi SMAs are the favorite choice in most applications due to their superior thermo-mechanical performance and stability (Wilkes and Liaw 2000, Huang 2002).

SMAs in porous form can offer several benefits that originate from both porosity and SMA characteristics. Metallic foams, in general, have found many applications in a variety of applications and industries, including biomedicine, aerospace, military, transportation,

construction, etc. (Bansiddhi, Sargeant et al. 2008, Bram, Köhl et al. 2011, Smith, Guan et al. 2013). Porous structures can provide many advantages, such as high stiffness to weight ratio, vibration damping, shock absorption and light weight that make them an attractive material choice (Gibson and Ashby 1999, Deshpande and Fleck 2000, K.R. Mangipudi 2010).

One example of the applications where the porous SMAs have attracted a lot of attention is the field of bone implants. A crucial factor in designing a bone implant is its chemical and mechanical biocompatibility. NiTi alloys are usually chosen for biomedical applications because of their chemical biocompatibility on par with titanium and stainless steel (Ryhänen, Kallioinen et al. 1998, Thierry, Merhi et al. 2002). There are some concerns regarding the nickel content of this alloy, as it can leach into the body and cause health problems, but many methods have been proposed to prevent the nickel release, such as different surface treatments. Also, because of the strong intermetallic bond between titanium and nickel, the leaching is minimal and mainly limited to corrosion (Bansiddhi, Sargeant et al. 2008).

As for mechanical biocompatibility, highest possible similarity in mechanical behavior to that of the natural bone is required. Young's modulus, tensile strength, ductility and fatigue life are among the mechanical parameters that need to be adapted for implants (Niinomi 2008). Lack of mechanical biocompatibility usually leads to a common issue concerning the metallic bone implants known as stress shielding phenomenon. This is encountered when the stiffness of the implant is significantly higher than that of the bone tissue, hence making the implant bear most of the stress and leaving the bone tissue unloaded. This in turn results in gradual atrophy of the bone adjacent to the implant and eventually the failure of the implant. Using a superelastic porous material in the implant can address this issue. This is due to the similarity in mechanical response of bone and a superelastic metal (Morgan 2004). Figure 0.2 depicts the schematic behavior of bone, steel and SMA in comparison to each other. Introducing porosity to the SMA will further lower the overall stiffness of the implant closer to the bone tissue. Porosity can also provide the added benefit of an improved osseointegration which is another important factor in effectiveness of a metallic implant. Ideally, the implant should be able to form a strong bond with the surrounding tissue, as many implant manufacturers introduce some form of

porosity to the surface, so that it would promote the ingrowth of bone tissue into the implant (see Figure 0.3). With a good integration between the bone and the implant, the loads can be transferred more effectively and in more distributed manner.

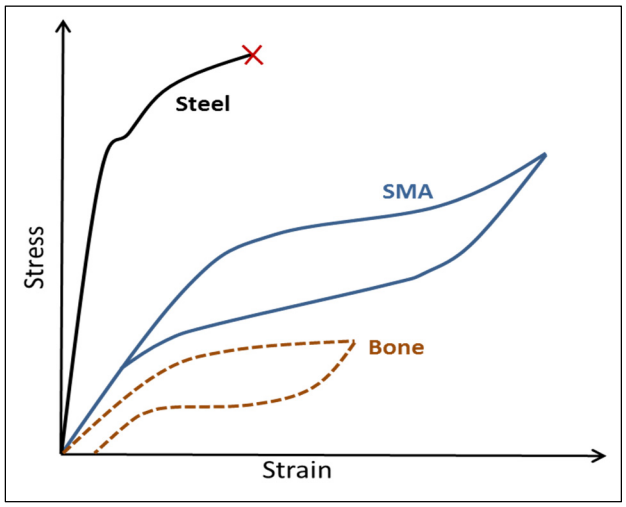

Figure 0.2 Schematic comparison between the mechanical behavior of steel, SMAs and bone

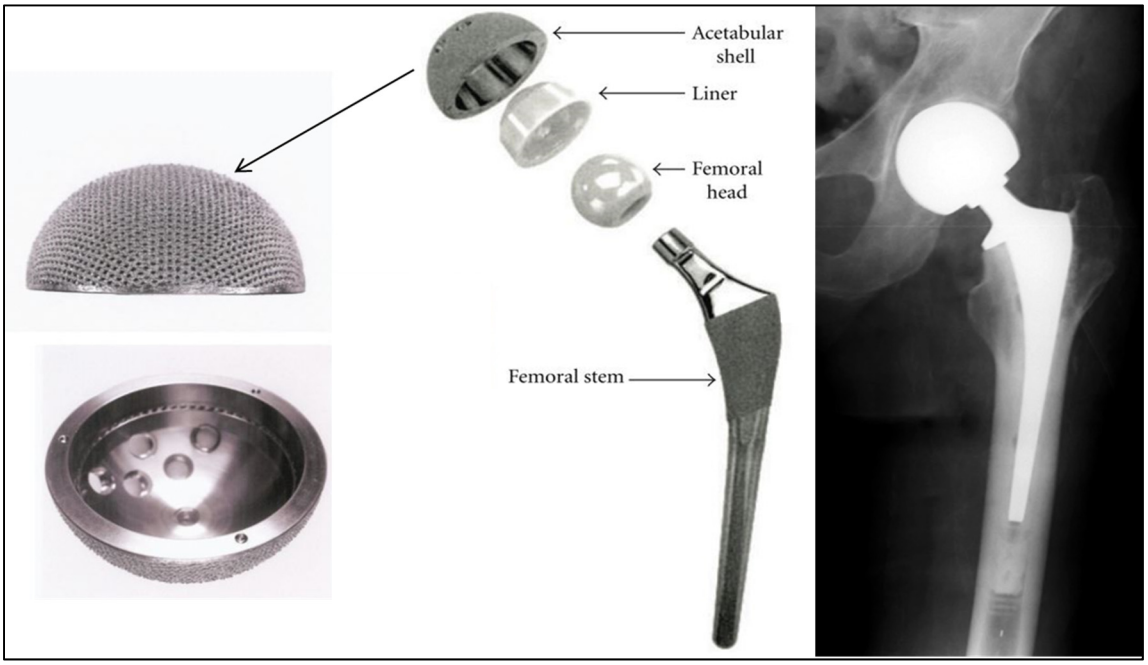

Figure 0.3 Hip replacement implant and addition of porous surface to the acetabular shell and femoral stem for improved bone ingrowth; taken from (Murr, Gaytan et al. 2012)

Thanks to the new additive manufacturing (AM) technologies, such as direct metal laser sintering (DMLS), it is now possible to produce porous parts with more control over their unit cell geometry and porosity level. This has opened the possibility of producing metallic lattice structures according to a specifically designed and optimized geometry in order to achieve the mechanical properties tailored to the requirements of a certain application. For example, producing a customized, biocompatible bone implant will improve the success rate and reduce the chance of failure and related replacement surgery costs. In order to design a porous structure, it is important to model the porous material and obtain an accurate prediction of its mechanical response in macroscale.

It has been shown in the literature that porous SMAs exhibit macroscopic mechanical behaviors, such as superelasticity, similar to dense (non-porous) SMAs (Lagoudas and Vandygriff 2002, Bram, Köhl et al. 2011). However, it is of interest to determine the extent to which a porous SMA would exhibit superelasticity compared to the dense SMA, and what would be the effect of porosity and unit cell geometry.

Based on the provided background, the general objective of this thesis is to analyze and predict the mechanical behavior of additively manufactured lattice structures made of SMAs for the purpose of customizing their macroscopic behaviors. The mechanical properties of such structures are affected by the geometry of the lattice substructure, as well as the constitutive behavior of the SMA material in bulk form. Therefore, both aspects should be taken into account. Considering these facts, three main objectives were pursued in this work which are discussed here.

The first research objective of this thesis is to investigate the mechanical behavior of porous SMAs with respect to dense material and present a modeling and comparison approach for multiple types of SMA lattice structures. Since the additive manufacturing is considered as the target manufacturing method, ordered lattice structures with repeating unit cells will be the focus of this work. As porous parts contain a large number of unit cells, modeling and analysis of the entire structure with all the details requires huge computational resources that makes the

direct modeling impractical. Therefore, most of the proposed modeling approaches in the literature are based on the analysis of the material on mesoscale where a single unit cell (in an ordered porous material) or a limited volume (in a random porous material), containing a group of cells, called representative volume element (RVE), is modelled and analyzed to derive the macroscopic material response. These methods are referred to as mesomechanical approaches (Badiche, Forest et al. 2000). The analysis on the mesoscale can be performed either analytically or numerically. However, due to the significant progress in the computational power, finite element (FE) method has become the preferred numerical method in a majority of applications, especially where the geometry is complex. In this work, FE analyses will be used to simulate and evaluate the mechanical behavior of different unit cells with superelastic material and based on the simulation results, a number of comparisons will be made between the key aspects of the unit cells at different porosities ranging from 10% to 90%. The FE simulations will be performed using the FE software package Ansys 18.2. The properties that will be compared include apparent elastic modulus, maximum recoverable strain, volumetric percentage of material transformation from austenite to martensite, and the energy absorption during the loading and unloading. These comparisons will provide crucial information about the behavior of different types of unit cells with respect to different porosity levels. This information can guide the designer to choose the right unit cell geometry and porosity in order to achieve the required mechanical response.

An important aspect of an accurate FE analysis is utilizing a proper material model. Ideally, a material (or constitutive) model should be able to predict the mechanical response of the material, in terms of stress-strain relationship, as close as possible to the experimental data obtained for that material.

The second research objective is to study the predictive capability of the SMA constitutive model of Ansys, based on the work by F. Auricchio (Auricchio 2001). The material parameters used in this model are obtained from a uniaxial tensile test. This model provides enough accuracy for the purpose of a qualitative comparison of unit cells. However, to ensure a realistic representation of the mechanical response of the FE analyses, one needs to verify the

performance of the material model. To our knowledge, there has not been a direct evaluation of this model's accuracy under more complex loading scenarios, especially when the path-dependency of the material response is considered.

Therefore, the accuracy of the Auricchio's model in predicting the mechanical response of SMAs under multiaxial and path-dependent load cases will be investigated according to experimental data. To obtain the relevant experimental data, a series of uniaxial, as well as path varying multiaxial tests will be conducted on thin-walled NiTi alloy samples at constant room temperature (SE aspect of the material will be focused on). Having obtained the necessary experimental data, an FE model of the test sample will also be created in Ansys and FE simulations will be performed with material parameters, loading sequences and boundary conditions representing the test conditions. The resulting data from both the numerical analyses and the experimental tests will then be compared.

A large number of articles have been published on constitutive modeling of SMAs in the past few decades, see for example (Khandelwal and Buravalla 2009, Cisse, Zaki et al. 2016). But the unusual behaviors of these material makes it challenging to accurately model all their thermomechanical behaviors. There are many important factors that should be taken into account when deriving or choosing a suitable model. Since the material models are usually developed with the purpose of being used in the design and simulation process, it is important to have a model that has the capability of being implemented in an FE software. Therefore, apart from the accuracy of the model in predicting the material behavior, it is also necessary to consider the computational efficiency, robustness and compatibility of the model with FE formulation framework. Other important aspects of constitutive models are the mathematical complexity, the number of parameters, internal variables and material constants involved in the model. Obviously, a constitutive model is more practical if the variables and material parameters are fewer and easier to obtain.

The third research objective is to study an alternative material model that could possibly provide an improved representation of the SMA behavior. Specifically, the model proposed by

V. Likhachev (Likhachev 1995) will be examined in more detail due to its promising features. This model will then be implemented in Matlab and compared with the Auricchio's model. Since this model is formulated in stress-driven format, it is necessary for this model to be adapted to a strain-driven formulation so that it can be incorporated into an FE code. A few approaches will be explored to make this model compatible for FE implementation, including methods for deriving the tangent modulus, a key component for an FE code to update the nodal forces during the simulation.

This thesis is structured in five chapters. After a literature review in Chapter 1, each of the three research objectives will be addressed in a separate chapter. FE analysis of superelastic lattice structures with different unit cell geometries will be presented in Chapter 2. In Chapter 3, the experimental tests and characterization of NiTi material, and validation of the material model in Ansys against the obtained experimental results will be discussed. In Chapter 4, the Likhachev model as an alternative constitutive model and its implementation will be presented. Finally, conclusions and recommendations will be included in Chapter 5.

CHAPTER 1

LITERATURE REVIEW

1.1 Modeling of Porous Metals

In the literature, modeling of porous structures is usually performed on two different scales: mesoscale and macroscale, see Figure 1.1. On mesoscale, the porous substructure is studied, and one or more cells inside a small volume known as representative volume element (RVE) are analyzed. Once the mechanical behavior of this volume is determined, the volume can be treated as a non-porous medium that represents the behavior of porous material. The majority of the proposed modeling methods to simulate porous structures' behaviors are developed on mesoscale and utilize the concept of RVEs. In models developed on macroscale, however, the whole porous structure is analyzed.

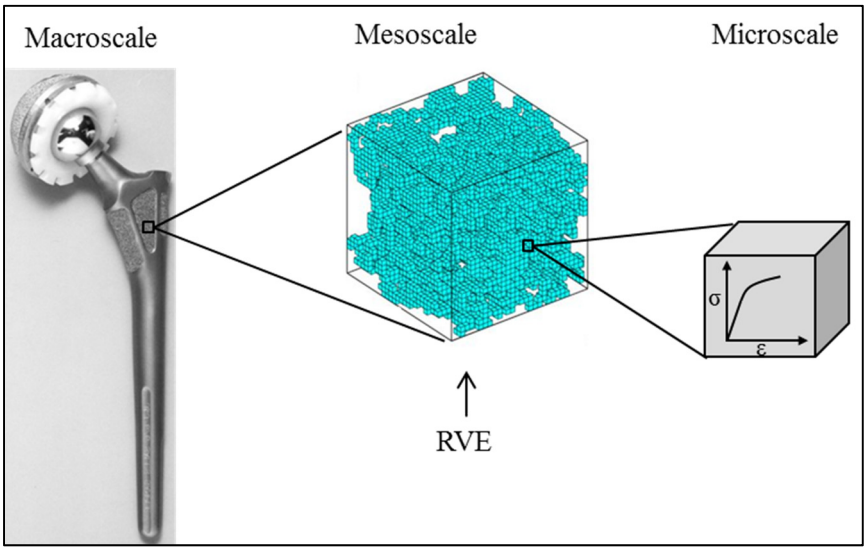

Figure 1.1 Definition of three different scales in this thesis

Based on the substructure arrangement, the porous materials can be divided into two groups of random and ordered substructures, which is also a distinct characteristic in categorizing the modeling approaches. The ordered or regular porous structures consist of identical substructure

units or cells which are repeated throughout the structure. However, in a random porous structure, the underlying cells vary in size and geometry across the domain. Figure 1.2 shows examples of these two porous structure types.

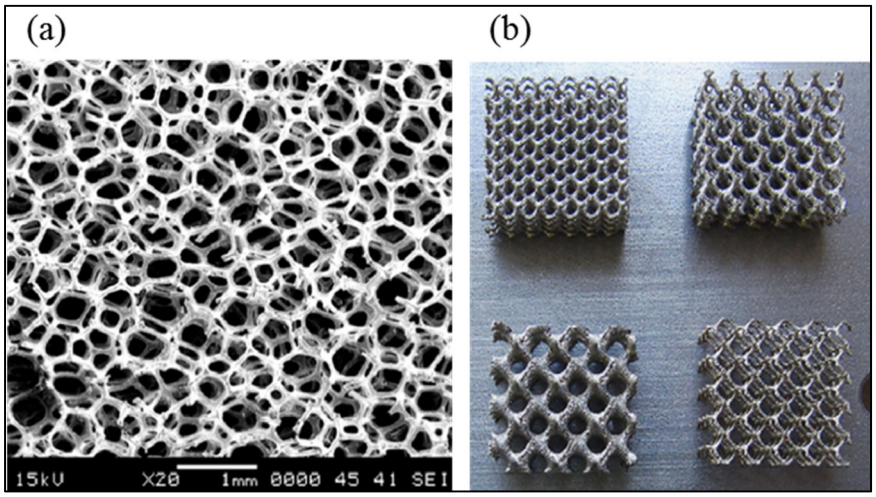

Figure 1.2 Two types of porous structures: (a) random, taken from (Michailidis, Stergioudi et al. 2008) (b) ordered, taken from (Yan, Hao et al. 2012)

The analysis of RVEs can be performed either analytically or numerically, such as the FE method. Most analytical modeling techniques are more suitable in cases where the porous cell structures have a clear and simple geometry, or otherwise are simplified to a degree that can be analyzed analytically. FE analyses, on the other hand, provides a more versatile solution and can be used for complex geometries as well. By performing mechanical analyses, the constitutive relation can be obtained on the mesoscale. Then a homogenization or scaling relation is used to determine the effective behavior on the macroscale. It should be noted that in many papers, the models dealing with porous substructures (on mesoscale) are referred to as micromechanical approaches; see for example (Janus-Michalska and Pęcherski 2003, Choi and Sankar 2005), but in this work, we consider microscale to be on the material level. Figure 1.1 illustrates how three different scales are defined. Other than above-mentioned methods, two other types of modeling approaches are also discussed here, namely, phenomenological methods and direct FE analysis. In the following sections, these methods will be explained.

1.1.1 Analytical modeling of RVEs

The main advantage of analytical methods for determining the mechanical behavior of porous material is the low computational costs. However, a certain amount of simplification is usually necessary to achieve a model that can be handled analytically. This method can be used for both random and ordered structures.

1.1.1.1 Analytical modeling of random structures

In order to model random porous microstructures analytically, it is usually necessary to apply some sort of simplification. In the most simplified approach, a random cellular material can be assumed to be ordered. Janus-Michalska and Pęcherski worked on modeling of open cell foams and used a simplified unit cell in periodic setting. Each unit cell was a tetrahedron containing four beams. Using analytical methods, they formulated the mechanical characteristics of the unit cell based on beam theory and eventually developed relations for the effective behavior of the foam in macro-scale. The key concept of their work was making use of the Kelvin moduli obtained from the unit cell elasticity tensor as a common parameter relating the micro and macro formulations (Janus-Michalska and Pęcherski 2003). Reyes, Hopperstad et al. used an existing constitutive model and applied statistical density variation to model the heterogeneous mass distribution in aluminum foam, and included fracture criteria implemented in a series of FE analyses to validate their model (Reyes, Hopperstad et al. 2003).

Another group of analytical models for random porous materials make use of averaging techniques. Qidwai, Entchev et al. worked on modeling of porous SMAs using micromechanical averaging based on the Mori-Tanaka stress averaging method (Mori and Tanaka 1973) where a random porous structure was treated as a composite material with pores as inclusions (Qidwai, Entchev et al. 2001). Entchev and Lagoudas also did a similar study on porous shape memory alloys with random pore distribution using the Mori-Tanaka averaging method for estimation of the overall stiffness properties (Entchev and Lagoudas 2002, Entchev and Lagoudas 2004). In another work, Zhao and Taya accounted for the pores as inclusions

based on Eshelby's equivalent inclusion method and Mori-Tanaka averaging method (Eshelby 1957, Mori and Tanaka 1973) and formulated relations for the macroscopic behavior (Zhao and Taya 2007). Nemat-Nasser, Su et al. used multi-phase composite model (MPCM) where a porous SMA is treated as a composite with two inclusions, martensite and austenite states, each being either matrix or inclusion, and the pores being the second inclusion (Nemat-Nasser, Su et al. 2005).

1.1.1.2 Analytical modeling of ordered porous structures

Analytical modeling is more commonly used for ordered porous materials due to their straightforward geometry of unit cells. As for open-cell or lattice structures, beam models are usually used whereas for closed-cell structures, plate models are needed. Diebels, Steeb et al. used a micromechanical approach by modelling open-cell foams with beam elements. The homogenized behavior of the material was compared to an existing continuum model (Diebels, Steeb et al. 2003). Florence and Sab investigated the effective mechanical characteristic of a 2D honeycomb periodic lattice microstructure by analytically analyzing a set of beams with elastoplastic formulations (Florence and Sab 2006). Ptochos and Labeas calculated the elastic mechanical characteristics of a 3D body-centered cubic (BCC) lattice structure by modeling the lattice struts as beams (Ptochos and Labeas 2012), see Figure 1.3.

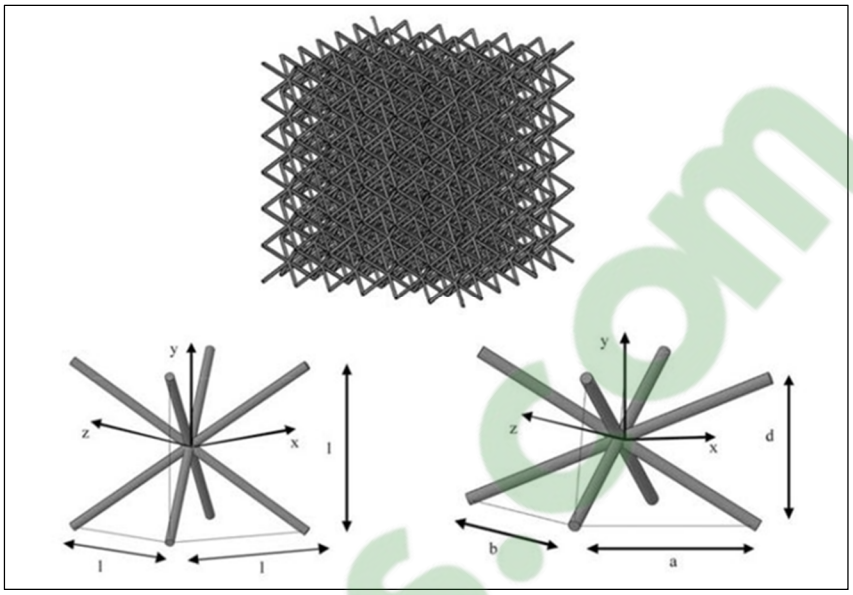

Figure 1.3 Unit cells of a BCC lattice structure made of beams;
taken from (Ptochos and Labeas 2012)

Similarly Ushijima, Cantwell et al. used classical beam theory to determine the yield behavior of a BCC lattice structure (Ushijima, Cantwell et al. 2013). Janus-Michalska used a similar approach for an anisotropic auxetic material which has negative Poisson's ratio due to its mesostructure. In this case, the RVE was first modeled using beam elements, then the strain energy density was calculated in the RVE and was averaged over the volume to derive the stiffness matrix for the macroscopic continuum model (Janus-Michalska 2009).

Plate models are commonly used for analytical modeling of closed cell microstructures. Janus-Michalska proposed a model for a closed cell honeycomb structure. They formulated the constitutive relations for a single cell made of plates based on linear elasticity and homogenized its mechanical response to derive a macroscopic constitutive model. Their model was formulated for small displacements and linear elasticity (Janus-Michalska 2005), see Figure 1.4.

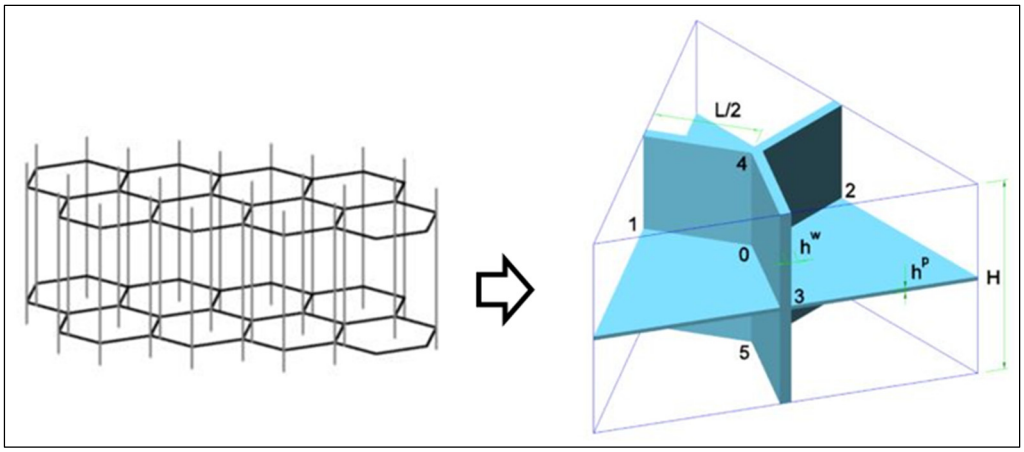

Figure 1.4 An RVE from a closed-cell honeycomb structure modelled analytically; taken from (Janus-Michalska 2005)

In another study, Gotkhindi and Simha derived the shear modulus of pipe stacking structures using theoretical formula such as thin ring and curved beam theory in 2D and used FEA for validation and comparison (Gotkhindi and Simha 2015).

1.1.2 FE modeling of RVEs

FE methods are becoming increasingly popular due to improved computation power in recent years. The process of creating a geometry from the mesostructure for FE analysis is an important step and is always a compromise between the level of details and computational costs. Different FE modeling techniques are categorized in the following subsections.

1.1.2.1 FE modeling of random structures

Since modeling of the real geometry of random porous structures can be laborious and impractical, different alternative numerical techniques are used to provide a simplified microstructure. Simone and Gibson idealized closed-cell foams into simpler geometries of 2D honeycomb and 3D tetrakaidecahedral structures and analyzed them using FEM (Simone and Gibson 1998).

Badiche, Forest et al. suggested a quasi-periodic beam microstructure with Penrose topology for an open-cell nickel foam (Figure 1.5), and analyzed it using FEM, which was able to predict some aspects of the metal foam such as density ratio dependency to the general properties. However, it lacked accuracy in nonlinear cases. In their work, they investigated both micromechanical and phenomenological modeling approaches. A compressible continuum plasticity constitutive model was also suggested where macroscopic test results were used to identify the material parameters. The latter approach provided a better prediction of the mechanical behavior of the nickel foam including its anisotropic behavior (Badiche, Forest et al. 2000).

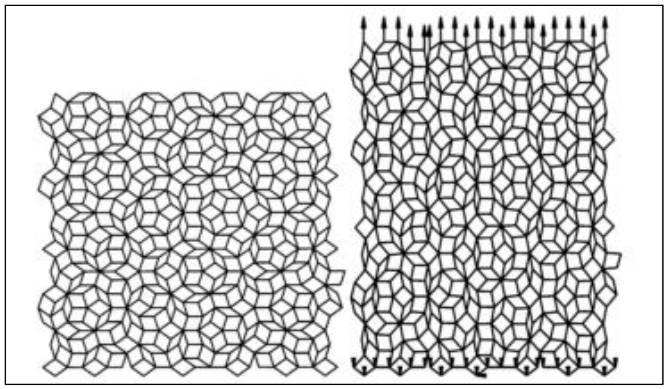

Figure 1.5 Quasi-periodic Penrose Timoshenko beam network and its deformed state in tension for linear elasticity (Badiche, Forest et al. 2000).

In some papers, randomness is introduced into an otherwise ordered geometry. One of the common methods is using Voronoi lattice structures in which the seeding positions can be randomized. Fazekas, Dendievel et al. investigated the impact of the geometry and degree of randomness in 2D Voronoi beam lattices on the effective properties. Different types of disturbances were added to the Voroni network and their effects were examined (Fazekas, Dendievel et al. 2002). Figure 1.6 shows examples of these lattice structures with varying degrees of randomness adjusted through a perturbation coefficient (α).

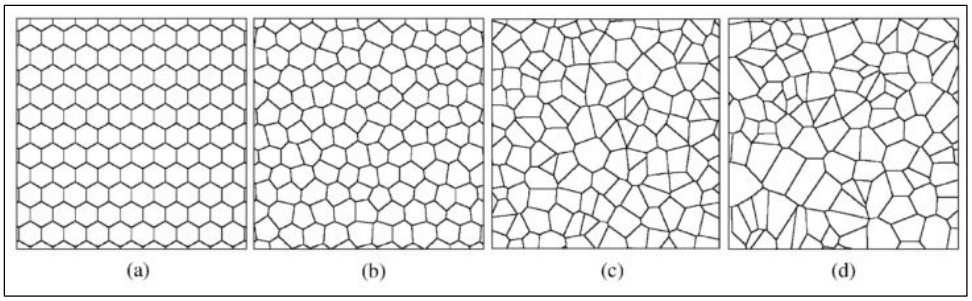

Figure 1.6 Four examples of Voronoi lattices: (a) regular;
(b) perturbation coffcient α =0.2; (c) α =0.5; and (d) fully random
(Fazekas, Dendievel et al. 2002).

K.R. Mangipudi also used random Voronoi beam network to model a metal foam. They developed a multiscale model for plastic hardening of 2D metal foams. In this study, the effect of plastic hardening of the solid material in microscopic scale, as well as the plasticity development in cellular level and reorientation of the struts in mesoscale, were investigated and found to have synergetic effect on the macroscopic strain hardening behavior of the metal foam (K.R. Mangipudi 2010). Betts, Balint et al. used X-ray micro-tomography to import the geometry of an open-cell aluminum foam into FE software ABAQUS. In their work, individual struts were tested and their behavior was used to calibrate the microstructure behavior and its relations to porosity (Betts, Balint et al. 2014).

Regarding 3D FE modeling of closed-cell foams, many idealized models are proposed. Liu and Zhang modeled the mechanical behavior of aluminum foams under compressive loading and suggested an RVE in form of a tetrakaidecahedron, see Figure 1.7. FE analysis was then performed on the RVE model with different mesh refinements, and the stress-strain results were compared with experimental results from Alporas aluminum foam (Liu and Zhang 2014).

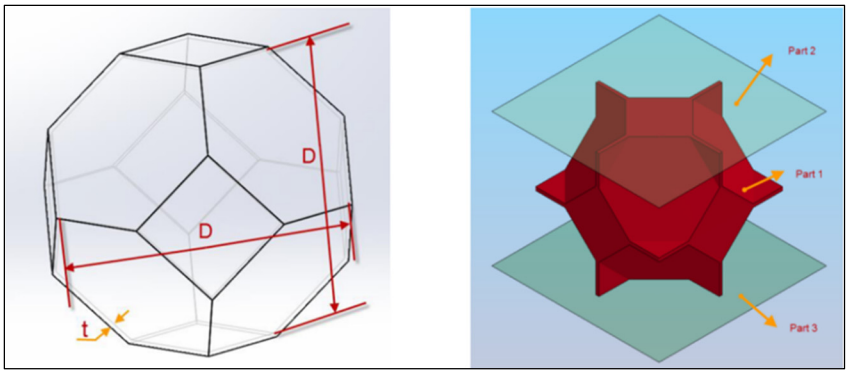

Figure 1.7 A tetrakaidecahedral RVE (Liu and Zhang 2014).

Another way of introducing randomness to an ordered set of cells is by changing the material properties of some of the cells. Panico and Brinson modelled a cubic RVE comprised of structured set of brick elements and randomly assigned negligible stiffness to some elements representing the pores of an SMA foam (Panico and Brinson 2008). Maîtrejean, Terriault et al. performed a number of FE analyses on RVEs with cubic elements and randomly distributed pores (void voxels) in order to determine the mechanical responses, and used scaling relations to replace the dense material model by that of the porous one (Maîtrejean, Terriault et al. 2013). Similarly, Simoneau, Terriault et al. proposed an algorithm to generate RVEs with randomly distributed void voxels based on the geometries obtained from cross-sectional scans of real foams (Simoneau, Terriault et al. 2014), see Figure 1.8.

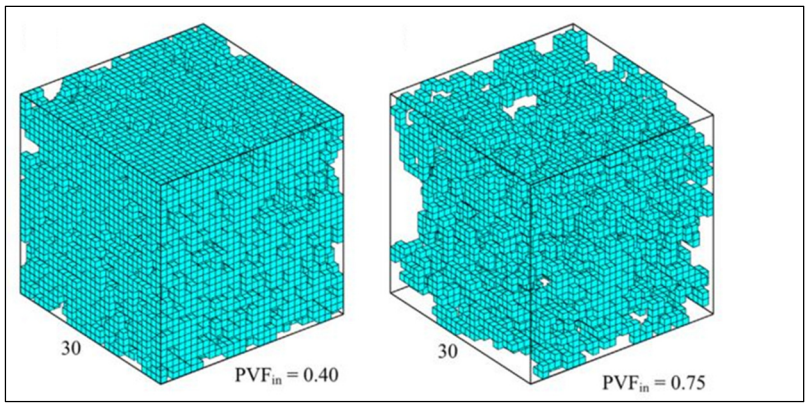

Figure 1.8 RVEs made of voxels representing different pore densities (Simoneau, Terriault et al. 2014).

Foroughi, Degischer et al. used X-ray tomography to scan the random structure of a commercial aluminum foam, but instead of directly reproducing the exact 3D geometry, they defined a continuous domain with variable density/stiffness mapping based on the scanned data. Then the domain was discretized to finite elements (Foroughi, Degischer et al. 2013). Figure 1.9 illustrates the modeling steps.

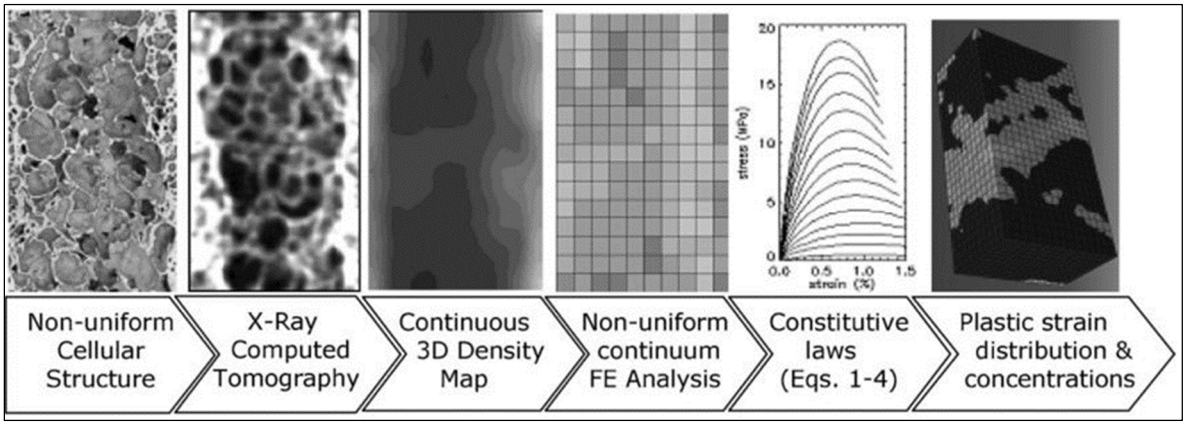

Figure 1.9 Modeling steps proposed by (Foroughi, Degischer et al. 2013).

Sonon, Francois et al. used level set functions to recreate random 3D structures, open- or closed-cell, by different tessellation techniques. They also introduced mesh enhancement approaches for the created geometry. As can be seen in Figure 1.10 their method has the capability of modelling single size, multi size and random shaped pores with different relative densities (Sonon, Francois et al. 2015).

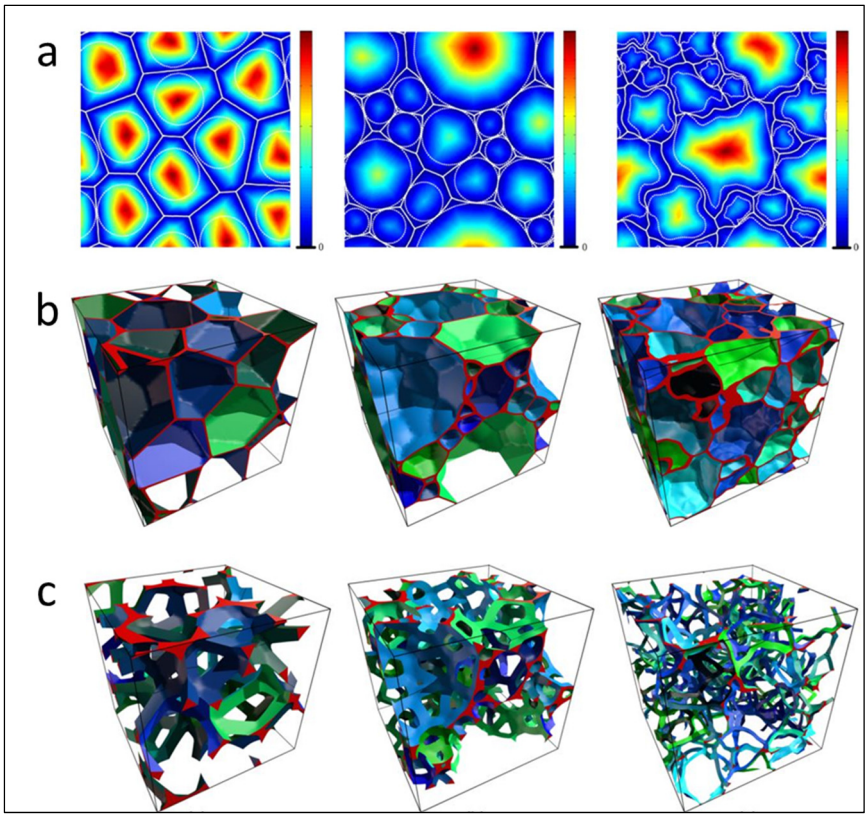

Figure 1.10 (a) Voronoi level set functions for different pore size and shapes (b) closed-cell geometry (c) open-cell geometry (Sonon, Francois et al. 2015).

1.1.2.2 FE modeling of ordered and additively manufactured structures

Ordered porous materials can conveniently be modelled using the FE method. Usually a unit cell or an RVE containing several cells can be modelled to determine the mechanical response. Due to a repetitive microstructural arrangement, periodic or symmetric boundary conditions are usually applied (Terriault and Brailovski 2017). Tsuda, Takemura et al. used FEM to model a periodic unit cell in a plate-fin structure and homogenized the stress-strain relations to the macro-scale (Tsuda, Takemura et al. 2010). Nguyen and Noels worked on the effect of the buckling behavior on the mesoscale and its contribution on the homogenized material behavior. FEA was used for simulation of microstructures in order to account for the bucking on micro-structure level as well as macroscopic scale where they used second order computational

homogenization to determine the buckling behavior (Nguyen and Noels 2014). Iltchev, Marcadon et al. used periodic homogenization method by introducing homogeneous equivalent medium (HEM) for pipe stacking structures with hexagonal and square configurations. A series of uniaxial and multi-axial FE analyses were performed on the RVE with periodic boundary conditions, and based on their mechanical responses, homogeneous equivalent laws (HELs) were identified with anisotropic compressible elastoplastic characteristics (Iltchev, Marcadon et al. 2015), see Figure 1.11.

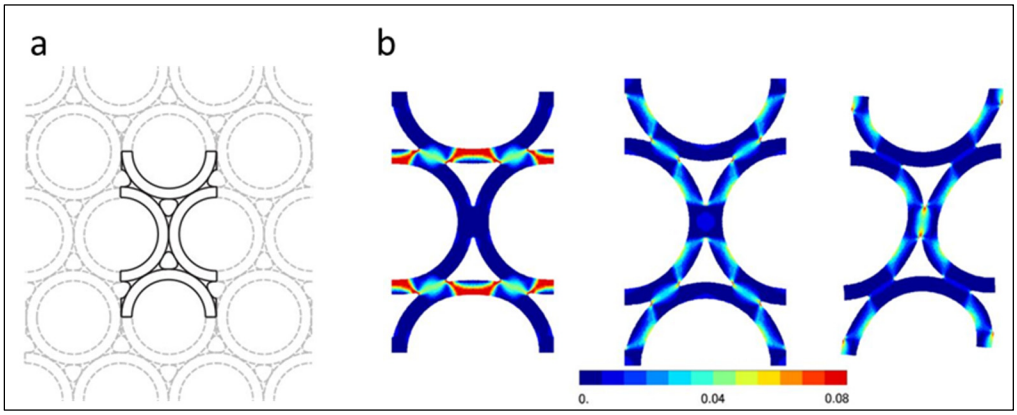

Figure 1.11 (a) Unit cells of the periodic tube stacking with hexagonal pattern (b) FEA results of the unit cell; taken from (Iltchev, Marcadon et al. 2015)

As the additive manufacturing (AM) techniques have become more common in recent years, a wide range of lattice structures with complex topologies can now be produced. Several different unit cell geometries are studied, manufactured, evaluated and characterized in the literature, see for example (Yan, Hao et al. 2012, Koehnen, Haase et al. 2018). However, there are design limitations regarding the manufacturability of lattice structures using AM. To address and navigate these limitations, Kranz, Herzog et al. created design guidelines through experiments to help with the design processes for AM (Kranz, Herzog et al. 2015).

FEM can be used for modelling of 3-D lattice structures with strut components. Smith, Guan et al. (Smith, Guan et al. 2013) studied the effects of different geometrical factors on the mechanical behaviors of two types of lattice microstructures, BCC and BCC-Z, by FE

modeling with continuum and beam elements, and compared the results with experimental values from additively manufactured samples.

It is often useful to evaluate how various mechanical characteristics of unit cells vary with their porosity and geometry. Gibson and Ashby (Gibson and Ashby 1999) derived a scaling relation between the mechanical properties of porous media and the relative density in form of a power law as:

$$\frac{E_p}{E_d} = C\left(\frac{\rho_p}{\rho_d}\right)^2 \tag{1.1}$$

where E_p and E_d, are the Young's moduli of the porous material and dense material, and ρ_p and ρ_d are the densities of porous and dense materials, respectively. This relation was used in a work by Maîtrejean, Terriault et al. where they used FEM to analyze tetrakaidecahedral unit cells with various porosities (Maîtrejean, Terriault et al. 2014). In another work, Egan, Gonella et al. studied multiple strut-based unit cells with varying strut diameters (hence varying porosities) and used FE simulations to determine different properties such as elastic modulus, with respect to porosities (Egan, Gonella et al. 2017). Xiao, Yang et al. used topology optimization to create the optimal geometry and manufacture three different unit cells, namely, face centered cube (FCC), vertex cube (VC) and edge centered cube (ECC) unit cells using selective laser melting (SLM) technology. They performed both FEA and mechanical testing for strength comparison of the unit cells with porosities between 70% and 90% (Xiao, Yang et al. 2018).

In a number of works, the properties of porous structures made of SMAs have been investigated both experimentally and numerically. Andani, Saedi et al. studied three different NiTi unit cells produced by SLM. They tested and characterized the shape memory and superelastic behaviors of the porous structures and compared them to the dense SMA (Andani, Saedi et al. 2017). Qidwai, Entchev et al. also used FEM for spherical and cylindrical unit cell analysis (Qidwai, Entchev et al. 2001). Maîtrejean, Terriault et al. also used SMA material model in their FE

analyses of tetrakaidecahedral unit cell and investigated the volumetric fractions of martensite during the loading. They also showed that better superelastic behavior and be achieved with this particular unit cell compared to a random porous structure.

The architecture of unit cell usually creates anisotropic mechanical behavior in terms of elastic modulus. This is an important feature of the lattice structures that should be taken into account in the design process. Xu, Shen et al. studied different unit cells and used FE analyses to evaluate the stiffness of the unit cell in different orientations and created 3D spatial plots of effective Young's modulus, see Figure 1.12, (Xu, Shen et al. 2016).

Lattice structures produced by additive manufacturing technologies such as Selective Laser Melting (SLM) usually have uneven surfaces and varying strut cross-sections which creates some difficulties in predicting their behavior. To address this issue, Ravari and Kadkhodaei created a detailed FE model of a single strut and introduced imperfections and pores, usually present in real specimens (see Figure 1.13), and determined its stress-strain behavior. Based on the comparison between this behavior and that of an ideal strut, they modified the constitutive model of the bulk material so that an ideal FE model could be analyzed without those imperfections (Ravari and Kadkhodaei 2015).

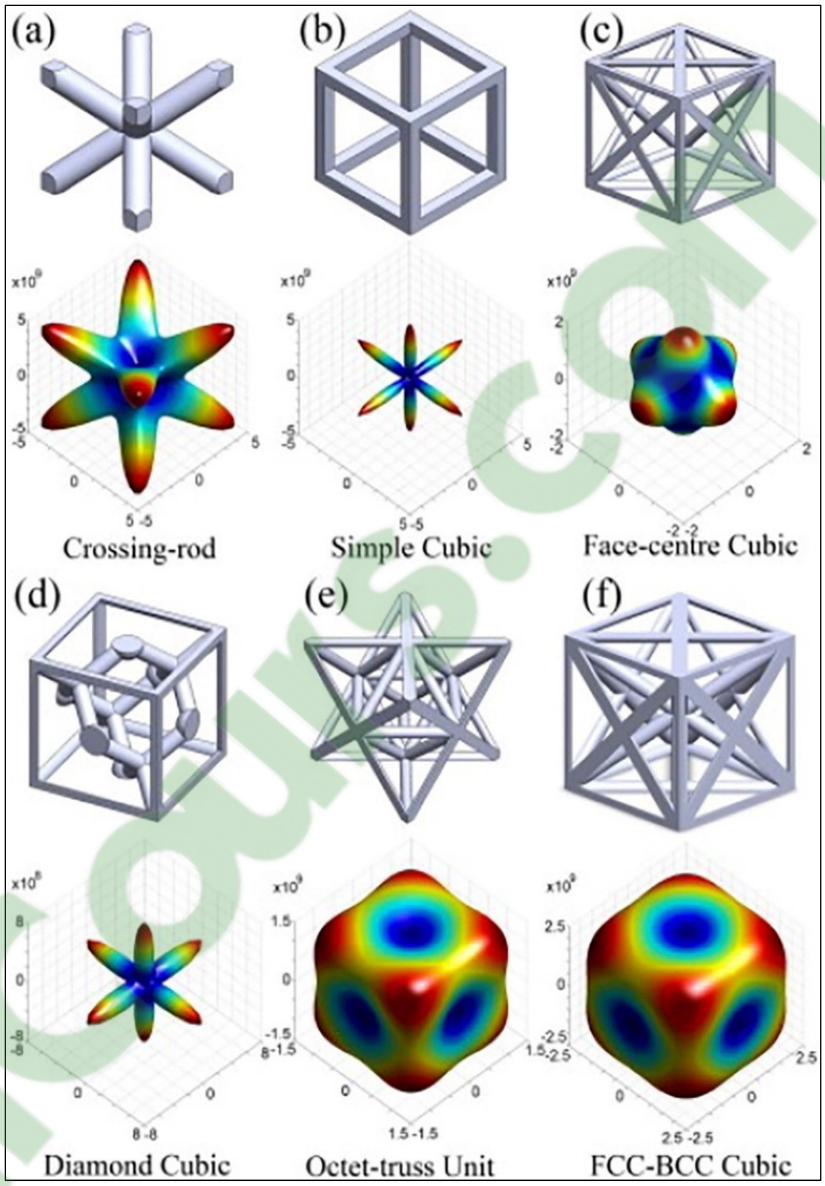

Figure 1.12 3D spatial surface plots representing the effective Young's modulus for various unit cells: (a) crossing-rod unit (b) simple cubic unit (c) face-centered cubic unit(d) diamond cubic unit (e) octet-truss unit (f) a combination of FCC and BCC units
Taken from (Xu, Shen et al. 2016)

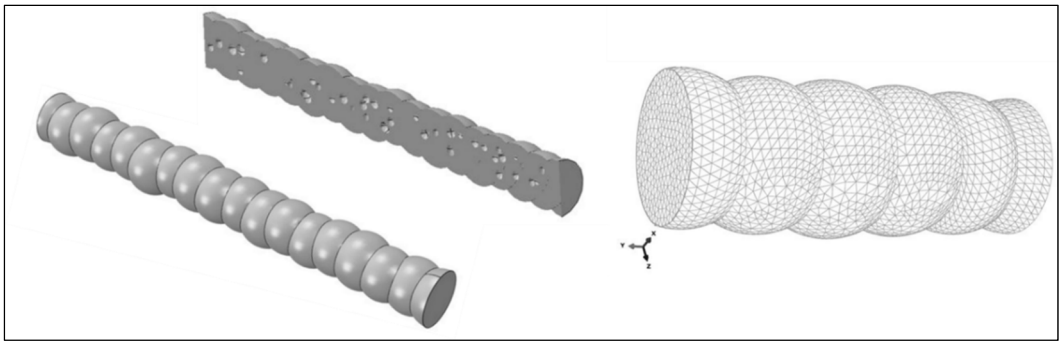

Figure 1.13 Modeling of a single strut with pores and imperfections
(Ravari and Kadkhodaei 2015)

In this work, the behavior of ordered lattice structures with varying porosities will be studied. These types of porous structures are advantageous because the CAD geometry of a single unit cell can easily be designed and adjusted for different porosities and mechanical requirements. Furthermore, this type of periodic structures is more suitable for additive manufacturing. Among the modeling approaches discussed above, there are possibilities of modeling a unit cell either analytically or by using FEA. Analytical approach can only be used when the unit cell is made of slender struts so that the Timoshenko beam theory would be valid, however, this condition will be met only for high porosities. In contrast, FEA can be used regardless of these limitations and for more complex geometries with stress risers, such as sharp corners, can be more accurate.

1.2 Constitutive Modeling of SMAs

The thermomechanical behavior of SMAs can usually be modelled using two different approaches. The first approach takes a macroscopic or phenomenological viewpoint where mathematical formulations are derived in order to directly represent the macroscopic behavior of the material without considering the molecular or crystallographic mechanisms involved in the material response (Paiva and Savi 2006). The second approach is the micromechanical one which deals with the material on the atomic level (microscale) or crystallographic level, including the austenite and martensite phases (mesoscale), and uses a scaling transition to

represent the macroscopic material response. Figure 1.14 illustrates these three scales in the context of material modeling.

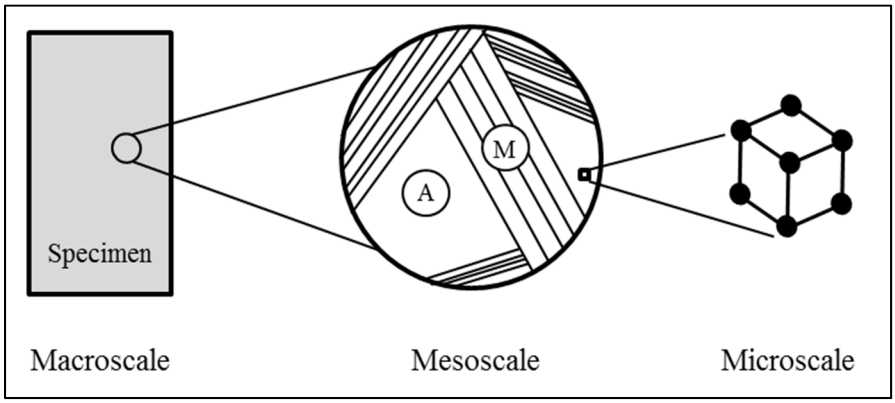

Figure 1.14 Three different scales in material modeling approaches

1.2.1 Phenomenological Models

A majority of published material models use the macroscopic or phenomenological approach where a range of methods are used to capture the overall macroscopic behavior of the material. Many proposed models use the thermodynamic principles and the concept of free energy to derive the formulations.

Panico and Brinson developed a 3D model using a macroscopic approach where the strain was additively decomposed to elastic and inelastic parts and separate expressions for the free energy of the austenite and martensite were proposed. Two internal variables separately accounted for the twinned and detwinned martensite volume fractions. This model was tested in different uniaxial and biaxial settings and was able to reproduce the main SMA features such as SE, SME and martensite reorientation strains. However, the large number of internal variables and material parameters makes this model complex. This model is stress-driven, meaning that it cannot directly be implemented in an FE software (Panico and Brinson 2007). In a later work, the same authors implemented the model in ABAQUS FE software where an iterative routine was used to match the stress with the applied strain (Panico and Brinson 2008).

Similarly, Popov and Lagoudas proposed a model with 3D capability accounting for transformation from both austenite and twinned to detwinned martensite. Gibbs free energy was devised for austenite, martensite and the mix. Three internal variables governing the phases, as well as 16 different material constants were introduced (Popov and Lagoudas 2007). Being a stress-driven model, the authors used the "closest point projection algorithm" from (Qidwai and Lagoudas 2000), a form of return mapping algorithm, and implemented the model in an FE program. Although this model is able to represent the main characteristics of SMAs such as SME and superelasticity, there are some disadvantages, such as lack of experimental validation, complex set of parameters and potentially high computational cost.

In another work, Chemisky, Duval et al. presented a phenomenological model based on thermodynamic potentials. Their model was able to model the martensite transformation, reorientation of martensite under stress and twinning or self-accommodation of the martensite. The latter mechanism is associated with the apparent change of modulus between austenite and twinned martensite. They also made use of the concept of path-dependent transformation strain which enabled the model to reproduce tension-compression asymmetry. This model was suitable for low stresses only (Chemisky, Duval et al. 2011).

(Evangelista, Marfia et al. 2010) suggested a 3D phenomenological model based on the finite strain theory capable of predicting both SE and SME. To implement in an FE code, return-mapping procedure was used in order to comply with the strain-controlled framework of FE formulation. The model presented a variety of predictions of the SMA behavior, but no experimental data was provided to validate the accuracy of the results.

Some macroscopic models are based on the theory of plasticity and formulations, such as flow rules and loading functions, are used to describe SMA-related processes (Cisse, Zaki et al. 2016). Lagoudas, Bo et al. used Gibbs free energy function accounting for volumetric martensite fraction and presented a transformation function analogous to a yield function from the theory of plasticity (Lagoudas, Bo et al. 1996). Also, the model by Auricchio, Taylor et al. was developed base on the generalized plasticity theory where the inelastic transformation

strains were treated as plastic deformation. This model was able to reproduce a few SMA behaviors such as superelasticity, martensite reorientation and tension-compression asymmetry. However, shape memory effect could not be modelled by this formulation. Due to simplicity of this model, only few material parameters needed to be determined and the only internal variable governing the transformation was the volume fraction of the single-variant martensite. A material parameter also defined the tension-compression asymmetry behavior. This model was later incorporated into the Ansys FE software package as a material routine based on a later paper by the same author (Auricchio 2001) where its robust performance was exhibited by different numerical simulations.

1.2.2 Micromechanical Models

The microscopic or mesoscopic approaches rely on describing the SMA features at microscale or mesoscale, and then use an averaging technique to derive macroscopic formulations. These models have been explored by a number of authors. Fischer and Tanaka used the concept of a microregions, smallest possible region in the material capable of being either martensite or austenite, and mesoregions containing several microregions, and used an averaging technique to derive the macroscopic material model (Fischer and Tanaka 1992). Comstock Jr, Buchheit et al. studied the phase transformation of constrained single SMA crystal and its anisotropic behavior in order to understand the characteristics of a randomly arranged polycrystalline SMA (Comstock Jr, Buchheit et al. 1996). In another work by Lu and Weng, the stress-induced martensitic transformation of a single NiTi crystal and its inherent anisotropic transformation strain was determined using invariant plane strain theory, and used to predict the polycrystalline stress-strain behavior through directional averaging (Lu and Weng 1998). Similarly, Šittner and Novák used simple stress averaging over a number of regions, each with their own orientation. They used crystallography and thermodynamics to obtain the transformation strain characteristics of a single grain in the domain (Šittner and Novák 2000). Another interesting model was proposed in a work by Likhachev. The central concept of his model is the introduction of an effective temperature based on the Clausisus-Clapeyron relation and defining a kinetic rule that governs the evolution of the both direct and reverse martensite

transformations, characterized by the four transformation temperatures of M_s, M_f, A_s and A_f. This model also takes into account the crystallographic orientation of the martensite crystals by dividing the domain into a number of regions with different orientations. As with most micromechanical methods, the macroscopic quantities of the SMA are achieved through an averaging technique. This model has the ability to predict most SMA behaviors, such as SE, SME, TWSME, stress generation and material degradation during cyclic loading. This model also uses only a limited number of material parameters that are easy to determine through experimental tests (Likhachev 1995).

Here, Likhachev's model will be investigated in more detail. One important aspect of SMA material models is their capability of capturing multiaxial path-dependent behavior of the SMA. Since Likhachev's model takes into account the existence of multiple regions with different crystallographic orientation, it is possible that this behavior of the SMA can be represented more accurately. Also, the material parameters needed to define this model are much easier to determine through experimental tests, which is not usually the case with most of other phenomenological models. Both simplicity and versatility of this model in representing all major SMA related material behaviors, makes this model a good candidate to investigate in further details.

1.3 Objectives

As mentioned in the Introduction, the main goal of this thesis is to analyze, model and predict the behavior of ordered porous structures made of SMA materials in order to facilitate customization of their design to match specific mechanical requirements. The literature review in this chapter helps us to lay out three specific objectives to achieve this goal. The objectives are:

1. Perform finite element analyses on various SMA unit cells with porosities ranging from 0 to 90%, and investigate the influence of unit cell geometry and porosity on key mechanical parameters.

2. Experimentally validate the material model used in the current FE software and to determine if this model is capable of predicting more complex behaviors of the SMA materials.
3. Investigate an alternative material model that can possibly provide improvements upon the current material model in the commercial FE programs.

CHAPTER 2

FINITE ELEMENT ANALYSIS OF SUPERELASTIC LATTICE STRUCTURES

The progress in additive manufacturing technologies has provided more freedom in terms of designing complex geometries for periodic lattice structures. As a result, the topology and porosity of the unit cell can be tailored for certain mechanical requirements.

Unit cell finite element method (UCFEM) is an effective tool in predicting the macroscopic mechanical response of this type of lattice structures. Due to periodicity and symmetry of designed lattice structures, it is sufficient to model and analyze only a single unit cell or even a fraction of the cell, provided that proper boundary conditions are utilized. This method has been used in a number of research papers such as (Qidwai, Entchev et al. 2001, Maîtrejean, Terriault et al. 2014, Xu, Shen et al. 2016). A comparative study of the mechanical properties of superelastic lattice structures and their dependence on unit cell geometry and porosity level is lacking in the literature. To address the first research objective pointed out in the Introduction, in this chapter, five commonly used unit cell geometries, namely, spherical, tetrakaidecahedron (TKDH), diamond, F2BCC and BCC were modelled and analyzed using the FE method in order to determine their mechanical behavior and compare their properties at varying porosities from 0 to 90%.

Through FE analyses of five different unit cells, the following data were extracted and compared against porosity level:

1. Extent of recoverable superelastic strain that each unit cell can exhibit,
2. Apparent initial elastic modulus (E_A),
3. Volume fraction of austenite, martensite and mixed phases during the loading process,
4. Amount of strain energy absorption and dissipation during loading and unloading.

2.1 Methodology

2.1.1 Geometries

The unit cells geometries were mainly created using Ansys Parametric Design Language (APDL). In some cases, Ansys Workbench was also used to create complex features which will be discussed later. One spherical and four strut-based unit cells were created. The spherical unit cell is comprised of a cube with 1mm length and a spherical pore in the center. Its porosity was adjusted by changing the pore diameter. This unit cell is a special case because it is a closed-cell lattice structure for low porosities, but it becomes an open-cell type as the diameter of the pore exceeds the length of the cube. Due to the symmetry of the geometry, only one-eighth of the unit cell needs to be modelled. Figure 2.1 shows the geometry for both the open-cell and closed-cell topologies.

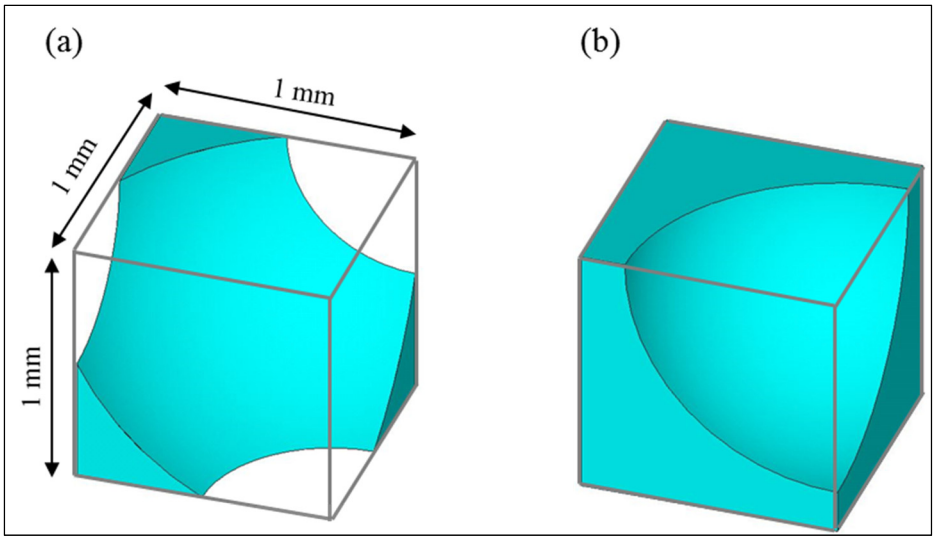

Figure 2.1 CAD geometry of spherical unit cell: (a) 70% porosity, open-cell (b) 30% porosity, close-cell

As for the strut-based unit cells, the struts were created with circular cross-section, and their lengths were kept at a constant value of 2 mm for all unit cells. The diameter of the struts was

then adjusted in order to achieve the desired porosity values. The size of the box containing the unit cell was determined by the topology of each unit cell.

Diamond unit cell is made of 12 struts of equal lengths L. The dimensions of the box encompassing the struts are $\sqrt{8/3}$ L $\times \sqrt{8/3}$ L $\times \sqrt{16/3}$ L (Terriault and Brailovski 2017). Figure 2.2 illustrates the schematic topology and the CAD model of the unit cell for a porosity of 70%. This unit cell has mirror symmetry along x and y axis, and translational symmetry along the z axis in the coordinate system shown in this figure.

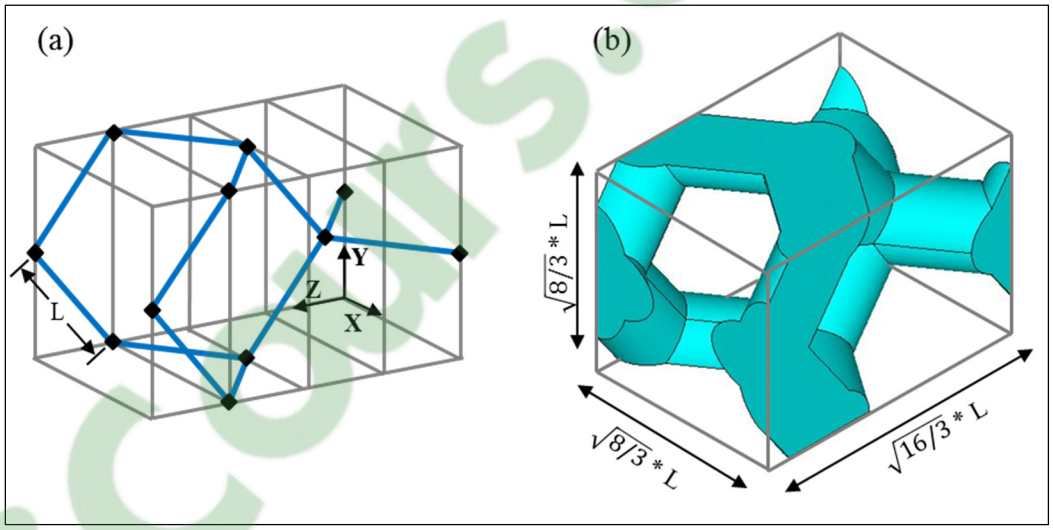

Figure 2.2 Diamond unit cell: (a) schematic topology (b) CAD geometry with 70% porosity

Tetrakaidecahedral lattice structure, also known as the regular truncated octahedron, is a common geometry studied in many publications (Zhu, Knott et al. 1997, Michailidis, Stergioudi et al. 2008, Sullivan, Ghosn et al. 2008, Thiyagasundaram, Wang et al. 2011), and can be used to closely model some types of open-cell natural tissues or metallic foams. TKDH structures also provide the minimum surface area to volume ratio (Gibson and Ashby 1999) which can be useful in some applications. The geometry of the unit cell is made of identical struts making up eight equilateral hexagons and six squares. As can be seen in Figure 2.3, the

TKDH unit cell is symmetric in X, Y and Z directions, therefore only one-eighth of it can be modeled for FEA.

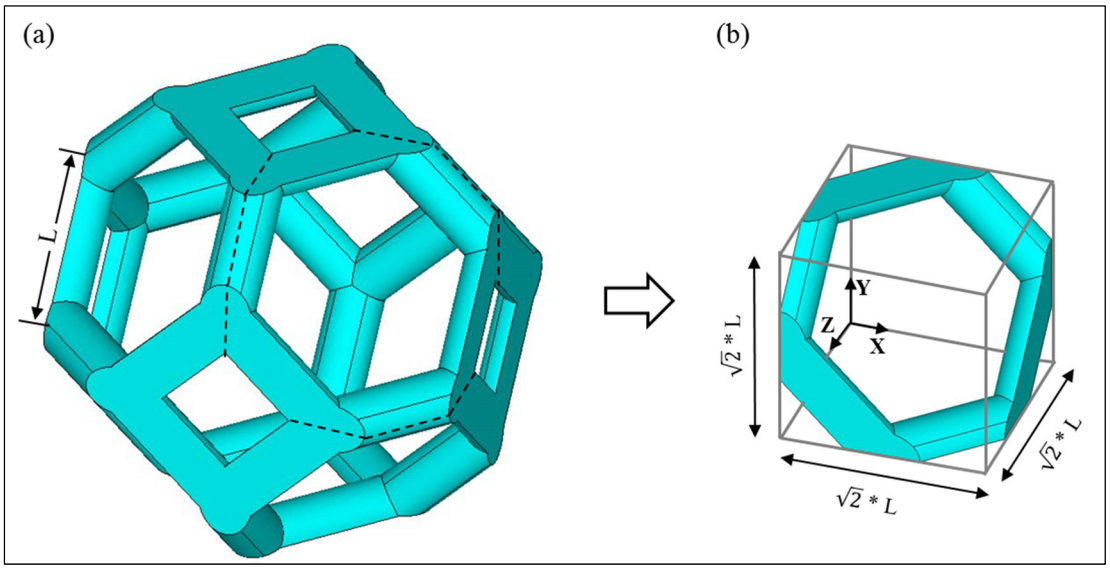

Figure 2.3 TKDH unit cell CAD geometry with 90% porosity: (a) Whole unit cell (b) one-eighth of the cell used for FEA

BCC unit cell has a simple geometry and is made of four struts with a length of L that cross at a node in the center of the cube. Due to symmetry in all directions, it is possible to model and analyze just one-eighth of the unit cell including half of a strut with a length of L/2. Figure 2.4 shows the BCC unit cell along with the dimensions of the cube.

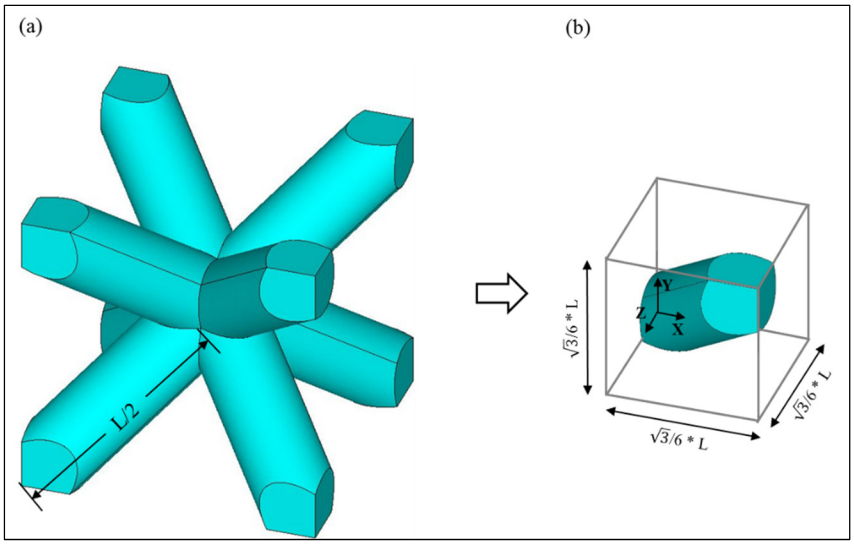

Figure 2.4 BCC unit cell CAD geometry with 70% porosity:
(a) Whole unit cell (b) one-eighth of the cell used for FEA

F2BCC unit cell is a combination of BCC unit cell with two face centered cubic (FCC) unit cells. Therefore, this unit cell has 12 struts in total, eight of which are located on four vertical faces of the cube (parallel to x and y planes). The other four struts intersect at the center of cube. See Figure 2.5 for geometrical details of this unit cell.

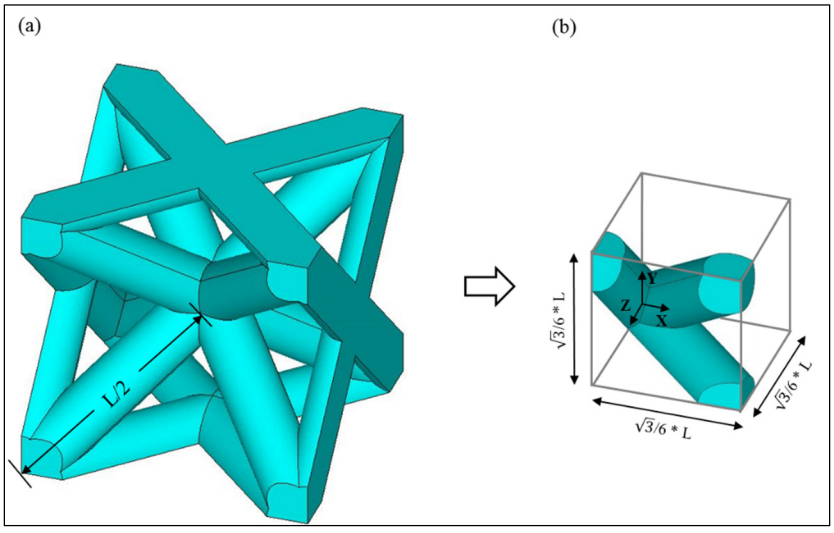

Figure 2.5 F2BCC unit cell CAD geometry with 70% porosity:
(a) Whole unit cell (b) one-eighth of the cell used for FEA

2.1.2 Material Model

The material model built in the Ansys FE software was used for the FE simulations. This model is based on Auricchio's model (Auricchio 2001), where the material parameters are determined based on uniaxial superelastic response of the SMA. These parameters are martensite start stress, σ_{ms}, martensite finish stress, σ_{mf}, austenite start stress, σ_{as}, austenite finish stress, σ_{af}, and maximum transformation strain, ε_L. Figure 2.6 shows these parameters in a schematic stress-strain curve of a superelastic material response. There is also another parameter, α, which accounts for the tension-compression asymmetry. This parameter was set to zero, assuming the symmetrical behavior. Other than SMA-related parameters, the elastic behavior of the material should also be defined by the Young's modulus E, and Poisson's ratio ν.

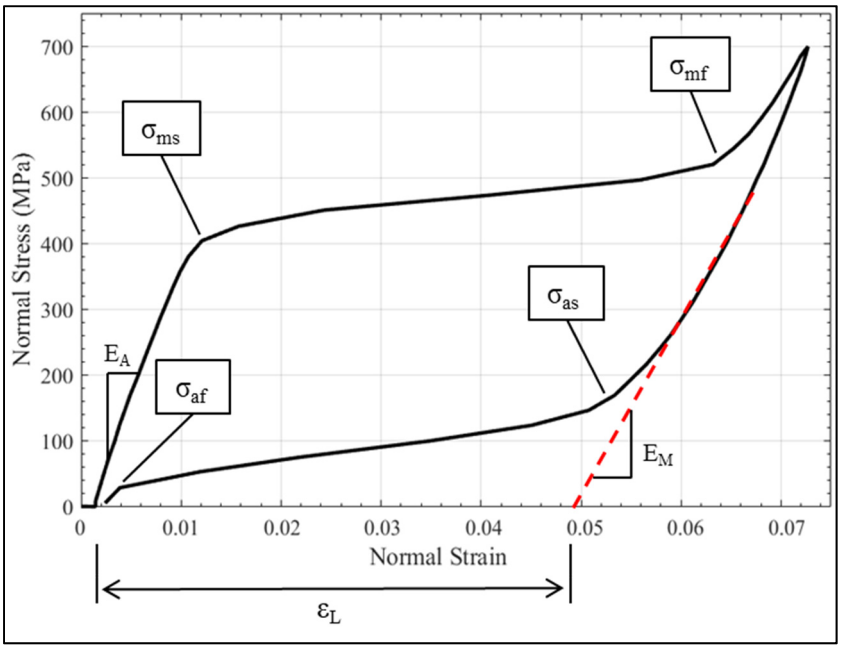

Figure 2.6 Material parameters in Ansys material model defined from the uniaxial test results of NiTi samples, taken from (Khodaei and Terriault 2018)

The material parameters used for the analyses of unit cells were based on the uniaxial tensile test results of NiTi samples from (Khodaei and Terriault 2018), which are listed in Table 2.1. Here, the austenite elastic modulus E_A was assigned.

Table 2.1 Material parameters used for the material model in Ansys based on Auricchio's model

Young's modulus, E_A [MPa]	49400
Poisson's ratio, ν	0.33
Martensite start stress, σ_{ms} [MPa]	403
Martensite finish stress, σ_{mf} [MPa]	544
Austenite start stress, σ_{as} [MPa]	169
Austenite finish stress, σ_{af} [MPa]	28
Transformation strain, ε_L [%]	4.8
Tension-compression asymmetry parameter, α	0

2.1.3 Boundary Conditions and Loadings

The type of boundary conditions suitable for a unit cell depends on the boundary conditions imposed on the structure. Here, the boundary conditions applied on all unit cells are based on the assumption that the porous structure has free boundary condition. This means that the outer surfaces of the structure except the areas of loading and fixtures are free to deform. This assumption, together with the fact that symmetry condition applies on all lateral directions of the unit cells (X and Y planes where no loads are applied), makes it suitable to apply planar conditions on faces of the boxes enclosing the unit cells (Terriault and Brailovski 2017). Planar condition requires that all nodes on a certain plane remain in that plane during the analysis, while the nodes will be free to move in their plane, and the plane itself can move as well. To fulfill this requirement, it is necessary that the nodes have identical displacements normal to the plane. In Ansys the planar condition is imposed through coupling of the degrees of freedom (DOFs).

Symmetry condition also requires that the shear stress to be zero on the symmetry plane. Since the nodes on all boundary surfaces are free to move in their plane, no shear stress will develop. Figure 2.7(a) shows how different surfaces of the box encompassing the unit cell are named according to the coordinate system attached to it.

The following boundary conditions were applied:

1. The nodes on the back, left and bottom surfaces were fixed in DOF perpendicular to their respective surfaces according to (2.1).

$$\mathrm{UX}|_{\mathrm{x}=0} = 0\,, \quad \mathrm{UY}|_{\mathrm{y}=0} = 0\,, \quad \mathrm{UZ}|_{\mathrm{z}=0} = 0 \tag{2.1}$$

   where UX, UY and UZ are the displacement components of the nodes in X, Y and Z directions, respectively. These three conditions satisfy the planar condition, and also prevent the rigid body motion of the unit cell in all the translational and rotational DOFs.

2. For the nodes on the top, front and right surfaces, coupling equations were defined for DOFs perpendicular to the nodes' respective planes, so that all nodes have identical normal displacements, see (2.2).

$$\mathrm{UX}_{\mathrm{i}} = UX_F\,, \quad \mathrm{UY}_{\mathrm{j}} = UY_R\,, \quad \mathrm{UZ}_k = UZ_T \tag{2.2}$$

where i, j, k are the number of all the nodes that reside on front, right and top surfaces, respectively, and $\mathrm{UX_F}$, $\mathrm{UY_R}$ and $\mathrm{UZ_T}$ are the values of the displacements normal to front, right and top planes, respectively. Figure 2.7(b) illustrates the applied boundary conditions.

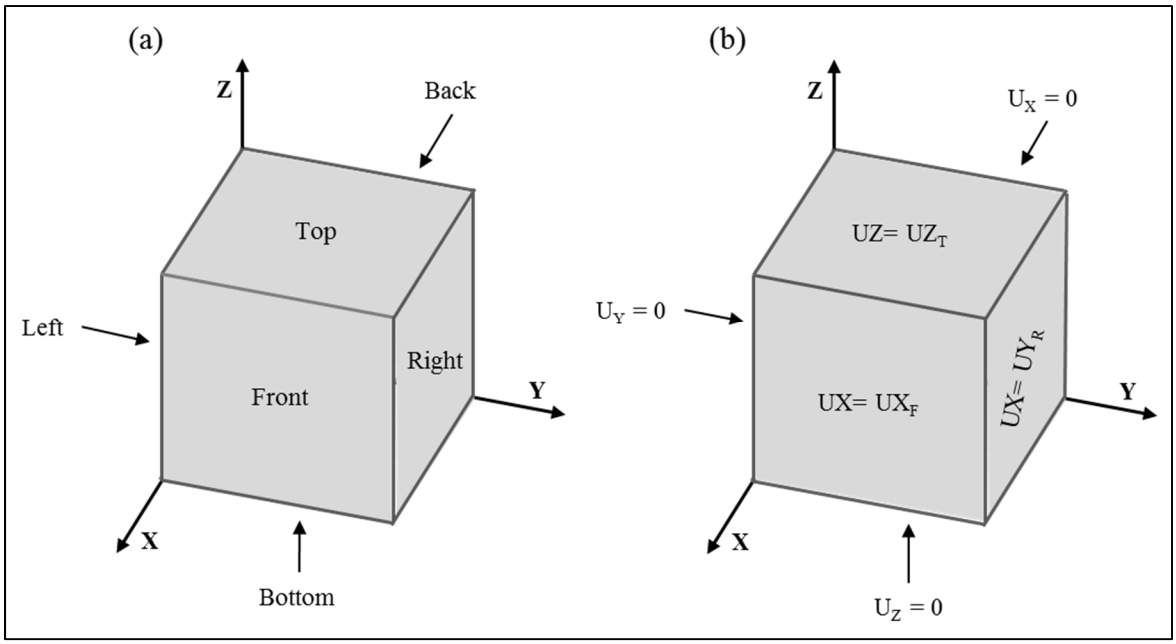

Figure 2.7 Boundary conditions applied to the unit cells: (a) Naming of surfaces of the box enclosing the unit cell (b) The constraints and couplings applied to each surface

The loading in all analyses were applied on "top" surface in form of force for mesh convergence study, or prescribed displacement for the main analyses (see Figure 2.8).

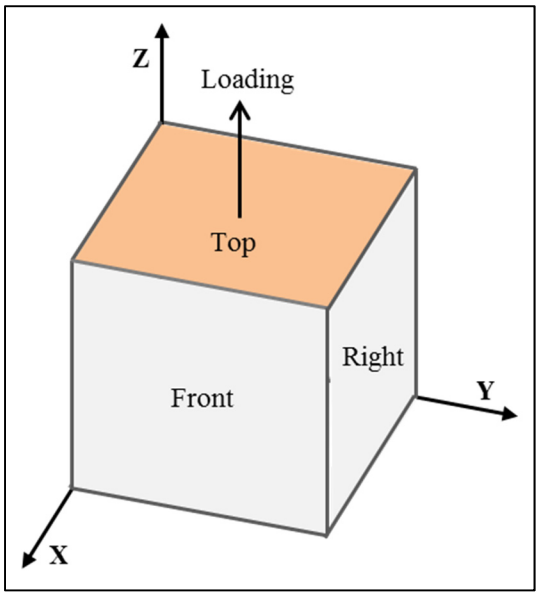

Figure 2.8 Applied loading on top surface of the unit cell

2.1.4 Mesh Convergence Study

The geometry of each unit cell was meshed using 3D, 10-node quadratic tetrahedral solid elements (Ansys element type: solid187). In order to find an optimal element size, a mesh convergence study was conducted for all unit cells. The geometry of a 70% porosity unit cell was used for mesh convergence in all unit cell types (a separate analysis with 30% porosity was also performed for comparison reasons). In order to maintain a more consistent measure of element size and mesh quality with respect to varying porosity, the e/D ratio was used as a metric of convergence, where e is the element size and D is the strut diameter. The exception was the spherical unit cell where the element size e was directly used and a porosity of 10% was analyzed.

We started the process from an initial coarse mesh with an e/D ratio of 1 for the strut-based and 0.4 mm for the spherical unit cell. A tensile force was applied to the top surface of the unit cell. After running the simulation, the maximum total nodal displacement in the model (USUM in Ansys) was extracted. Then in each subsequent iteration, the element size was reduced by half. With the new finer mesh, the same analysis was repeated, and the maximum total displacement was compared with the previous result. This process was continued until the amount of change in the results between the two last analyses would not exceed 2%. At this point, the mesh refinement would be deemed sufficient. Figure 2.9 shows the diamond unit cell with e/D ratios ranging from 0.5 to 0.0625.

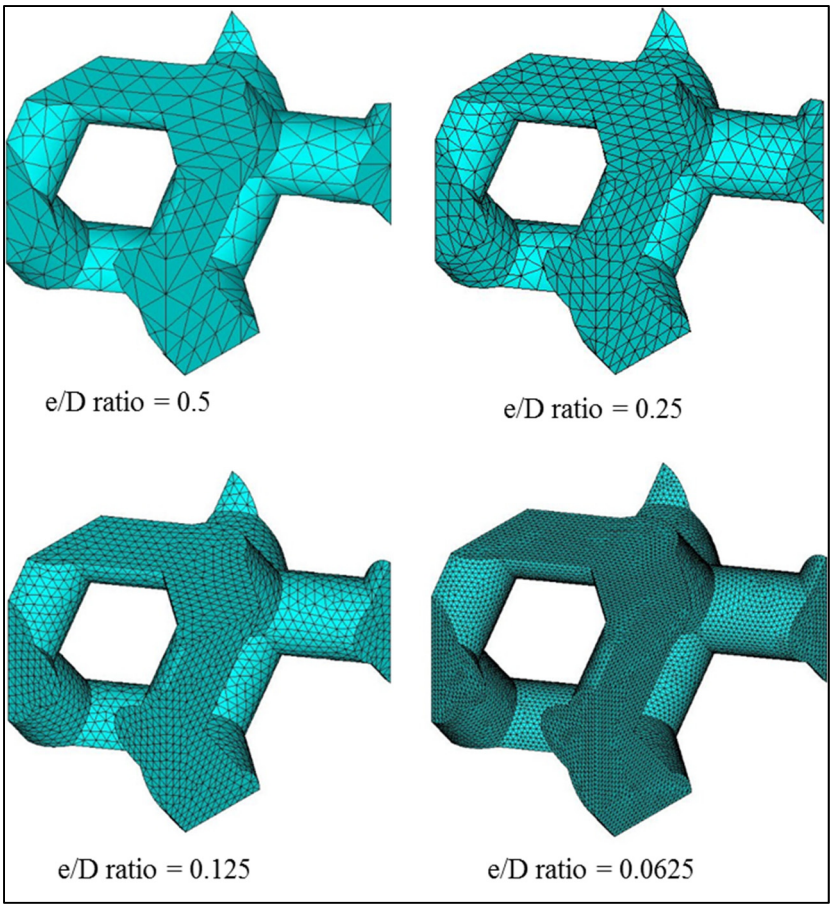

Figure 2.9 Meshing of diamond unit cell with 70% porosity and different e/D ratios

As mentioned above, all mesh convergence analyses were conducted on unit cells with 70% porosity. To control for a possible variation in the results, one set of extra analyses were also performed on F2BCC unit cells with 30% porosity. Figure 2.10 shows the F2BCC unit cell with 30% porosity and e/D ratios from 0.5 to 0.0625.

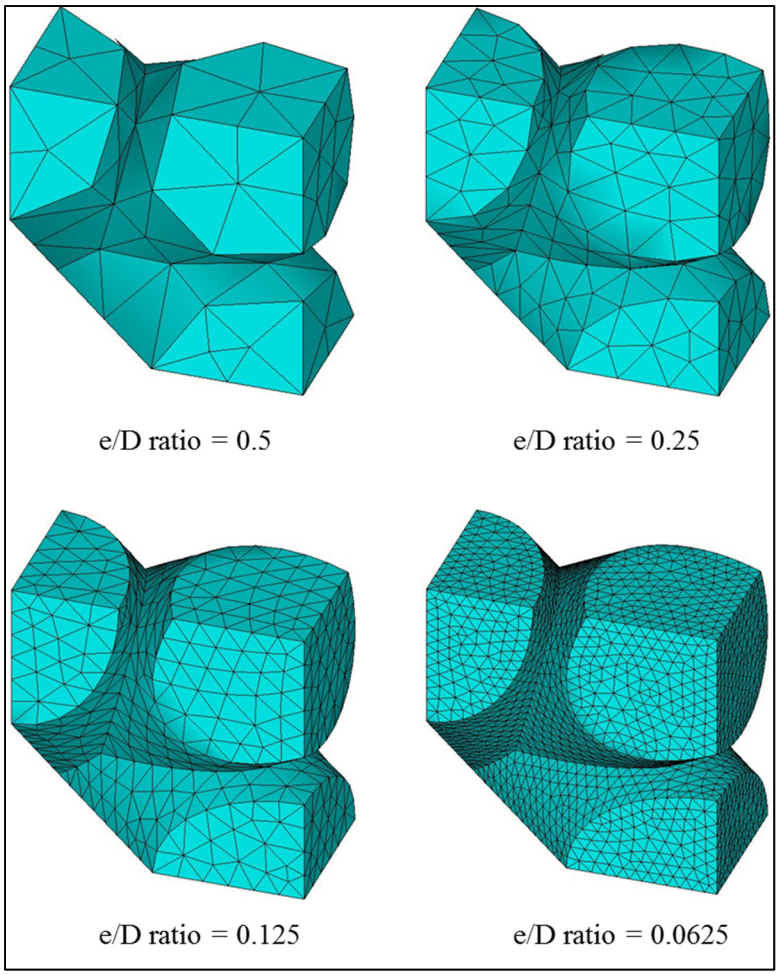

Figure 2.10 Meshing of F2BCC unit cell with 30% porosity and different e/D ratios

2.1.5 Analysis setup

Having determined the optimal element size for the mesh, two series of analyses where conducted on each unit cell type, and for each porosity level: analysis for determining the maximum admissible reversible strain, and load-unload cycle up to the determined maximum strain.

It should be noted that in all analyses, large displacement, non-linear solution type was selected in Ansys to account for geometric non-linearity.

2.1.5.1 Determining the maximum admissible reversible strain

The aim of these analyses was to determine the extent to which the unit cell can undergo reversible deformation until it reaches a limit, after which the unit cell would sustain plastic deformation. Existence of stress risers such as sharp corners in the unit cell's geometry means that the peak local stress at these locations will reach the plastic limit much earlier than the rest of the model. Theoretically, if the stress in only one node exceeds the yield stress, the unit cell has entered the irreversible zone. However, having this criterion as the limit makes the results highly mesh-dependent and unreliable. Alternatively, we introduced a 0.5% volume fraction criterion, rather than a single node to consider as the threshold. Therefore, slightly more deformation is tolerated until 0.5% of the material reaches the stress limit. By using this criterion, more realistic and consistent results can be achieved for different geometries. Note that this limit value was chosen under the circumstances of this study, therefore, other values are possible based on the given conditions and desired accuracy.

The stress limit was taken from the experimental tests of NiTi tubes (Khodaei and Terriault 2018) and was set to 1100 MPa which is an approximate point in the stress-strain curve where the material loses linearity in a tensile test (see Figure 2.11). The evaluation of 0.5% volume fraction limit was approximated using the number of nodes with over-limit stress divided by the total number of nodes in the FE model.

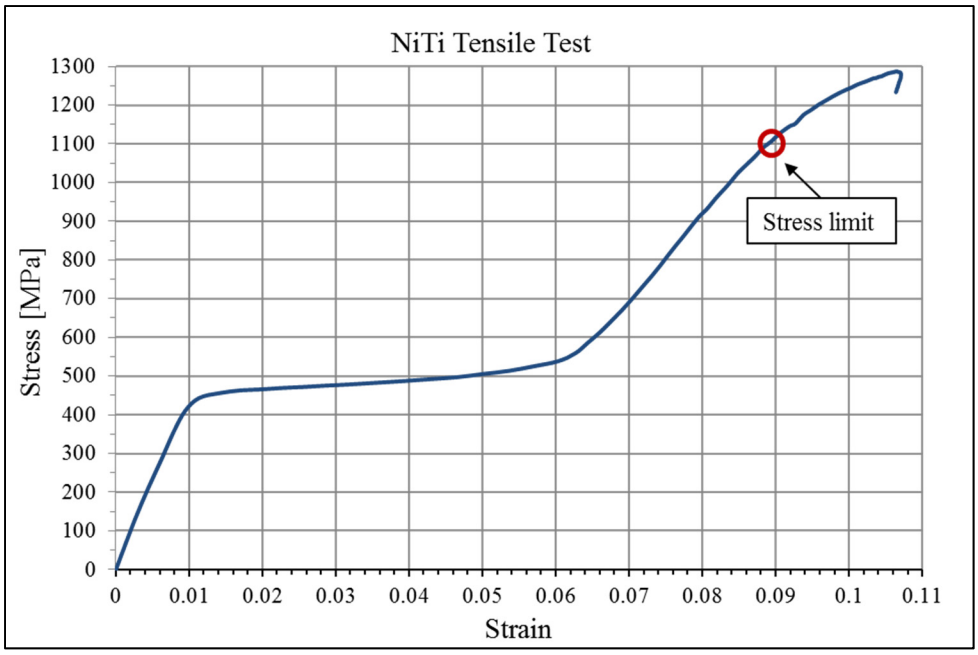

Figure 2.11 Stress- strain response of NiTi alloy under uniaxial tensile test

The analysis was conducted iteratively with an initial tensile displacement of $\Delta = 0$, and successively increasing it until the criterion is met. The following operations were executed in Ansys using APDL:

1. Modifying the total displacement as $\Delta = \Delta + \delta$ and applying it on "top" surface of the unit cell in Z direction, where δ is a small increment of the displacement
2. Solving the FE Analysis
3. Extracting all the nodal Von Mises stresses
4. If the number of nodes with stresses over the limit makes up more than 0.5% of the total nodes, then exit the loop and register the applied displacement Δ as the amount of displacement the unit cell can undergo reversibly.
5. Else, go to step 1.

2.1.5.2 Loading and uploading cycle based on the maximum strain

Once the amount of reversible strain is determined for each of the unit cells, and in all porosities, another set of analyses was performed, in which the unit cells were loaded up to the

displacement corresponding to their maximum apparent strain and unloading down to zero. This group of analyses leads to the unit cell response in form of the full hysteresis cycle, as well as the data that are used for calculating a number of quantities which are described below.

2.1.6 Post-processing

The quantities extracted or calculated from the FE solution results are:

- Apparent reversible strain,
- Apparent austenite elastic modulus (E_A),
- Energy absorption/ dissipation,
- Volume fraction of austenite, martensite and mixed phases during the loading.

The apparent reversible strain of the unit cell can be calculated once the maximum admissible displacement Δ_{max} is determined (see 2.1.5.1). The apparent strain ε will be:

$$\varepsilon = \Delta_{max}/\mathrm{h} \tag{2.3}$$

where h is the height of the unit cell in Z direction.

In order to calculate the apparent elastic modulus, as well as plotting the stress-strain response of unit cells, first the apparent stress of the unit cell needs to be determined. Since the analyses are displacement-controlled, the reaction force, F_R generated on the bottom surface of the unit cell can be extracted. The total reaction force in each time step was obtained by summing up the nodal forces on the bottom surface. Dividing the total reaction force by the bottom surface area of the unit cell box ($A = d \times w$), the apparent stress σ is calculated as:

$$\sigma = F_R/A \tag{2.4}$$

Since in the beginning of loading, the material is entirely in austenite phase, the initial slope of the apparent stress-strain curve represents the austenite elastic modulus:

$$E_A = \sigma_0/\varepsilon_0 \tag{2.5}$$

where subscript 0 indicates the values of apparent stress and strain in the beginning of loading.

By obtaining the apparent stress-strain response of the unit cell, the strain energy can be obtained by calculation of the area under the apparent stress-strain curves. The area under the loading curve gives the amount of the strain energy that is absorbed by the unit cell during the loading. When the unit cell is unloaded to zero, a part of the input loading energy is recovered which corresponds to the area under the unloading curve. This leaves the area inside the hysteresis cycle which represents the dissipated energy in form of heat. Figure 2.12 shows these energy definitions schematically.

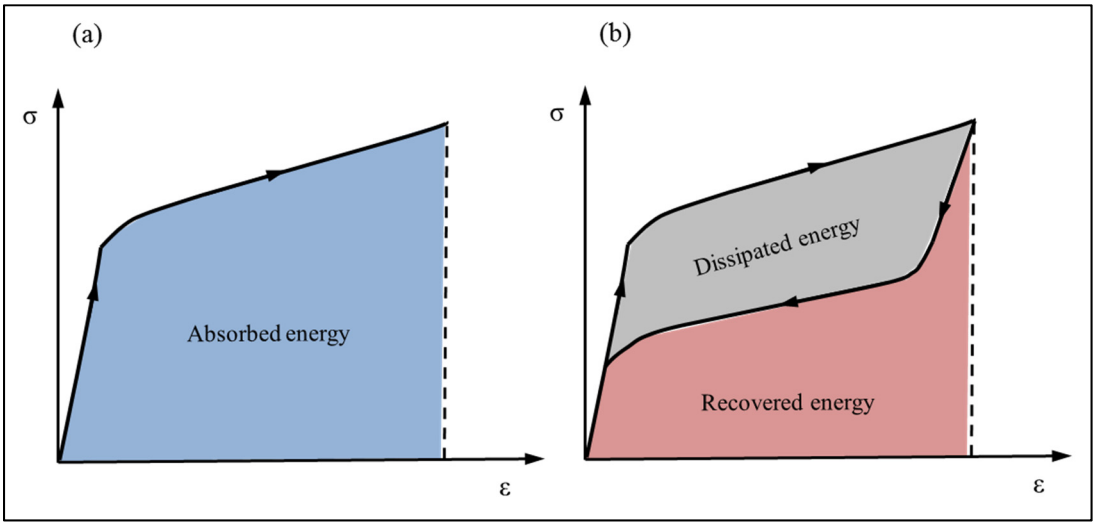

Figure 2.12 Schematic illustration of strain energy absorption (a) and dissipation (b) during the loading and unloading

The volume fractions of austenite, martensite and mixed phases during the loading process were calculated using the nodal Von Mises stresses, and the percentage of nodes in each phase

was used as an approximation of the volume fraction. This approximation can only be made when a uniform mesh is created across the whole geometry, which is the case in this work. To determine these fractions, at each time step, the nodes were sorted based on their Von Mises stresses and grouped based on the σ_{ms} and σ_{mf} values provided in Table 2.1. The nodes having stresses below σ_{ms} fall into austenite group, between σ_{ms} and σ_{mf} into mixed or "in transformation" group, and over the σ_{mf} stress, into the martensite group.

2.2 Results and Discussions

2.2.1 Mesh Convergence

The mesh convergence analysis results for all unit cells are summarized in Table 2.2. The mesh refinement is considered converged when the maximum total nodal displacement (USUM) changes less than 2% with further element size decrease. Spherical unit cell converged at an element size of 0.1 mm, however the mesh with this size resulted in poor element quality at around 50% porosity due to a very thin wall. Therefore, a finer mesh with element size of 0.05 was chosen. As for strut-based unit cells, the mesh convergence analyses resulted in the same e/D ratios of 0.125 for all types, except for TKDH unit cell where e/D ratio of 0.25 deemed acceptable. However, in order to have consistent mesh density across all unit cells as well as having large enough number of nodes for later volume fraction calculations, the same mesh density as other unit cells (e/D = 0.125) was used for TKDH as well.

Table 2.2 Mesh convergence analyses results for different unit cells: the shaded cells indicate converged values for element size or e/D ratios

Spherical - 70% porosity					
Element size (mm)	0.4	0.2	0.1	0.05	
Max. USUM (mm)	0.032148	0.034695	0.035082	0.035101	
Change	_	7.92%	1.11%	0.054%	
Diamond - 70% porosity					
e/D ratio	1	0.5	0.25	0.125	0.0625
Element size	1.245	0.6225	0.31125	0.155625	0.0778125
Max. USUM (mm)	0.024238	0.025671	0.026214	0.026774	0.026929
Change	_	5.91%	2.11%	2.13%	0.0578%
TKDH - 70% porosity					
e/D ratio	1	0.5	0.25	0.125	0.0625
Element size	1.417	0.7085	0.35425	0.177125	0.0885625
Max. USUM (mm)	0.009575	0.009872	0.010222	0.010403	0.010501
Change	_	3.1%	3.54%	1.77%	0.94%
BCC - 70% porosity					
e/D ratio	1	0.5	0.25	0.125	0.0625
Element size	0.311	0.1555	0.0775	0.038875	0.019437
Max. USUM (mm)	0.011563	0.010462	0.010885	0.011285	0.011505
Change	-	9.52%	4.04%	3.67%	1.9%
F2BCC - 70% porosity					
e/D ratio	1	0.5	0.25	0.125	0.0625
Element size	0.234	0.117	0.0585	0.02925	0.014625
Max. USUM (mm)	0.00733	0.007595	0.007707	0.007959	0.008084
Change	_	3.61%	1.47%	3.27%	1.57%
F2BCC - 30% porosity					
e/D ratio	1	0.5	0.25	0.125	0.0625
Element size	0.4235	0.21175	0.105875	0.052938	0.026469
Max. USUM (mm)	0.002016	0.001853	0.001942	0.001982	0.002018
Change	-	-8.08%	4.8%	2.05%	1.82%

2.2.2 Porosity Dependence of Reversible Strain

As a result of the first set of analyses described in 2.1.5.1, the amount of the reversible apparent strain for each of the unit cells and porosities from 10% to 90% was determined. The apparent

strain values determined for each of the geometries correspond to the applied displacement that causes 0.5% of the material in the unit cell to enter the plastic zone. Figure 2.13 shows Von Mises stress results of the spherical unit cell with porosities of 30, 50 and 70%, and Figure 2.14 shows the Von Mises stress results for strut-based unit cells with 70% porosity, all of which are plotted at their maximum strain limit. The gray areas in these figures indicate stresses above the limit of 1100 MPa, which was set as the plastic limit.

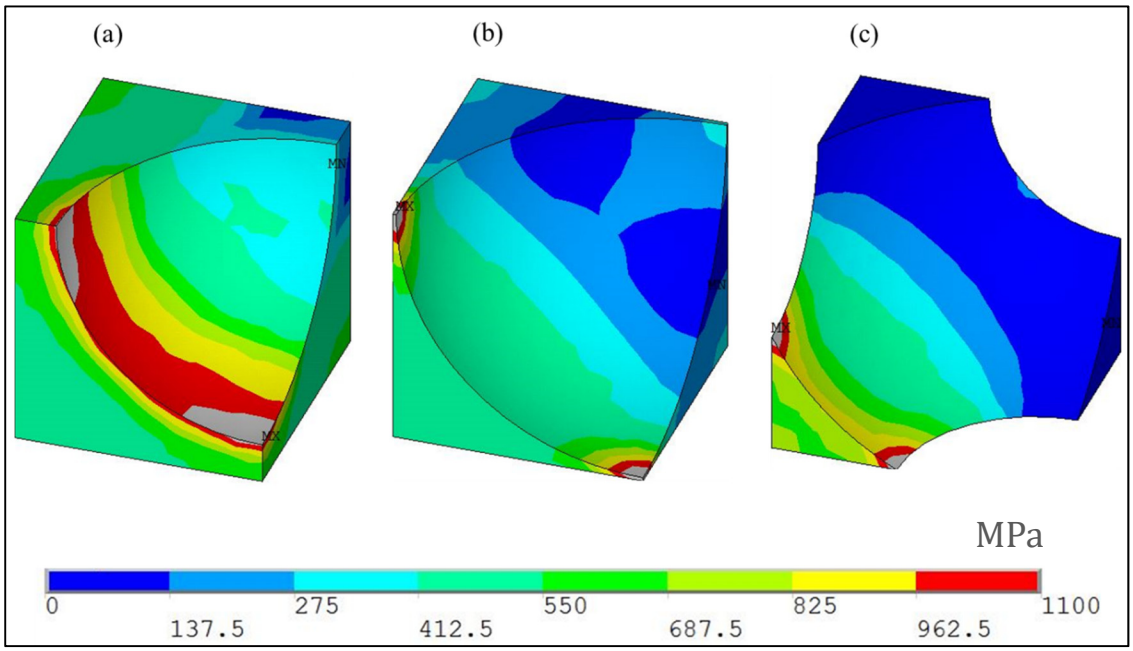

Figure 2.13 Von Mises stress results of spherical unit cells with 0.5% of the material over the stress limit of 1100MPa, indicated with gray areas. (a) 30% (b) 50% (c) 70% porosity

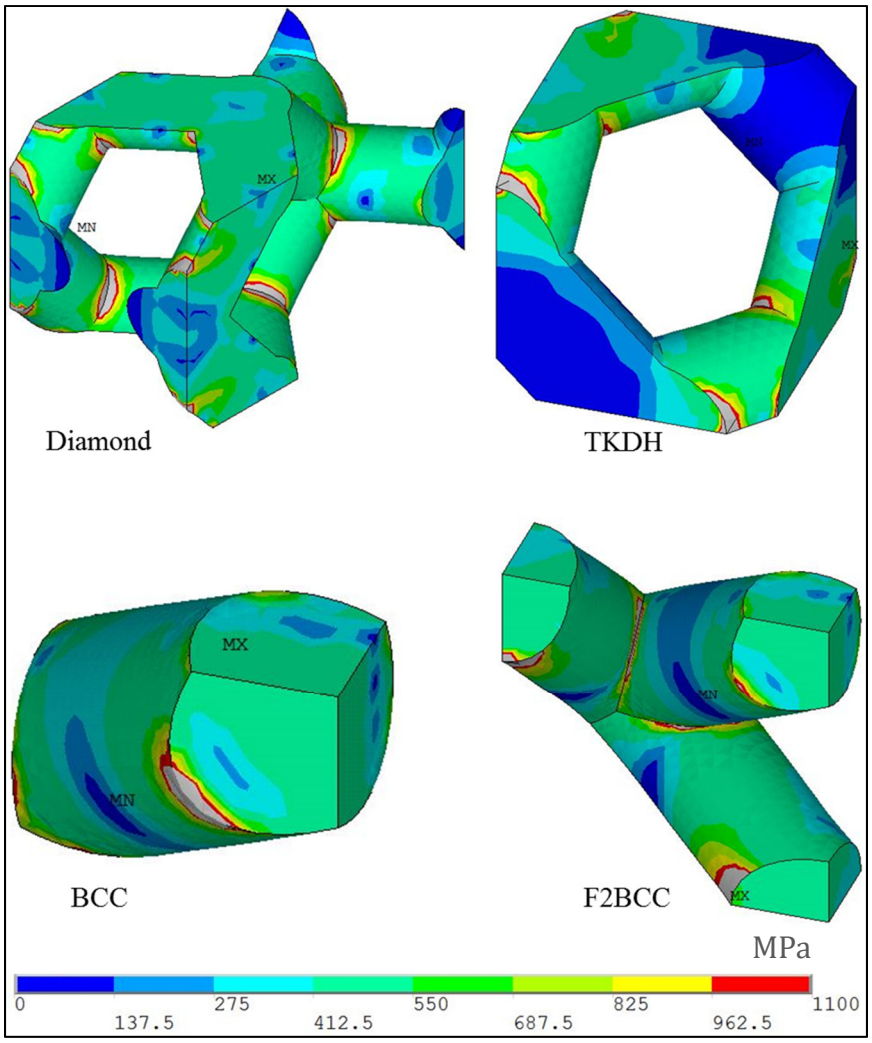

Figure 2.14 Von Mises stress results of strut-based unit cells with 0.5% of the material over the stress limit of 1100 MPa, indicated with gray areas; all unit cells have 70% porosity

Figure 2.15 shows the variation of the apparent strain for all unit cells with porosities of 0% (dense material) up to 90%. As can be seen from the results, the behavior of spherical unit cell is particularly different from other strut-based unit cells. The strain for this unit cell significantly drops at 50% porosity, which is due to the fact that the geometry has very thin walls that significantly raise the stress concentration (see Figure 2.13 b). This in turn causes the unit cell to reach the plasticity limit much sooner. Also note that the topology of the unit cell transitions from closed cell to open cell for porosities beyond 50%. For porosities above

50%, the acceptable apparent strains remain low, which is due to the existence of sharp edges around the open pores (see Figure 2.13 c).

As for strut-based unit cells, the apparent strains of different unit cells for porosities of 50% and below are relatively similar. Since low-porosity unit cells have bigger strut diameters that overlap with other struts and take up most of the unit cell box volume, the significance of unit cell topology is small which can explain the small difference between unit cells. However, the difference in the apparent strain becomes more pronounced as the porosity increases and the unit cell topologies become more influential. For porosities between 50 and 70%, diamond unit cell exhibits the highest strain followed by BCC and F2BCC unit cells, but for 80 and 90% porosities, BCC and F2BCC unit cells show significantly higher strains. TKDH unit cell shows lower strain compared to these three unit cells and does not increase significantly with increasing porosity.

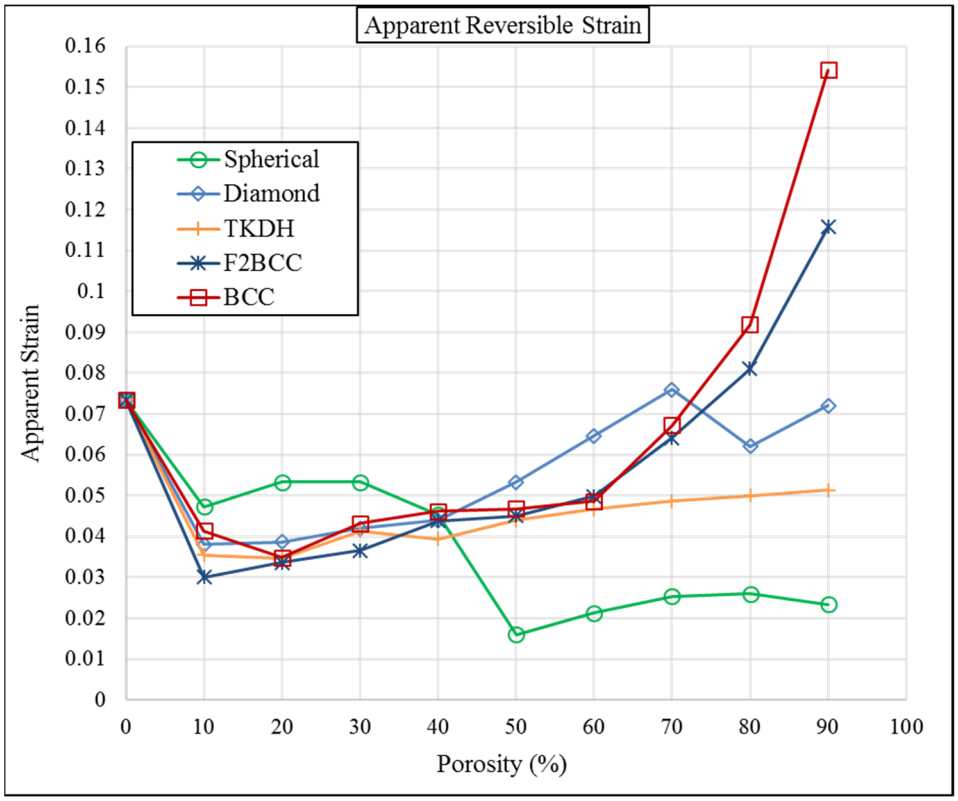

Figure 2.15 Apparent strain of unit cells with respect to the porosity

2.2.3 Apparent Stress-Strain Curves

Applying a load-unload cycle up to the max reversible apparent strain, the apparent stress-strain curves were generated. All unit cells with all porosities exhibit the superelastic behavior with a distinguishable hysteresis cycle. As an example, the results for TKDH cells are provided in Figure 2.16, where the apparent stress-strain curves are plotted separately for each porosity.

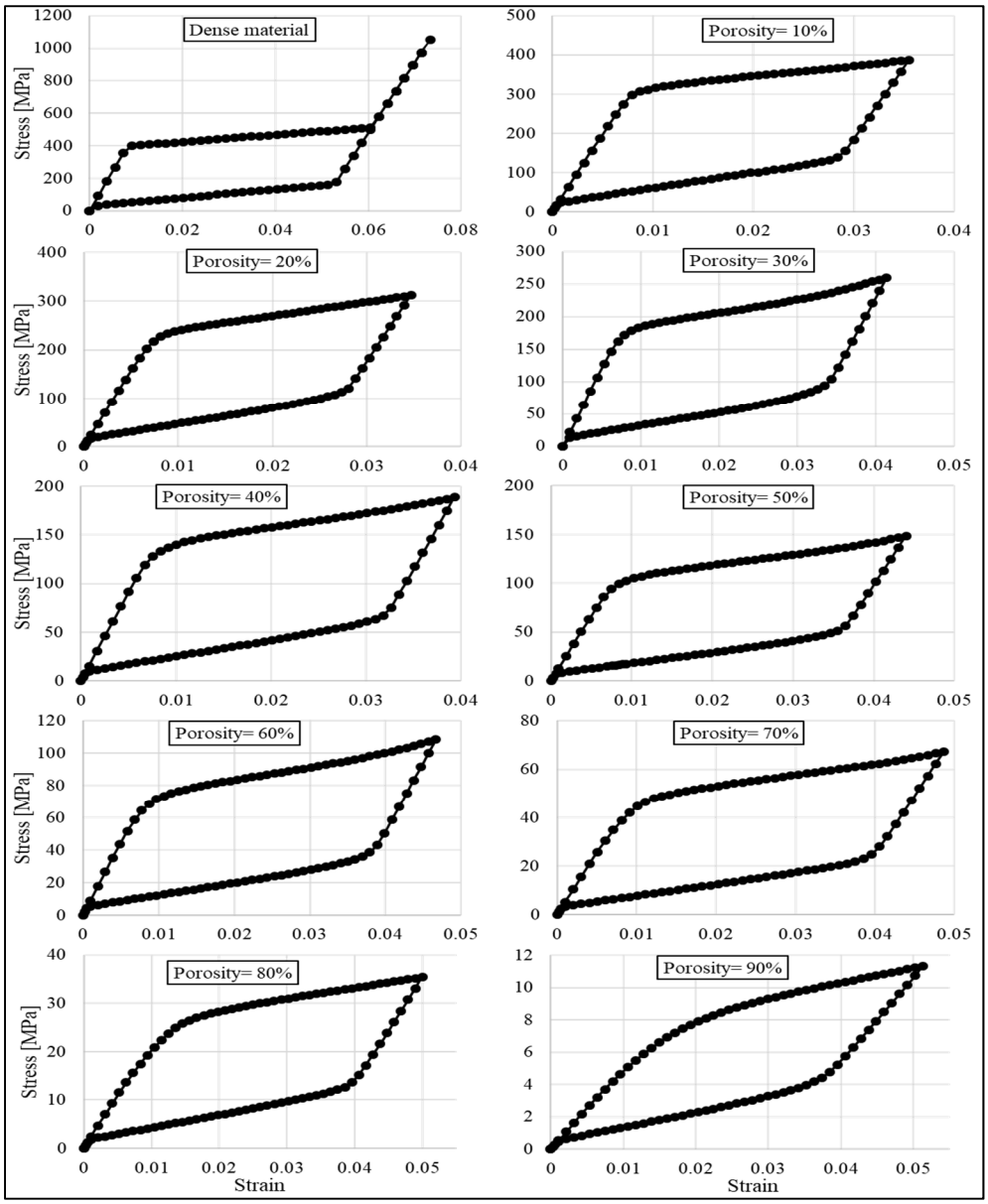

Figure 2.16 Apparent stress-strain curves of TKDH unit cell for all porosities

For a better comparison and brevity, the apparent stress-strain curves were combined in a unified graph. Figure 2.17 to Figure 2.21 show these results for all unit cells.

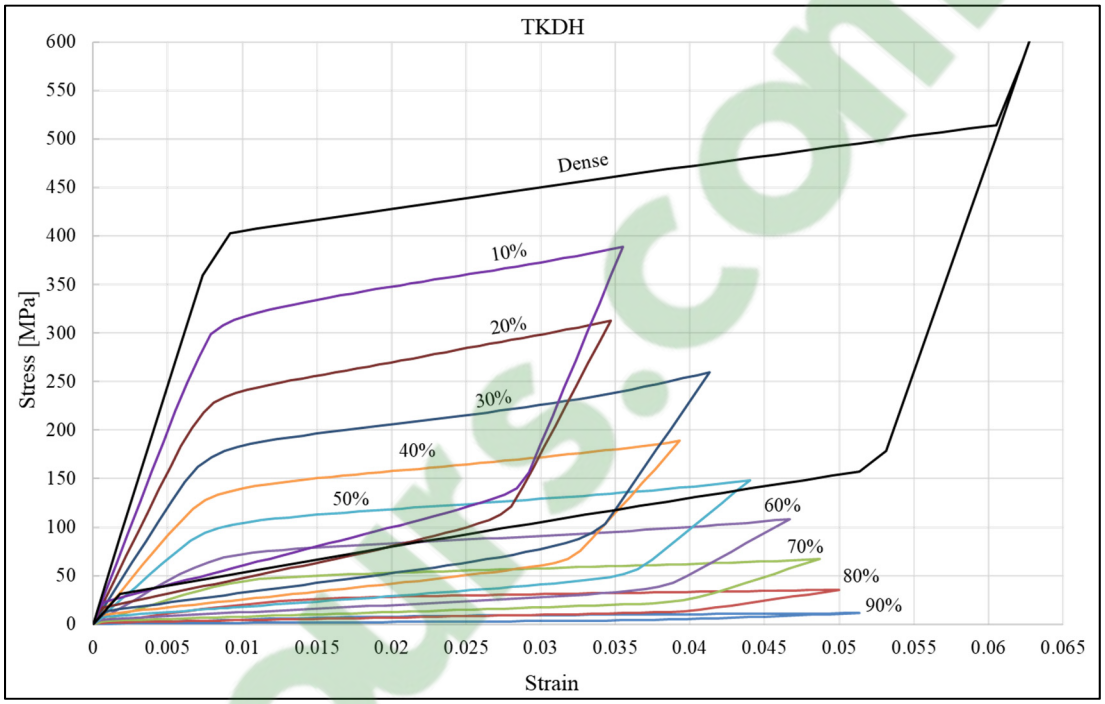

Figure 2.17 Comparison of the apparent stress-strain responses of the TKDH unit cell with different porosities

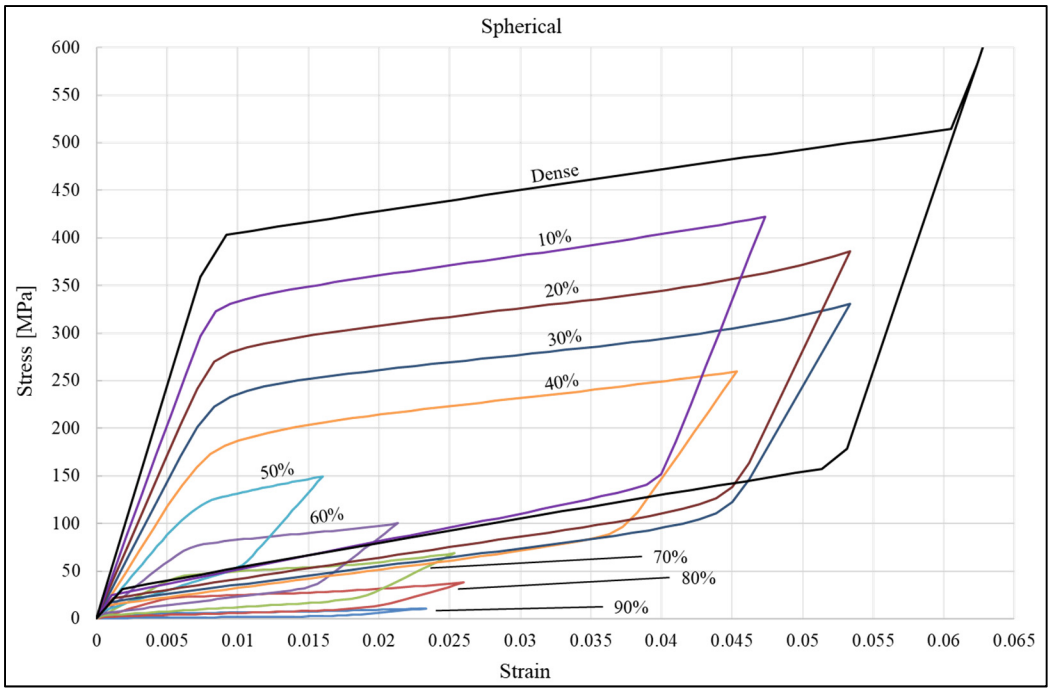

Figure 2.18 Comparison of the apparent stress-strain responses of the spherical unit cell with different porosities

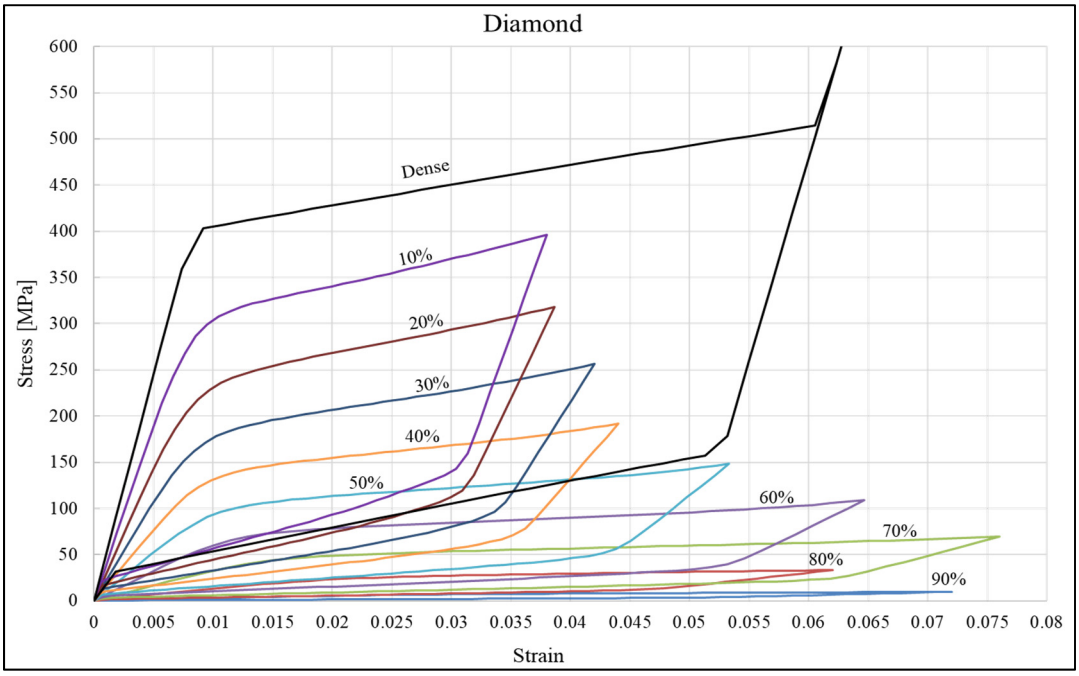

Figure 2.19 Comparison of the apparent stress-strain responses of the diamond unit cell with different porosities

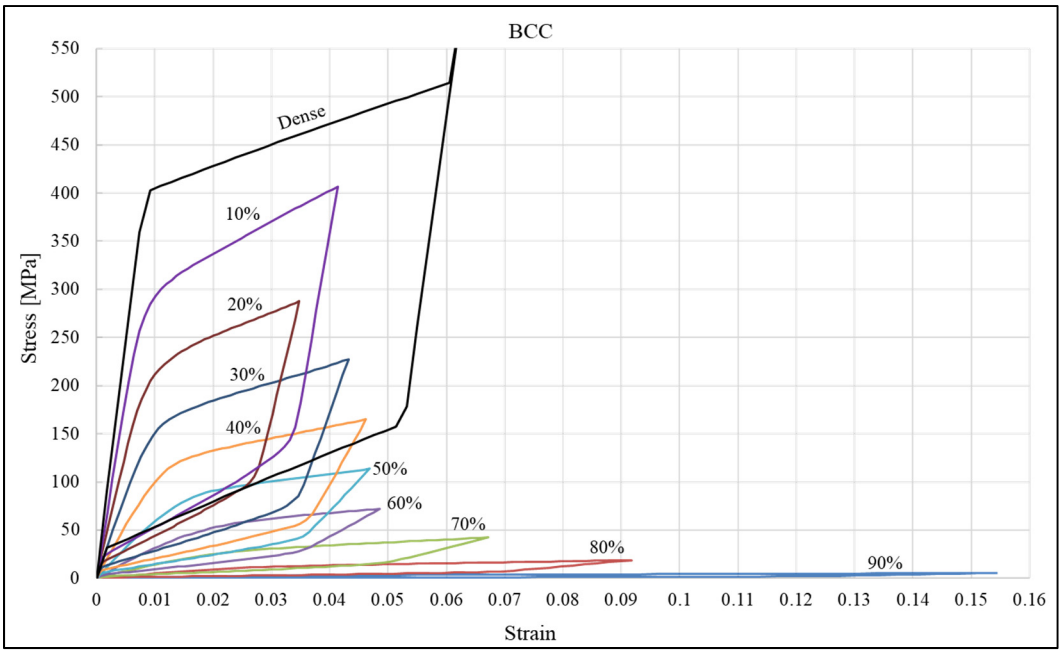

Figure 2.20 Comparison of the apparent stress-strain responses of the BCC unit cell with different porosities

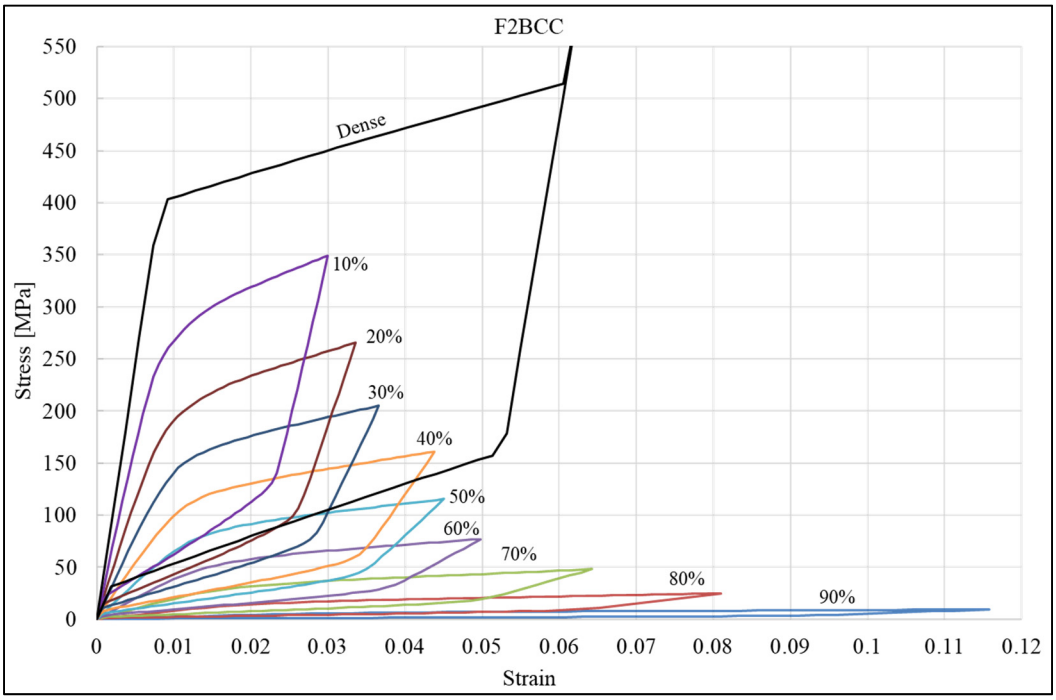

Figure 2.21 Comparison of the apparent stress-strain responses of the F2BCC unit cell with different porosities

2.2.4 Porosity Dependence of the Apparent Elastic Modulus

The elastic modulus is a common metric for estimating the strength of unit cells, and a good comparison basis for different unit cell geometries. Here, we measured the apparent elastic modulus at the beginning of the loading, i.e. E_A, based on the apparent stress and strain results. Figure 2.22 shows the porosity dependence of E_A for all unit cells.

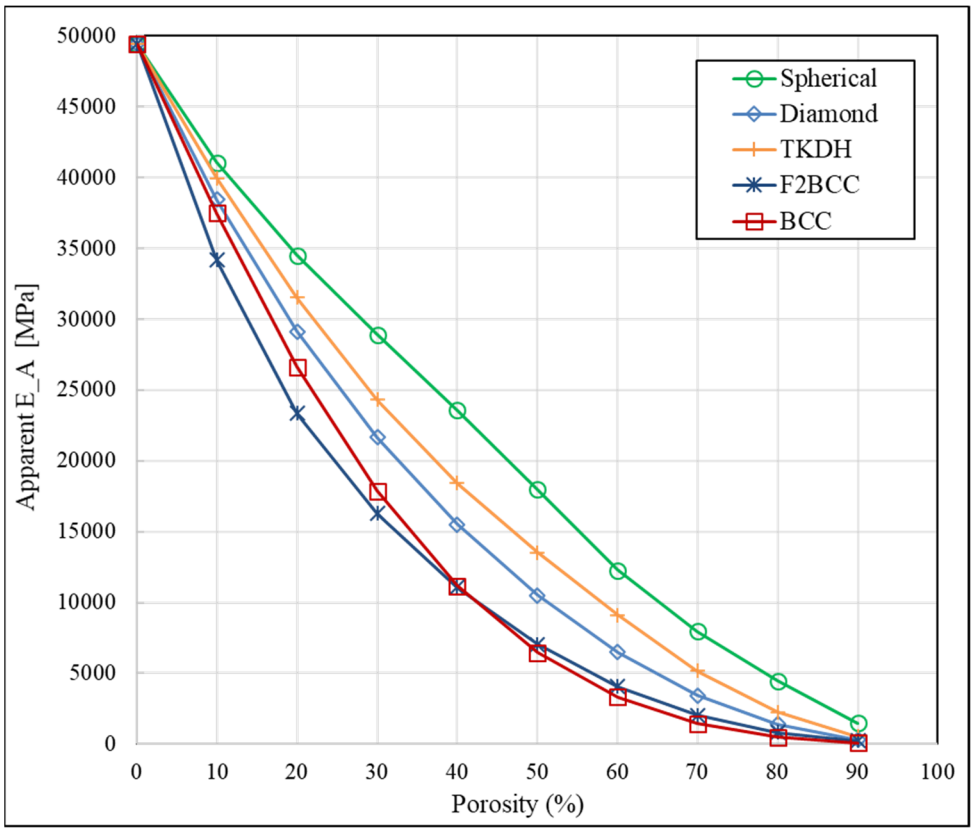

Figure 2.22 Apparent Young's modulus of austenite for all unit cells with respect to porosity

Spherical unit cell shows the highest strength for all porosities. But among the strut-based types, TKDH has the highest modulus followed by the diamond unit cell. BCC and F2BCC exhibit relatively similar stiffnesses.

Another observation worth mentioning is the amount of variation of the elastic modulus among different unit cells with respect to the porosity. As an example, at 10% porosity, the highest apparent elastic modulus belongs to the spherical with 41 GPa, and the lowest is 34.2 GPa for F2BCC, therefore, the ratio of the highest to lowest E_A will be 1.2 to 1. Now if we consider this at 90% porosity, the highest and lowest values are 1.46 and 0.087 GPa, for spherical and BCC, respectively, which results in a much greater ratio of 16.8 to 1. Table 2.3 lists the numerical values of E_A for all unit cells and porosities together with these ratios. One can also plot these ratios vs porosity as shown in Figure 2.23.

Table 2.3 Apparent elastic moduli, E_A of different unit cells in all porosities and the ratio of the highest value to the lowest at each porosity

Porosity (%)	Apparent Elastic Moduli of Austenite, E_A (GPa)					Max/min ratio
	Spherical	Diamond	TKDH	F2BCC	BCC	
0	49.4	49.4	49.4	49.4	49.4	1
10	41.0	38.4	39.9	34.2	37.5	1.20
20	34.5	29.1	31.5	23.3	26.6	1.48
30	28.9	21.6	24.3	16.3	17.8	1.78
40	23.6	15.5	18.4	11.1	11.1	2.13
50	17.9	10.5	13.5	7.03	6.44	2.79
60	12.2	6.48	9.11	4.05	3.31	3.70
70	7.96	3.42	5.17	2.03	1.45	5.47
80	4.47	1.40	2.25	0.83	0.49	9.05
90	1.46	0.30	0.51	0.23	0.087	16.8

One observation from the table above is that considering only the Young's modulus, choosing a certain unit cell over the other can save a significant amount of material. For example, among the strut-based unit cells, the diamond unit cell with 80% porosity has almost the same strength as a 70% BCC cell. This means 33% less material can be used. By including the spherical unit cell, even more material reduction can be achieved, as a 90% spherical unit cell exhibits a similar strength which means that the amount of material can be reduced by 67%.

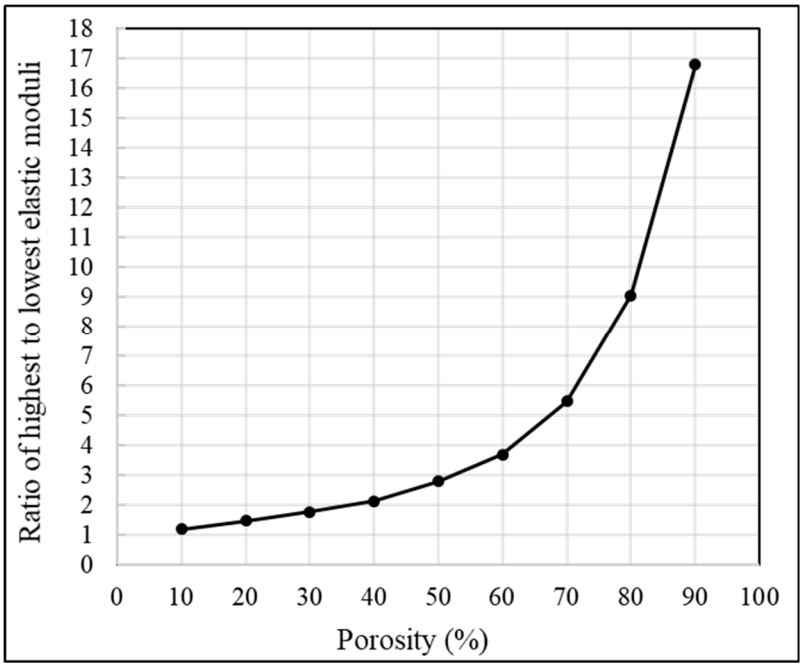

Figure 2.23 The ratios of highest to lowest apparent elastic moduli with respect to porosity

It can be seen from the figure that as the porosity increases, the variation between different unit cell types increases exponentially. This implies that the geometry of the unit cell becomes significantly more important in determining the strength of the unit cell at higher porosities. As discussed in 2.2.2, the same conclusion was also drawn regarding the reversible apparent strain results.

2.2.5 Volume Fraction of Material Phases During the Loading

The volume fractions of martensite and austenite phases, as well as the fraction of the material in transformation (mixed phase) where calculated at each time step, and their evolutions during the loading process are plotted for all porosities and unit cells.

For a dense SMA, the transition from austenite to mixed phase occurs in a very short strain interval, and over the whole geometry. As the strain increases, the material transitions rapidly once again from mixed phase to martensite. This rapid uniform transformation is due to the

lack of any geometric features to cause stress concentration. Therefore, the stress distribution and consequently the phase transformations are uniform across the material. This material phase transformation is depicted in Figure 2.24 in terms of volume percentage.

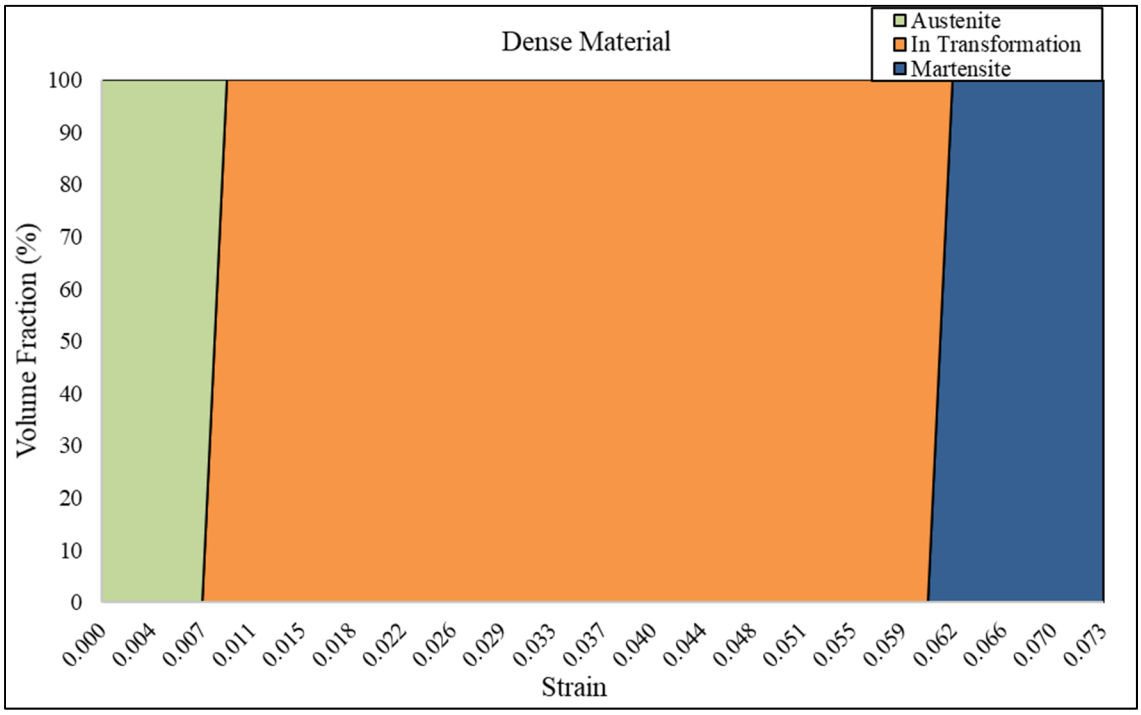

Figure 2.24 Volume fraction of material phases vs. apparent strain for dense material

However, in the case of porous SMA, existence of stress risers such as sharp corners, eliminates the stress uniformity in the model, hence the material enters phase transformation at these locations much earlier than the rest of the geometry. This leads to a gradual increase of the volume fraction of different phases with apparent strain. Figure 2.25 to Figure 2.28 show the transformation progress of these three phases for all unit cells and for porosities of 30, 50, 70 and 90%.

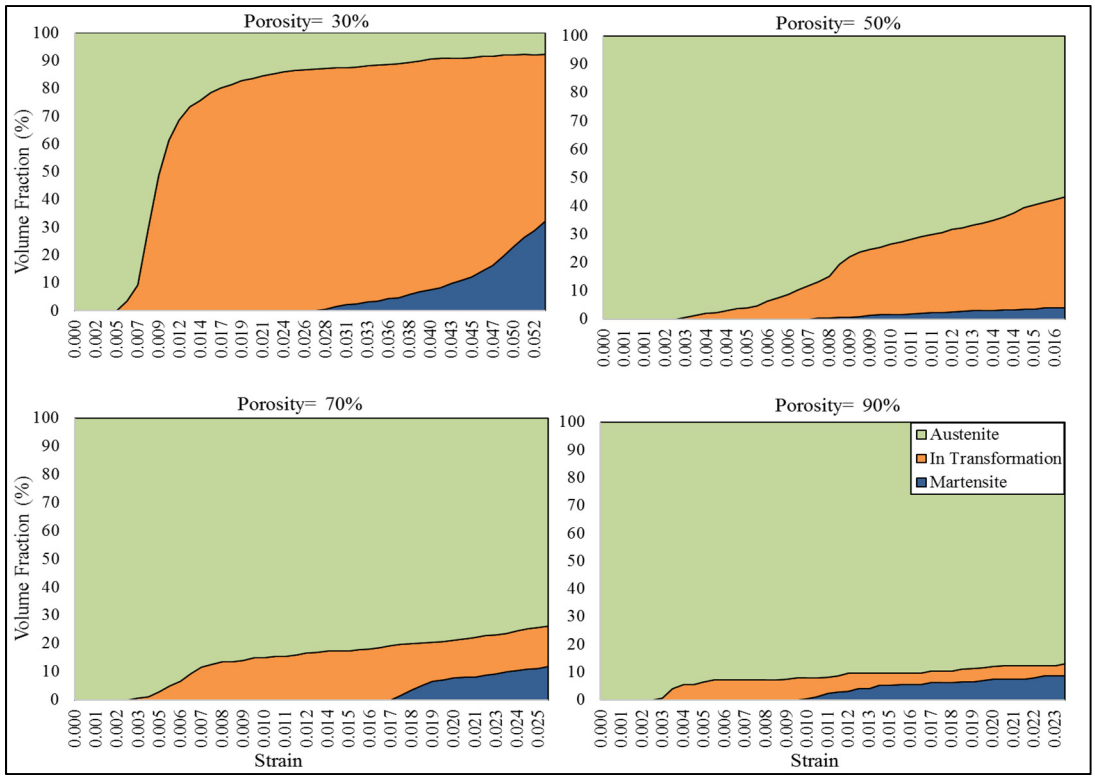

Figure 2.25 Volume fraction of material phases vs. apparent strain, spherical unit cell

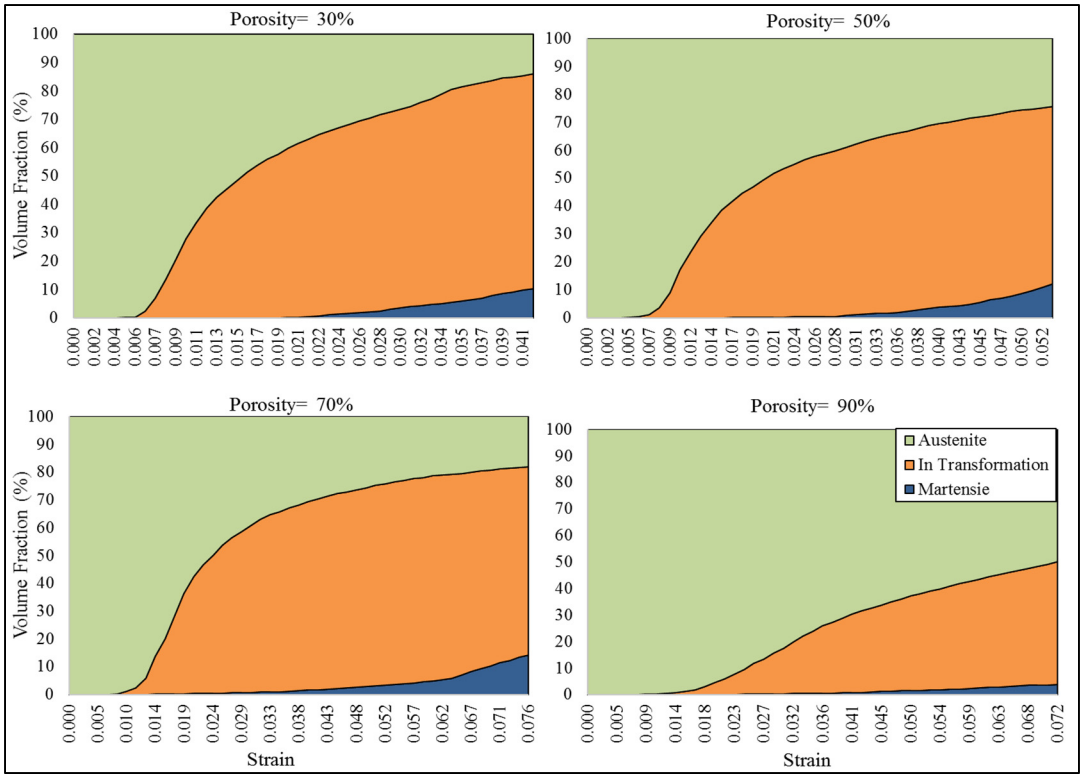

Figure 2.26 Volume fraction of material phases vs. apparent strain, diamond unit cell

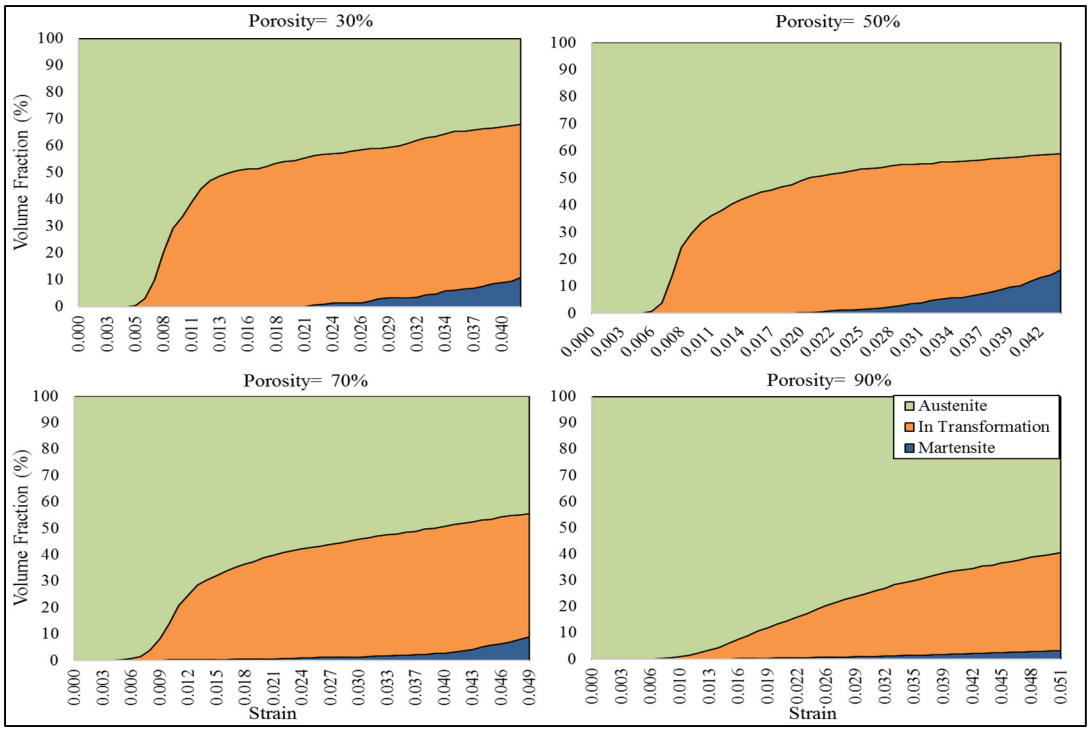

Figure 2.27 Volume fraction of material phases vs. apparent strain, TKDH unit cell

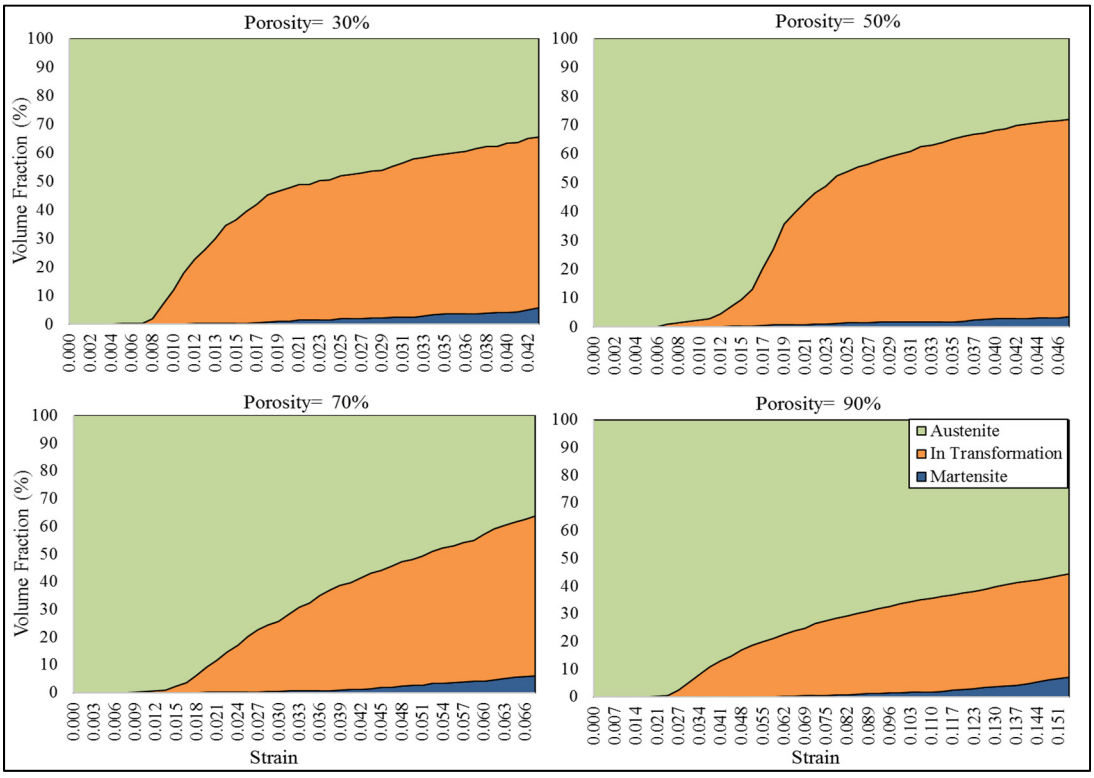

Figure 2.28 Volume fraction of material phases vs. apparent strain for BCC unit cell

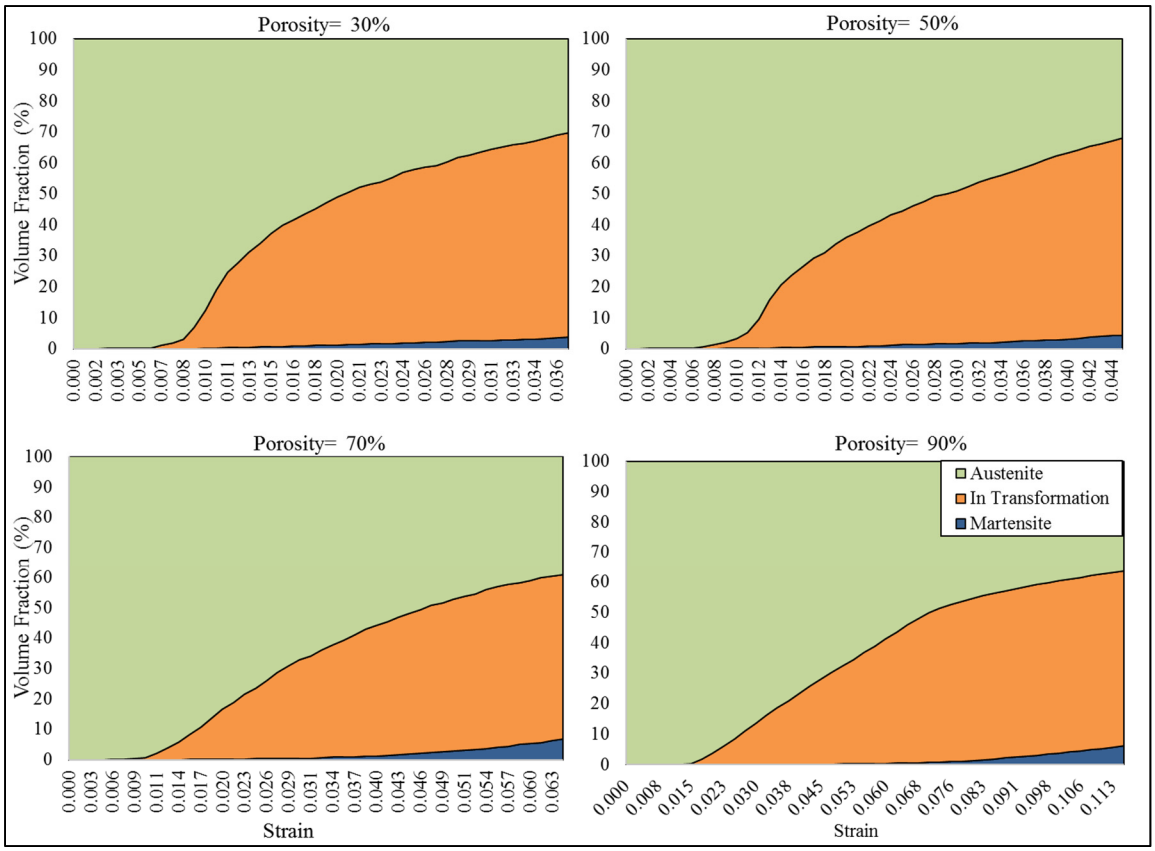

Figure 2.29 Volume fraction of material phases vs. apparent strain for F2BCC unit cell

As can be seen from the plots, very small percentage of the material fully transforms into martensite (blue) which are limited to high-stress areas of the unit cells, and the rest of the material in the unit cell either remains in austenite zone (green), or is in the process of transformation (orange).

2.2.6 Strain Energy Absorption and Dissipation Vs. Apparent Strain

A comparison of the strain energy absorption and dissipation of different unit cells can provide useful information regarding the capability of a lattice structure in shock absorption or vibration damping. The energy absorption and dissipation for all unit cells were plotted against porosity and are illustrated in Figure 2.30Figure 2.31. Although the values for energy

absorption are higher than those of energy dissipation, the unit cells rank similarly relative to each other.

In porosities between 10 to 40%, the spherical unit cell ranks highest, but drops sharply to the lowest of all unit cells for porosities of 50% and higher which is due to the geometric transition to open-cell topology along with presence of thin walls and sharp edges that limit the reversible strain.

Among the strut-based unit cells, the diamond unit cell exhibits the highest amount of energy absorption/dissipation across all porosities except for 10% where BCC exceeds the diamond unit cell. TKDH unit cell comes second in most porosities.

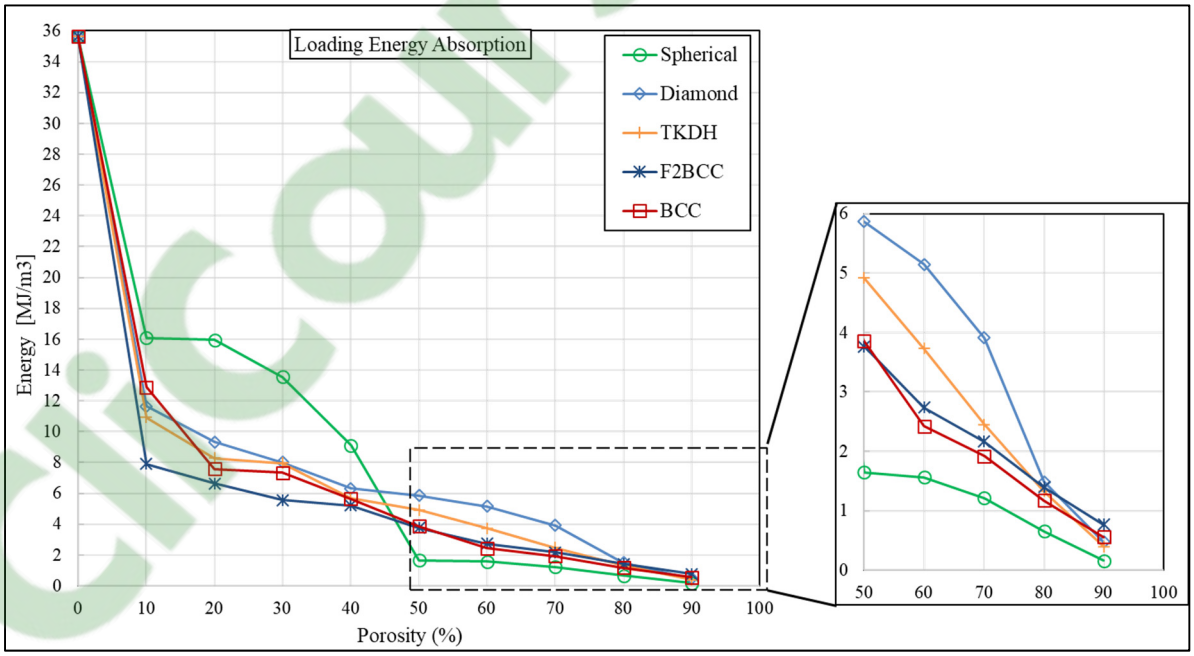

Figure 2.30 Strain energy absorption of different unit cells vs. porosity

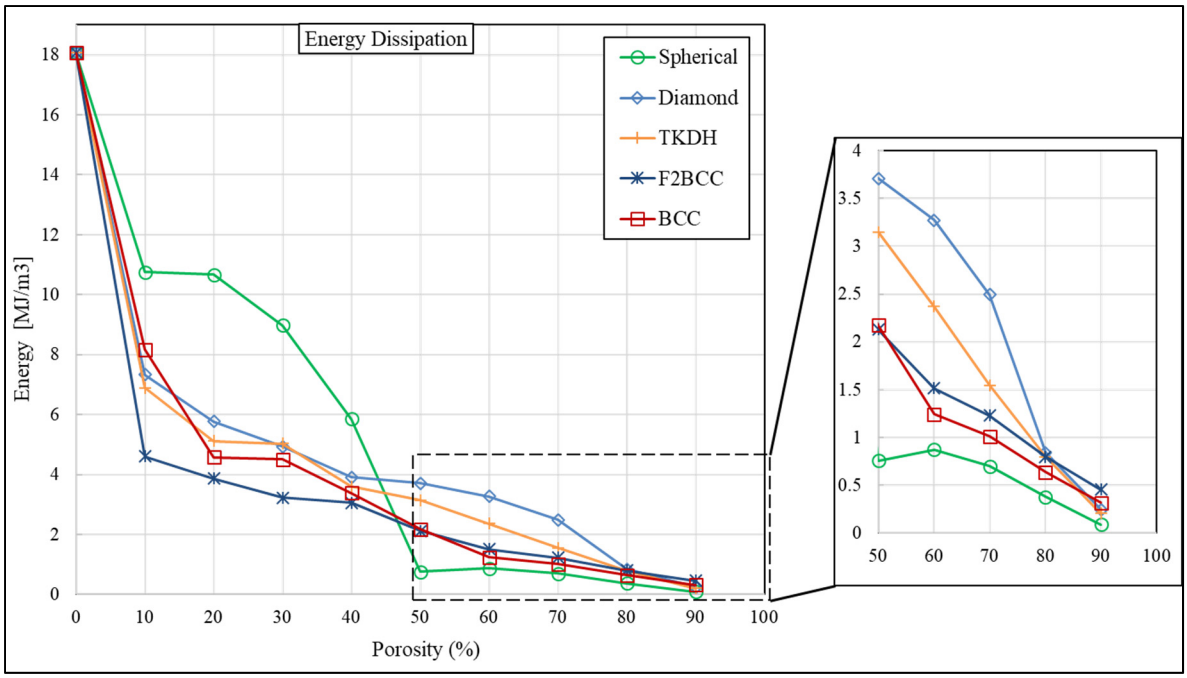

Figure 2.31 Strain energy dissipation of different unit cells vs. porosity

2.2.7 Addition of Fillets at the Strut Joints

The high stress concentration at the strut joints and sharp corners is a major factor in determining the reversible strain limit and the overall unit cell strength. An important aspect of additive manufacturing is the existence of imperfections that can lead to rounded edges. Therefore, we conducted a complementary set of FE analyses with a BCC unit cell with added fillets of different radiuses at the joints. The objective is to investigate how addition of fillets will affect the mechanical response of the unit cell. Four fillet radii of 0.05, 0.10, 0.15 and 0.20 mm were added to a 70% BCC unit cell. Note that by addition of the fillets, the porosity will also be altered. The geometries were modelled using Ansys Workbench. Figure 2.32 shows the geometries of BCC with four different fillet radiuses and corresponding porosities.

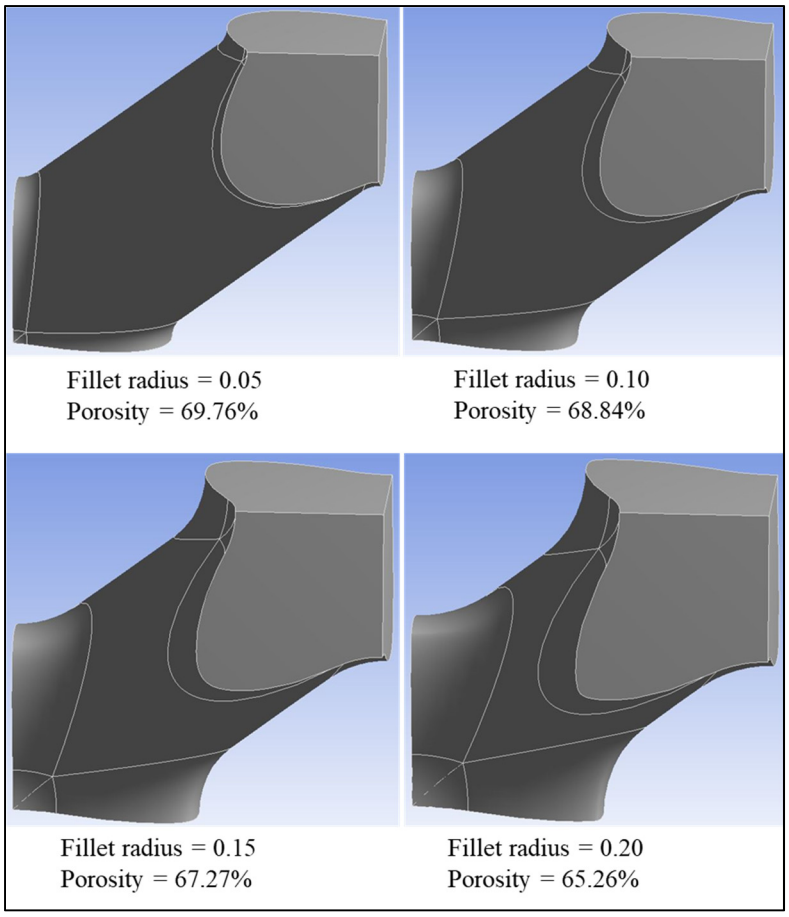

Figure 2.32 Geometry of BCC unit cell with four different fillet radiuses and corresponding porosities

The first set of analyses for determining the extent of reversible strain limit were performed. Figure 2.33 shows the Von Mises stress results for two fillet sizes at their strain limits with gray areas indicating the stresses over the 1100 MPa limit.

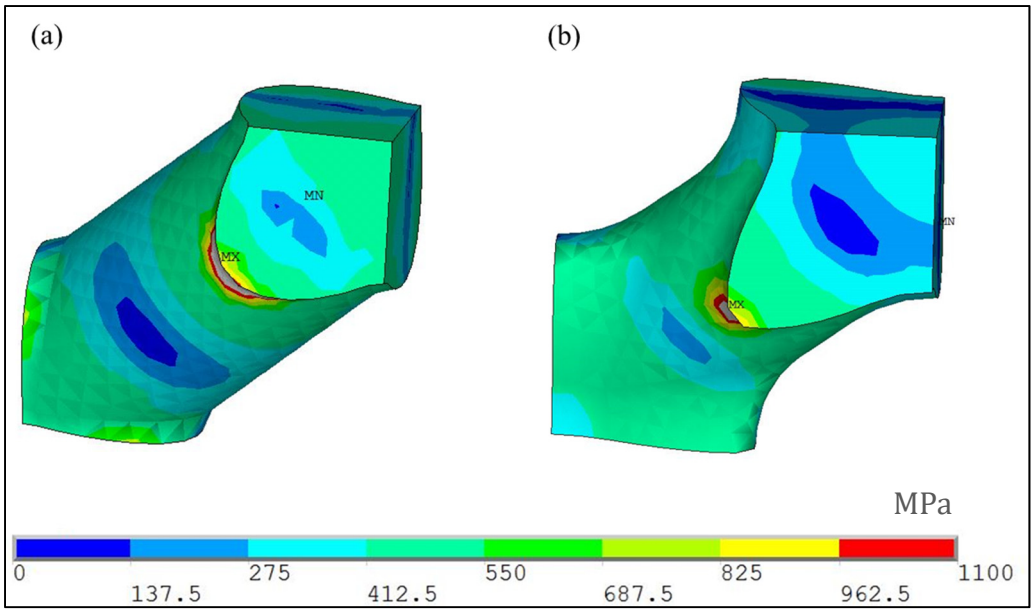

Figure 2.33 Von Mises stress results for BCC unit cell with (a) 0.05 mm fillet and (b) 0.20 mm fillet

These analyses give the maximum reversible apparent strain for each of the four geometries which are plotted together with the original BCC unit cell in Figure 2.34.

As can be seen in the plot, the addition of fillet causes the apparent strain limit to decrease for all fillet sizes compared to the BCC unit cell. This is because by adding fillet, material is added at the high-stress zones, so the criterion of 0.5% over limit is reached sooner during the loading. While this extra material helps to reduce the peak stresses at the corners, and overall reinforce the unit cell, the fillet material itself will be under high stress. This is evident in the figure above as the fillets fall into the gray areas.

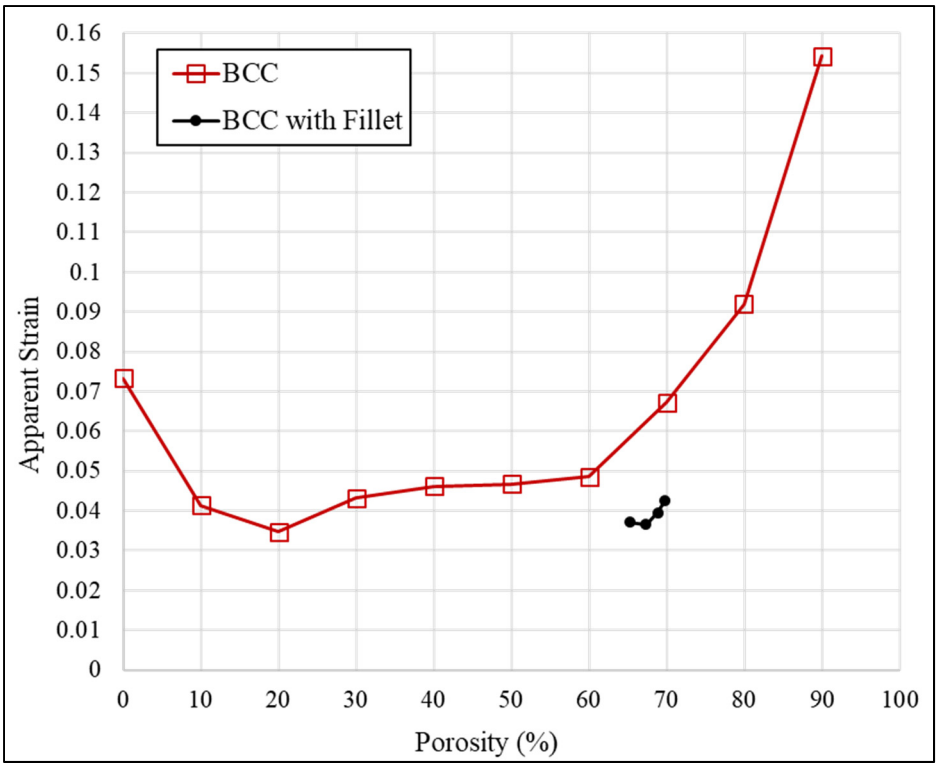

Figure 2.34 Apparent reversible strain of BCC with four fillet radiuses together with the BCC unit cell without fillet

After determining the reversible apparent strains, the FE analyses with load-unload cycles were conducted. Figure 2.35 depicts the apparent stress-strain curves of the BCC unit cell with four fillet sizes in comparison with the normal BCC of porosities 60% and 70%.

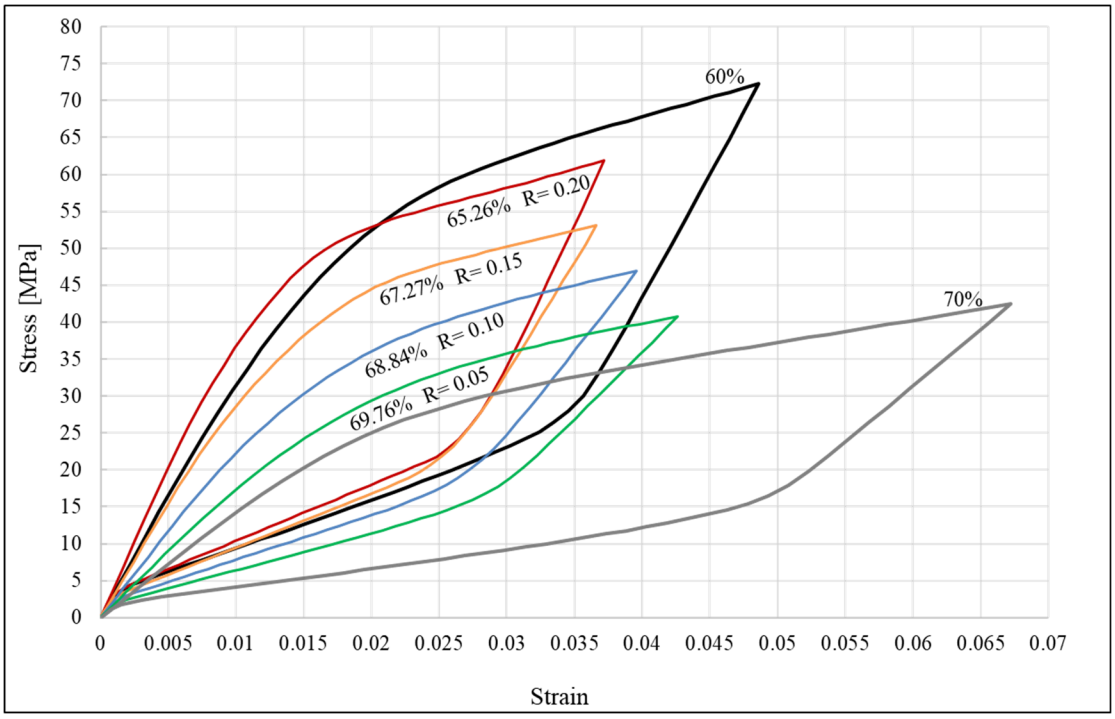

Figure 2.35 Comparison of apparent stress-strain responses of BCC unit cell with four different fillet sizes and the original 60 and 70% porosity BCC geometry without fillet

Using the apparent stress-strain curves, the initial elastic modulus (E_A) was calculated for all geometries. As expected, the addition of fillets increases the elastic modulus of the BCC unit cell due to the added reinforcement of the structure and reducing the stress concentration; see Figure 2.36.

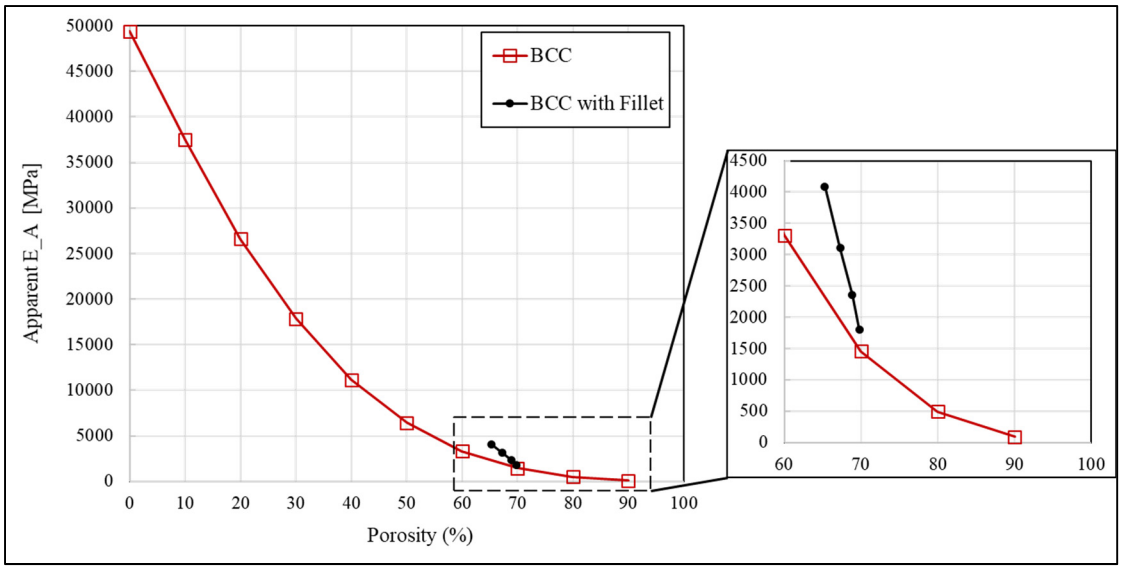

Figure 2.36 Comparison of apparent E_A between BCC unit cells with and without fillets

Finally, the energy absorption and dissipation values were calculated and are shown in Figure 2.37 and Figure 2.38.

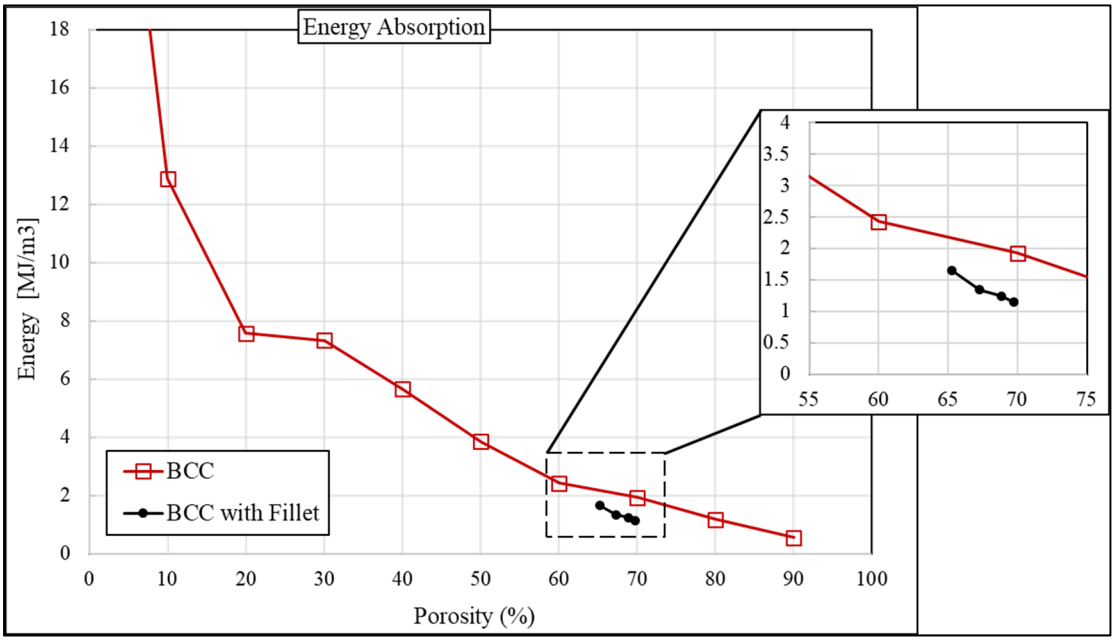

Figure 2.37 Strain energy absorption vs. porosity for BCC unit cell with four fillet sizes and the BCC without fillet

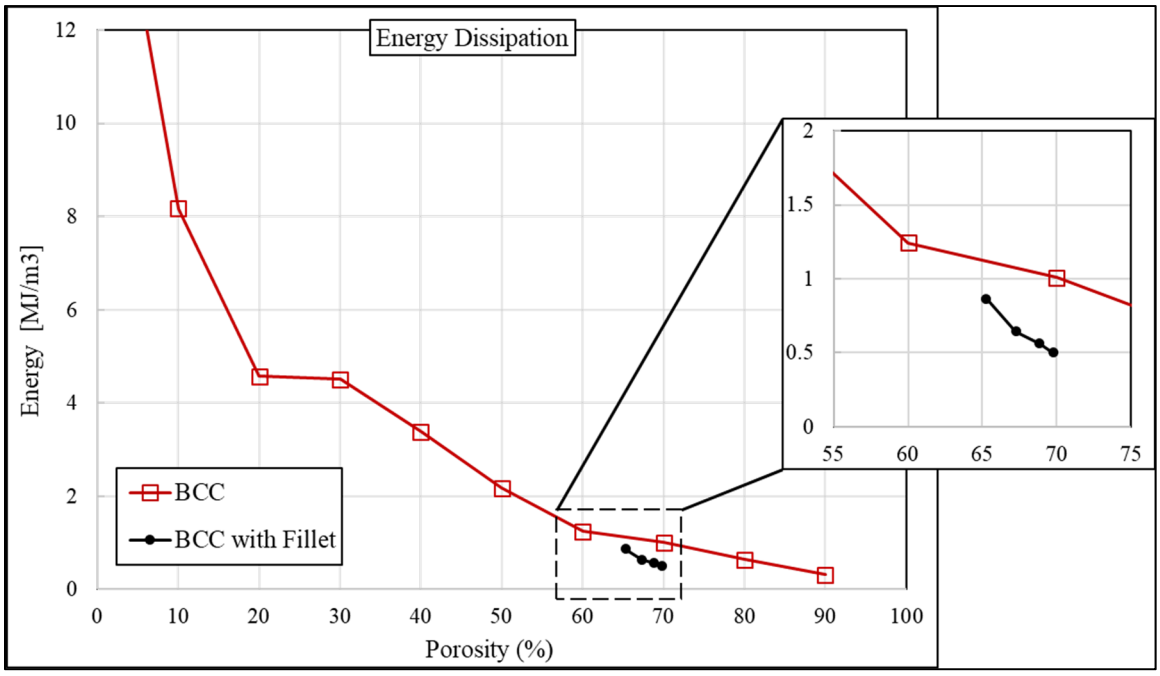

Figure 2.38 Strain energy dissipation vs. porosity for BCC unit cell with four fillet sizes and the BCC without fillet

The decrease in the strain energy values is mainly due to the decrease in the reversible apparent strain. Also, it should be noted that the increase in the initial elastic modulus can slightly increase the energy absorption in the beginning of the loading since it increases the apparent stress-strain slope in the linear part of the response, but its effect on the overall energy absorption is limited compared to the effect of apparent strain decrease.

These extra analysis results demonstrate the significant impact of rounded edges on the overall behavior of the unit cell. Here, the main analyses were performed on the idealized geometries with sharp edges. However, the experimental results with additively manufactured unit cells might differ from the simulation results as the manufactured samples usually contain rounded edges.

2.3 Concluding Remarks

By conducting UCFEM on five different unit cells, the influence of two main lattice structure design parameters, namely, geometry and porosity on the main mechanical characteristics of the unit cells were investigated. Considering the analysis results, the main conclusions can be outlined as follows:

- The reversible apparent strain for all geometries were determined by imposing limits based on the onset of plastic deformation. The threshold of 0.5% plasticity was set arbitrarily and can be modified according to any requirement.

- It was shown that all unit cells with all porosities exhibit superelastic behavior within their predetermined reversible strain range.

- For apparent elastic modulus and the reversible strain, the effect of the unit cell geometry becomes increasingly important. As the porosity increases, the range of variation between unit cells increase exponentially.

- By plotting the evolution of different material phases during the loading, it was shown that only a small percentage of the material in all the unit cells fully transforms into martensite from austenite. Although a large part of the unit cells do not undergo martensite transformation, macroscopic superelastic response can still be observed. However, the small amount of transformation, especially for higher porosities, limits the superelastic behavior of the unit cell.

- The energy absorption and dissipation calculations provide some insight and comparison basis between different unit cells and can be useful for applications where shock absorption or vibration damping is expected.

- It was shown that addition of rounded edges to the geometry of unit cells has a significant effect on the mechanical response of the unit cell. Since AM creates rounded edges, among other imperfections, it is of great importance to further investigate the effects of AM on the experimental results and their deviation from the simulated ones.

- The set of analyses and post-processing routines presented here are used as an example for only uniaxial loading. However, all these procedures can easily be expanded to various other loading types to suite a specific design requirement.

CHAPTER 3

EXPERIMENTAL VALIDATION OF THE SMA MATERIAL MODEL IN THE CURRENT FE PROGRAMS

Remark: The content of this chapter, in a shorter form, has been published as an article (Khodaei and Terriault 2018)

Modeling of the macroscopic mechanical response of porous SMAs requires taking into account the fact that the material within the porous substructure is subjected to a three-dimensional state of stress, and due the large variation of the stress field across the structure, any material point will be at a different stage of the transformation process. Furthermore, the material usually undergoes different loading paths, and since the thermomechanical response of SMAs is dependent on the loading path (Azadi, Rajapakse et al. 2007), it is of importance to verify the performance of any material model in reproducing these aspects of the SMA behavior. Although numerous constitutive models have been proposed in the academic community, Auricchio's model (Auricchio 2001) is currently the only model incorporated in the commercial Finite Element (FE) software (e.g. Ansys and Abaqus) with an acceptable level of numerical efficiency and robustness. Auricchio's model has a 3D formulation and is developed based on the generalized plasticity theory, where the inelastic transformation strains are treated as plastic deformation. This model is able to reproduce the superelastic response of SMAs as well as tension-compression asymmetry. Because of the simplicity of this model, only a few material parameters need to be determined, and the only internal variable governing the transformation is the volume fraction of martensite. The material parameters involved in this model can easily be determined through uniaxial experimental tests.

Following the second objective of this thesis mentioned in the Introduction, in this chapter the accuracy of Auricchio's model in predicting the multiaxial and path dependency of the SMA material behavior will be investigated against experimental test data. This study will focus only

on the SE aspect of this model, as the target application will be porous SE implants under the isothermal condition.

The experimental validation of the simulated response of the material is a crucial step in evaluating the performance and fidelity of any constitutive model. Several studies have investigated the mechanical response of SMAs under different conditions, such as uniaxial loads (Brinson, Schmidt et al. 2004, Williams and Elahinia 2008, Hartl, Lagoudas et al. 2009), multiaxial tension-torsion (Sittner, Hara et al. 1995, McNANEY, Imbeni et al. 2003) and multiaxial, non-proportional loadings with various loading paths (Grabe and Bruhns 2009). In a more recent experimental work, NiTi tubes were characterized under tension, compression and pure bending loads (Reedlunn, Churchill et al. 2014). To obtain the material parameters for the constitutive model in the FE software such as Ansys, experimental data from uniaxial test should be used. While some studies provide a wide range of test data, it was not possible in this case to accurately obtain those material parameters and apply them to multiaxial, path-dependent tests that were done under the same test condition as the uniaxial one. Hence, to obtain the values for material parameters needed for the Auricchio's model, new experiments were performed.

The first part of this chapter presents the testing, measurement and FE modeling procedure. A uniaxial test was performed on thin-walled NiTi alloy samples for material characterization and to determine the needed material parameters. Multiaxial tests with different loading paths were also applied on similar samples at the same temperature to demonstrate the path-dependent behavior of the SMA. With the necessary experimental data produced, an FE model of the specimens was then created using the Ansys FE software, where the SMA material based on Auricchio's model was assigned, and the exact loading sequences were applied to the model. A separate test was also performed with thermal measurements in order to monitor the temperature change in the samples during the test.

In the second part, numerical and experimental results are compared in order to investigate the ability of the material model to reproduce the uniaxial, as well as multiaxial path-dependent response.

3.1 Material and Methods

3.1.1 Samples

Experiments were carried out on thin-walled tubes having an outer diameter of 10 mm and a wall thickness of 0.2 mm, giving a radius-to-wall-thickness ratio of 25:1. The samples were cut from a tube approximately 1 meter long. Each sample had a total length of 70 mm, of which 20 mm at each end was used for grip jaws of the testing machine, and a snug-fitting steel rod with a 9.5 mm diameter was inserted and glued to support the sample under the grip force. In the middle portion of the sample, a separate piece of the same rod was inserted without gluing, allowing tensile and torsional deformations, but preventing the sample from buckling inwards under torsional loads. The geometry of the samples and the elastic modulus of the material imposes a buckling stress limit for compression and torsion (Batdorf, Stein et al. 1947), which makes it impractical to apply a compressive load high enough to reach the transformation stress. Buckling under torsion was prevented by adding an initial tensile load for all loading paths.

It should be noted that the instructions of ASTM F2516-14 (ASTM-F2516-14) regarding the tensile testing procedure of NiTi alloys were not entirely followed for this sample since the nature of the tests, especially the multiaxial ones, is different in this study. The strains were measured on an area far enough from the clamped edge to avoid local stress irregularities. A schematic drawing of the sample is shown in Figure 3.1.

The alloy in the samples was medical grade NiTi provided by Euroflex GmbH, Germany, composed of 54.5 - 57% Nickel in terms of weight, and was trained prior to delivery. The

austenite finish (A_f) temperature was stated by the company to be 15°C, and consequently, the material was expected to exhibit a full SE cycle at a room temperature of 24°C.

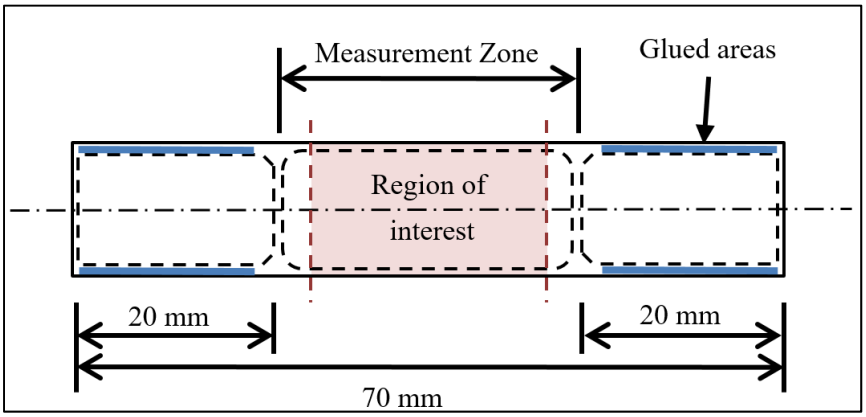

Figure 3.1 Schematic drawing of the sample, including the inserts

3.1.2 Experimental Tests

3.1.2.1 Testing Equipment

The tests were performed using an MTS 858 Minibionix testing machine (MTS Systems Corporation Eden Prairie, MN, USA). This machine is equipped with hydraulic wedge grips and is able to exert both axial and torsional loads.

3.1.2.2 Strain Measurement

The strain in the sample was measured using an Aramis 3D digital image correlation (Badiche, Forest et al.) system, together with GOM Correlate software (GOM GmbH, Braunschweig, Germany). Using two 5-megapixel camera sensors, this system can measure and track the evolution of the strain field over a specified area of the sample that is painted by a suitable speckle pattern. By observing the strain field during the test, it is possible to distinguish and exclude the local strain irregularities mostly close to the grip. The strain measurement was performed by defining multiple distance lines across the region of interest and averaging the

calculated strain values. Six distance measurement lines for strain, shown in Figure 3.2(a), and nine sample points for angular strains, shown in Figure 3.2(c), were used to produce the averaged strain data. An example of the strain field across the surface of the sample during the tensile and torsional tests is depicted in Figure 3.2(b) and (d).

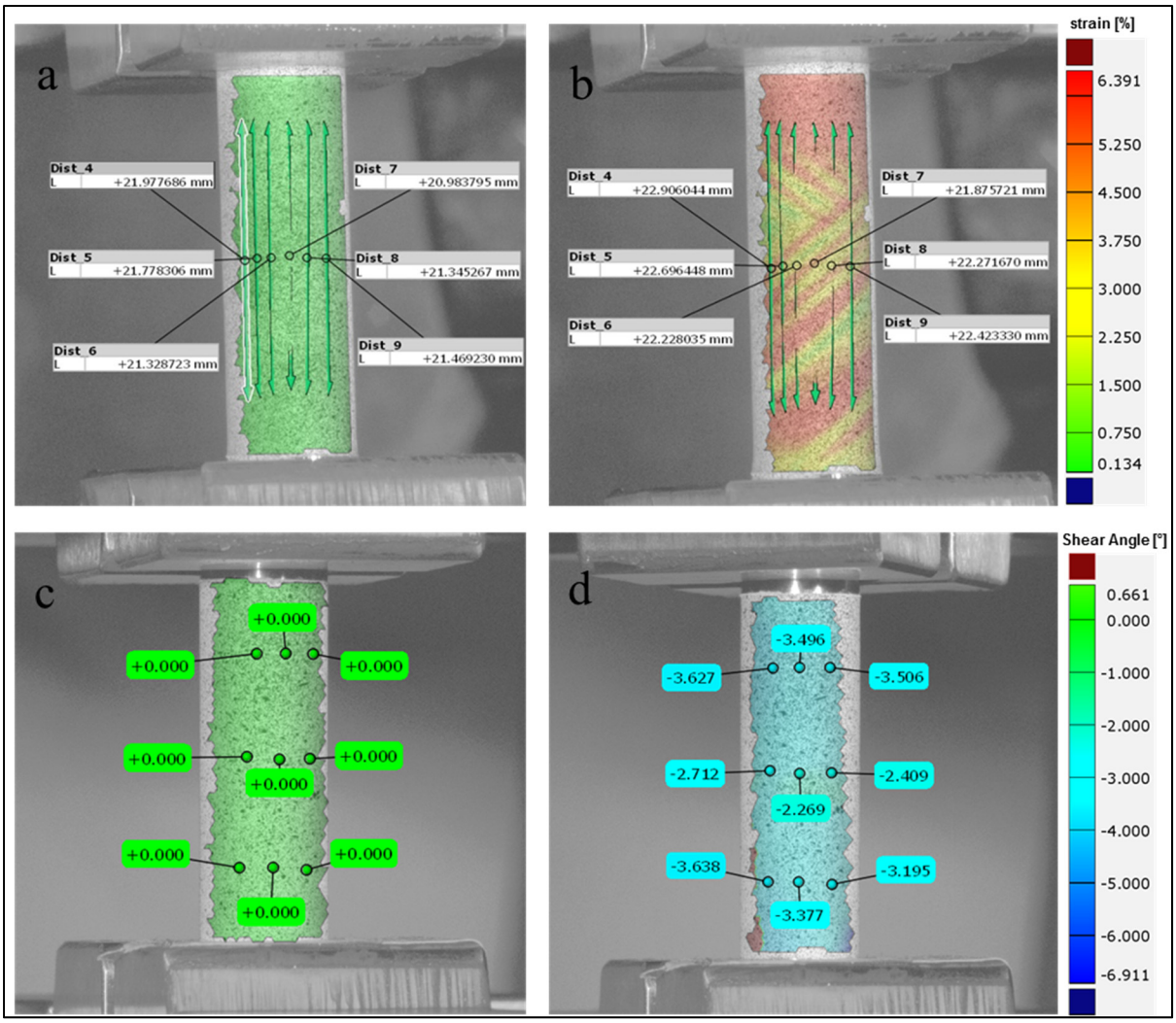

Figure 3.2 Strain measurement of the NiTi tube samples using Digital Image Correlation (Badiche, Forest et al.): (a) un-deformed sample before tensile stretch, (b) deformed sample under tensile force, (c) un-deformed sample before torsion, (d) deformed sample under torsion

The strain field in Figure 3.2(b) exhibits the localized deformation phenomenon (Orgéas and Favier 1998) demonstrated by bands of high-strain transformation regions, also known as

Luders bands. This signifies the necessity of sampling the strain over multiple locations to obtain a better estimate of the overall macroscopic strain of the material.

3.1.2.3 Tensile Test

Two different tensile tests were performed. The first tensile test was carried out to the point of fracture in order to establish the full range of the material response and its ultimate stress. This test was displacement controlled, with the rate of 0.05 mm/s, with the total displacement set to a large value of 25 mm, in order to ensure that the sample would reach the fracture point.

The second tensile test was performed to determine the key material parameters: elastic modulus for austenite (E_A) and martensite (E_M), maximum transformation strain (ε_L) and transformation stresses, martensite start (σ_{ms}), martensite finish (σ_{mf}), austenite start (σ_{as}), and austenite finish (σ_{af}). The sample was stretched up to well above the full transformation stress (σ_{mf}), and then unloaded to produce the full hysteresis cycle. The resulting curve produced by this test also provides the needed information for determining the stress levels in the tensile direction in the multiaxial tests. For this test, the force controlled setting with a rate of 17.96 N/sec or 2.91 MPa /sec (based on the tube cross-section area of 6.157 mm^2) was applied. The applied stress was increased up to a maximum of 700 MPa and reduced back to zero. The maximum applied stress value was taken from the observed response of the sample in the first tensile tests, and is the stress level at which the material has clearly passed the full transformation.

3.1.2.4 Shear Test

The shear test was performed in order to determine the plateau shear stress which would then be used as a guide to set the shear load level in the multiaxial tests. A torsional load was applied to the sample to create pure shear stress in the tube. Two tests were carried out: first, three successive load cycles with increasing magnitude were applied to examine the extent of transformation and the reversibility of the material; in the second test, the sample was twisted

with a magnitude beyond the full transformation stress up to fracture. The testing machine was set to twist angle control mode, at a rate of 0.5 degrees/sec.

3.1.2.5 Multiaxial Path Dependent Tests

Based on the tensile and shear tests, two different loading paths were designed to exhibit the path-dependent behavior of the material. Both paths start with an initial pretension stress of 200 MPa to ensure that no bucking under the torsional load occurs. Figure 3.3 shows the two different loading paths applied to the sample.

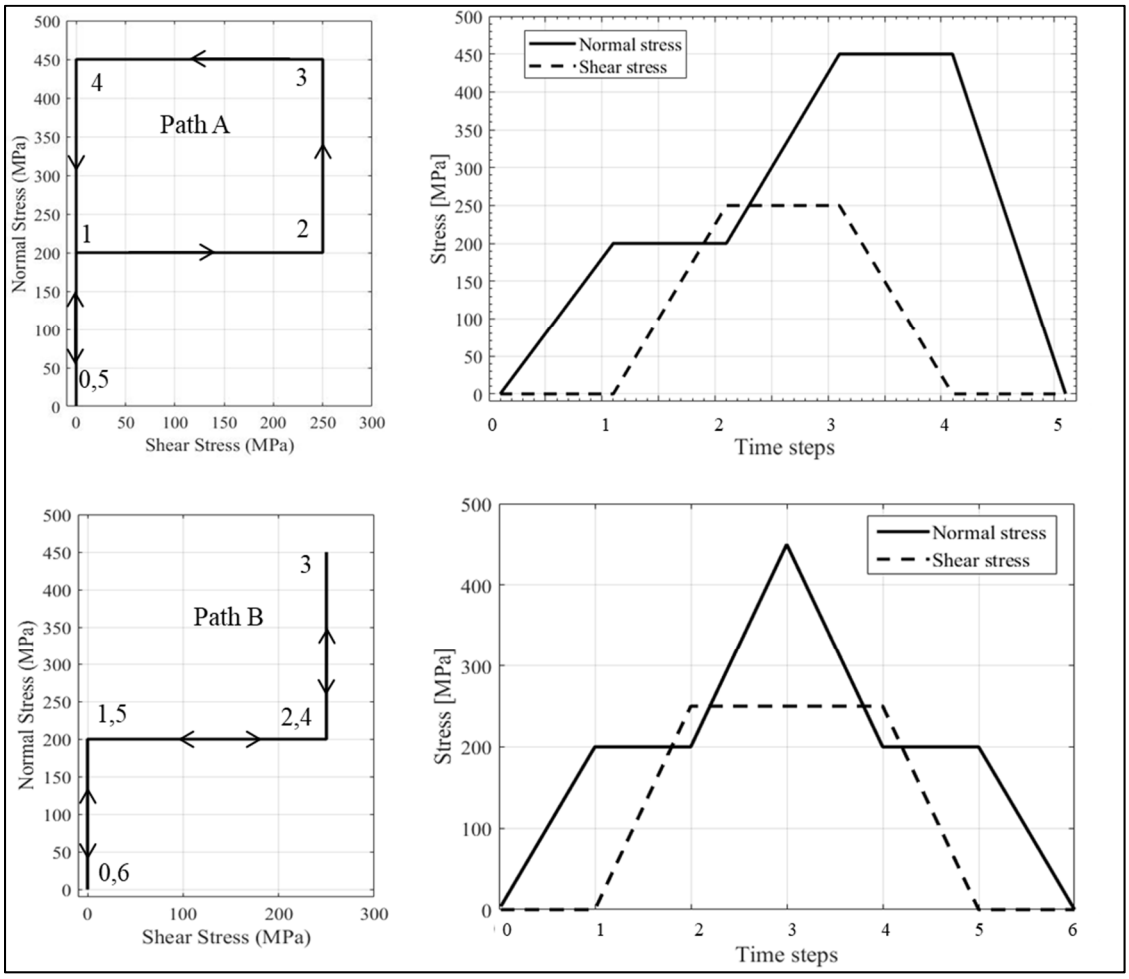

Figure 3.3 The multiaxial loading history – Paths A and B. The numbers in each path diagram on the left correspond to the step numbers in the graph on the right.

To perform these tests, the testing machine was set to force and torque-controlled mode. To maintain a consistent number of data points throughout the loading path captured by the Aramis system, the rate of the loading was adjusted, and ranged between 2 and 4.2 MPa/s. The loading rates were low enough to prevent significant temperature rise in the specimen due to phase transformation and the self-heating effect (Torra, Carreras et al. 2014). For the multiaxial test (path A), the temperature was measured using a thermal imaging camera. Some temperature variations were observed with the maximum temperature change momentarily reaching 4.4°C.

3.1.3 FE Modeling

To simulate the mechanical behavior of the NiTi samples, an FE model was built using Ansys Mechanical APDL 15.0 (ANSYS Canonsburg, PA, USA), based on the geometry of the test samples.

3.1.3.1 Geometry

A hollow cylinder with an outer diameter of 10 mm and inner diameter of 9.6 mm was created according to the dimensions of the sample tubes. Only the middle portion of the sample with a length of 30 mm was modeled, and the gripped ends were excluded.

3.1.3.2 Material Model

The Ansys software's built-in constitutive model for superelastic materials, based on the Auricchio model (Auricchio 2001), was assigned to the elements. The parameters used for the material model were based on the uniaxial tensile test results which will be presented in the Results section.

3.1.3.3 Mesh

The model was meshed using 1520 linear 8-node solid elements with an average size of 0.8 mm. Note that the use of 20-node non-linear solid elements was not supported with the SMA material model. A mesh convergence analysis was performed to ensure that further mesh refinement would not improve the accuracy of results significantly. Figure 3.4 illustrates the meshed FE model.

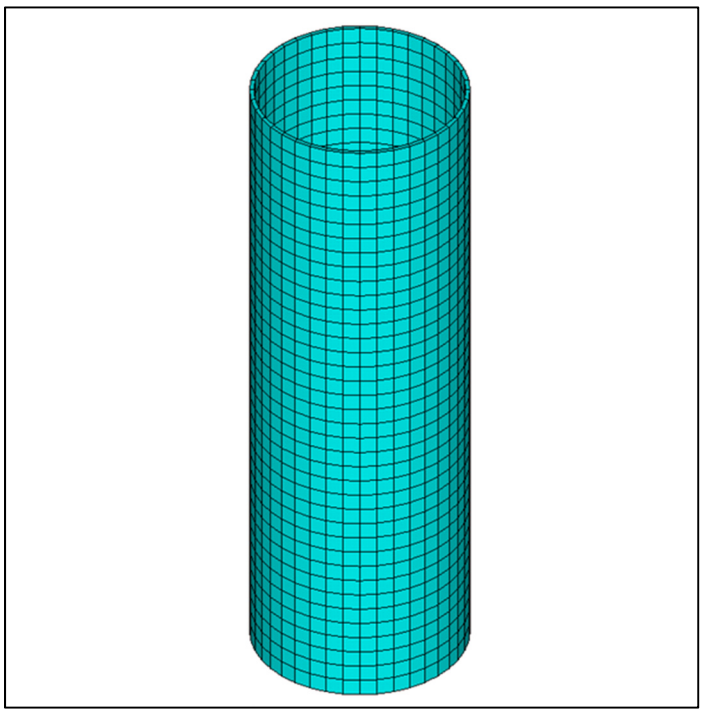

Figure 3.4 Meshed FE model of the test sample

3.1.3.4 Boundary Conditions and Loading

A local cylindrical coordinate system, with its z axis along the centerline of the tube, was defined for easier assigning of the boundary conditions and loads. The nodes at the bottom end of the model were fixed in all three DoFs ($U_R = U_\theta = U_Z = 0$), and at the top end, the outer circumferential nodes were fixed in radial direction ($U_R = 0$), in order to account for the effect of the grips and the glued inserts. The axial and circumferential DoFs of the same nodes were

used to apply tensile force F_z and torque M_z. Figure 3.5 shows the applied coundary conditions and loads.

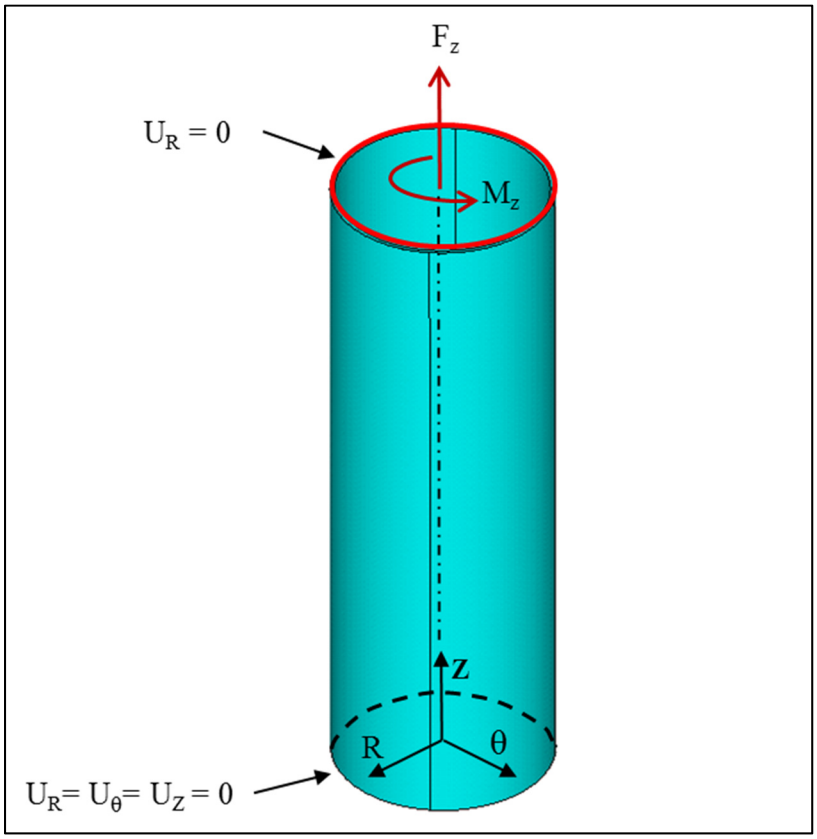

Figure 3.5 Loads and boundary conditions applied to the FE model of the NiTi tube

3.1.3.5 Analysis and Post-processing

A nonlinear, large displacement solution method was used in the software. Uniaxial, as well as multiaxial load cases with two different paths, similar to those of the experimental tests, were applied to the model to evaluate the accuracy of the Auricchio's model in predicting the mechanical response of the material. The strain results were extracted at the middle of the tube on the outer surface.

Figure 3.6 depicts an example of the normal stress distribution of the model under a combined tensile and torsional load. As can be seen in the figure, except for the two ends of the model,

the stress distribution is mostly uniform. Extracting the results at the middle of the model ensured that local boundary effects would not disrupt the results.

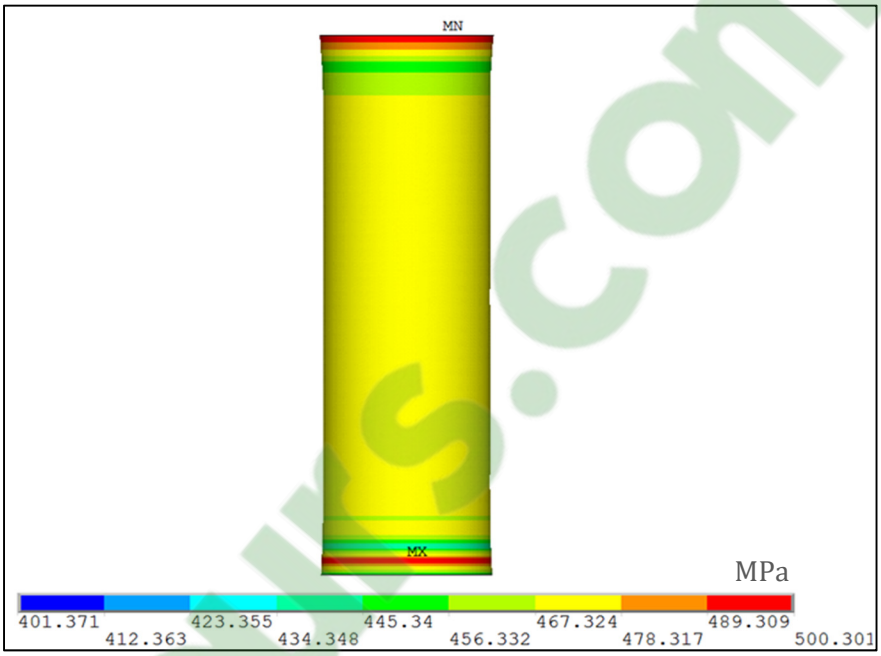

Figure 3.6 Stress distribution under a combined tensile and shear loading state

3.2 Results and Discussions

The mechanical responses of the NiTi samples were obtained using the optical DIC method described in the previous section. The stress-strain curves representing the material behavior were produced for each testing case. The results from the FE simulations are provided and compared with the corresponding experimental results.

3.2.1 Uniaxial Tensile Test and Determining Material Model Parameters

The stress-strain curve representing the response of the NiTi material and the full hysteresis cycle associated with the MT under the uniaxial tensile loading/unloading was obtained. A comparison also was made between the FE result and that of the experimental tests.

The uniaxial tensile test results were used to determine the material parameters needed for the constitutive model in Ansys. The modulus of elasticity for austenite, E_A, and martensite, E_M, were 49.4 GPa and 22.8 GPa, respectively, and were obtained by determining the slope of the linear parts of the graph before and after the MT. An averaged value of 36 GPa was considered for the material model in the FE software as it uses only a single value. The reason for using the average of E_A and E_M was that the simulated curves made closer approximation of the experimental curves.

The maximum transformation strain, ε_L, was measured to be 4.8%. The extracted parameters on the experimental curve are shown in Figure 3.7(a), and are summarized in Table 3.1. A comparison between the experimental results and those of the corresponding FE simulation is shown in Figure 3.7(b).

As can be seen in the figure, the material model was able to closely reproduce the experimental behavior of the material under uniaxial loading. Note that the tension-compression asymmetry parameter, α, was not experimentally determined since the compression tests could not be carried out on the samples due to the very thin wall of the sample tube and the occurrence of buckling. Therefore, it was assumed to be 0, meaning that the material would behave identically in tension and compression. However, the parameter α can be influential in the overall behavior of the model, considering the fact that compressive stresses are created in the material during shear loadings. The effect of this parameter was investigated, and results are discussed in section 3.2.4.

Table 3.1 Material parameters used in the FE analyses

Young's modulus, E [MPa]	36000
Poisson's ratio, ν	0.3
Martensite start stress, σ_{ms} [MPa]	403
Martensite finish stress, σ_{mf} [MPa]	544
Austenite start stress, σ_{as} [MPa]	169
Austenite finish stress, σ_{af} [MPa]	28
Transformation strain, ε_L [%]	4.8
Tension-compression asymmetry parameter, α	0

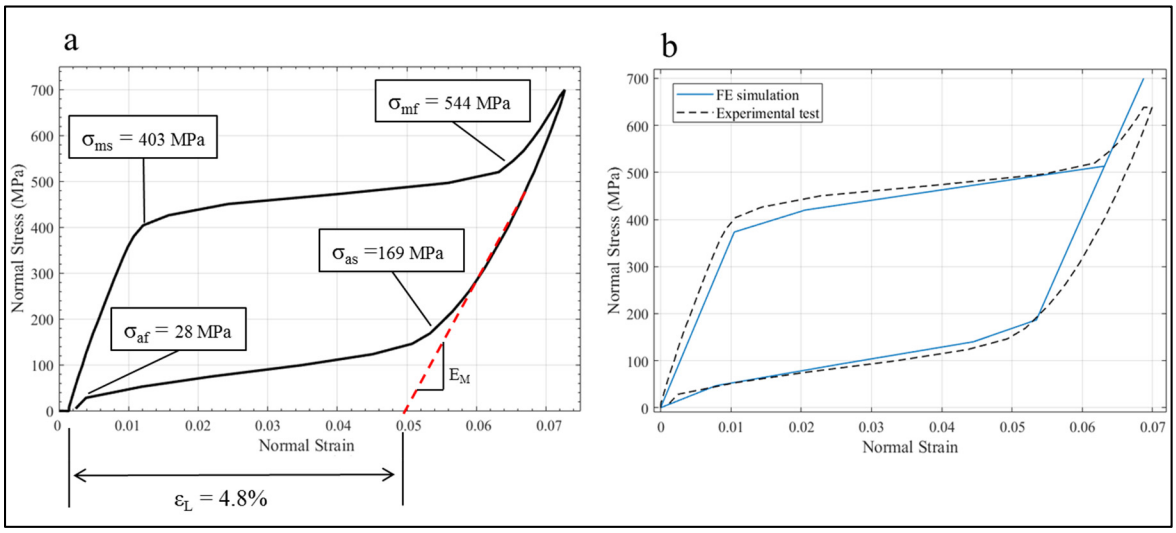

Figure 3.7 Superelastic behavior of NiTi alloy under uniaxial tensile cycle: a) Material parameters determined from the experimental curve, b) Comparison of the experimental with FE simulated results

3.2.2 Shear Test

The results of pure shear tests on the NiTi sample are shown in Figure 3.8. The martensite transformation occurred between 300 and 350 MPa, approximately. These values, in comparison with corresponding values in the tensile test, were considered as a guide for determining the loading levels in shear and tension in the multiaxial tests. Under the three

progressive cycles, the material exhibited good reversibility, with insignificant residual strain, proving that the material was trained prior to delivery.

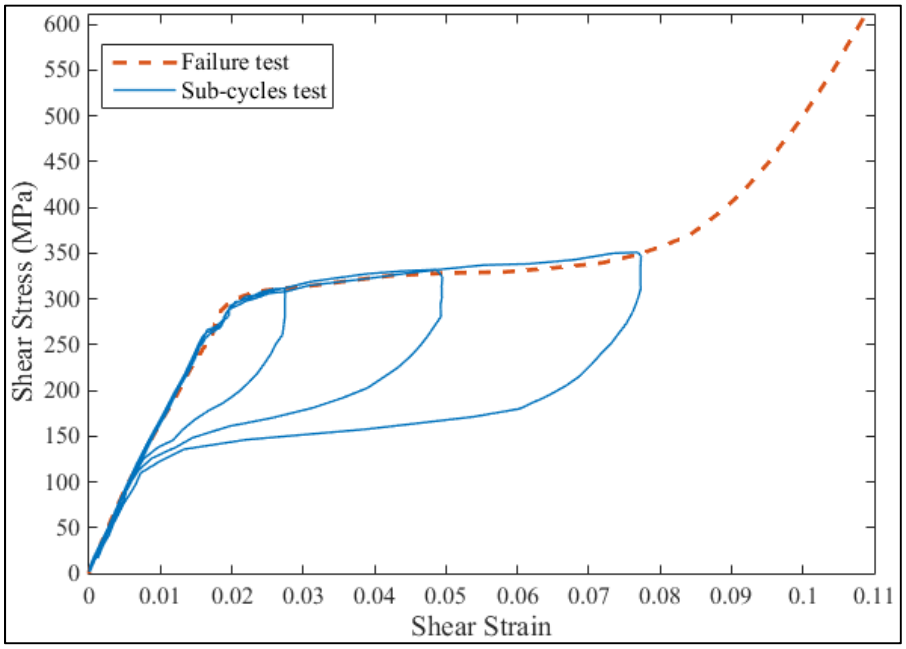

Figure 3.8 Mechanical response of the NiTi alloy under shear loading, including transformation sub-cycles

3.2.3 Multiaxial Load Cases

In order to evaluate the accuracy of Auricchio's model in Ansys FE software under multiaxial loads, comparisons were made between the experimental tests and FE simulation results for the multiaxial loading paths, A and B. The results are presented in stress-strain plots separately for tensile and shear, as well as normal vs. shear strain plots. The comparison plots for both multiaxial loading paths are shown in Figure 3.9 and Figure 3.10.

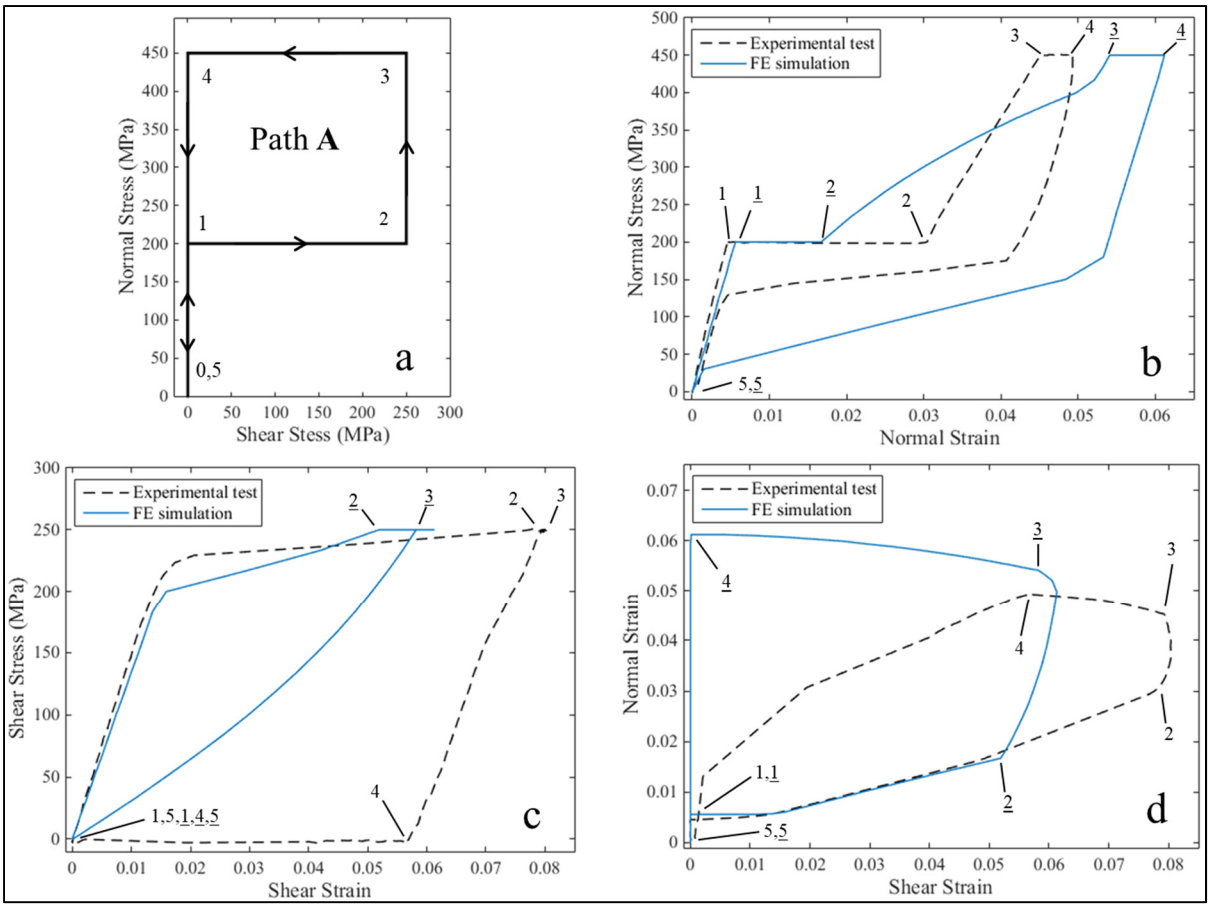

Figure 3.9 FE results compared with experimental data under multiaxial load path A. The numbers on each curve indicate the loading step numbers (FE step numbers are underlined) (a) Loading path, (b) normal stress-strain response, (c) shear stress-strain response, (d) normal vs. shear strain response

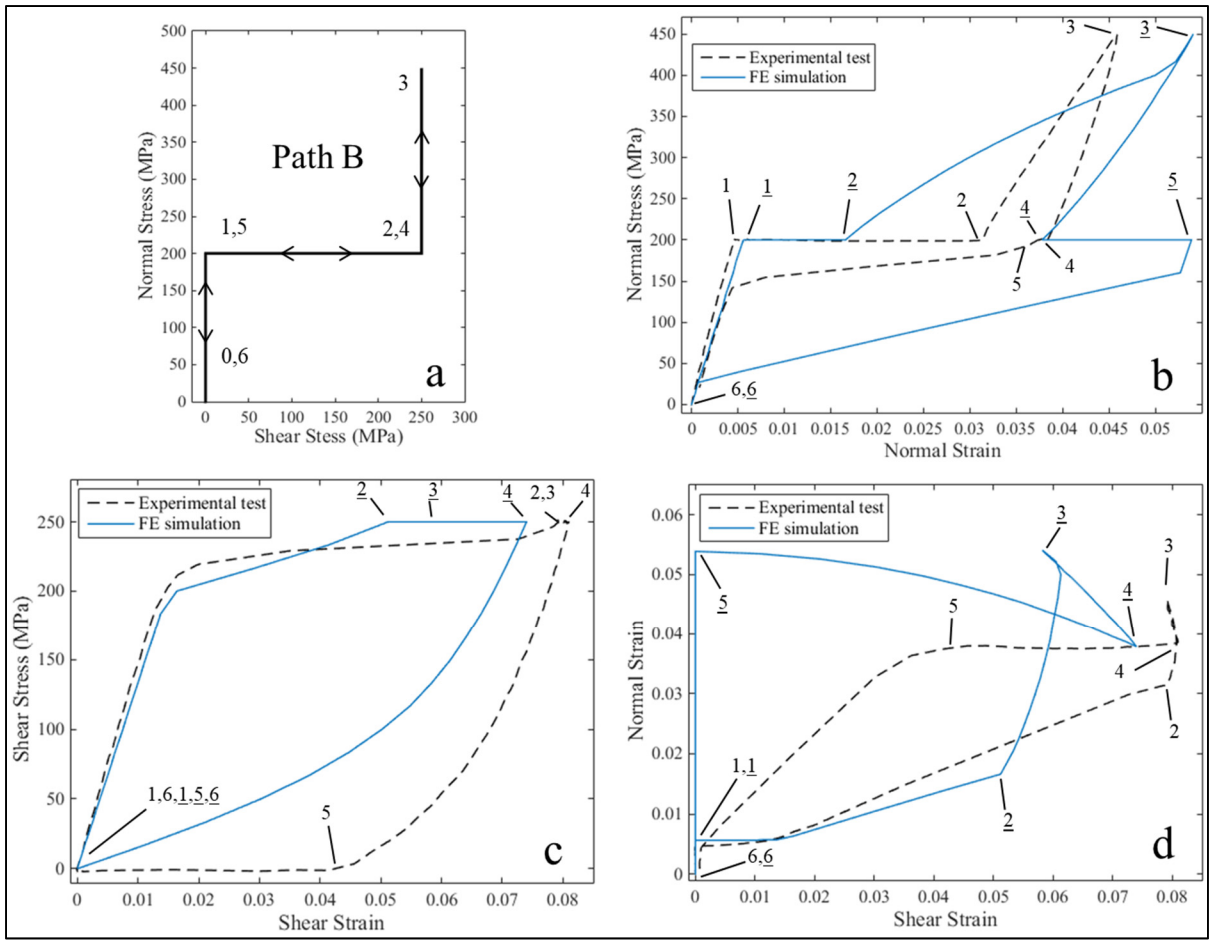

Figure 3.10 FE results compared with experimental data under multiaxial load path B. The numbers on each curve indicate the loading step numbers (FE step numbers are underlined) (a) Loading path, (b) normal stress-strain response, (c) shear stress-strain response, (d) normal vs. shear strain response

By comparing the results, it can be seen that while this constitutive model is able to exhibit some aspects of the path-dependent behavior, there is a poor agreement between the general mechanical behavior of the tests and that of the constitutive model. Also, in general, the model tends to overestimate the normal strain while underestimating the shear strain.

3.2.4 Parameter Study of α

Since an experimentally validated value for α was not available, the FE simulations presented above were carried out using a value of 0 for this parameter, hence assuming a symmetric

behavior for tension and compression. This parameter is calculated through the following formula in Ansys:

$$\propto = \frac{\sigma_c^{AS} - \sigma_t^{AS}}{\sigma_c^{AS} + \sigma_t^{AS}} \tag{3.1}$$

where σ^{AS} is equivalent to martensite start stress, σ_{ms}, and the subscripts c and t denote compression and tension, respectively. As an example, with a value of $\alpha = 0.1$, and a given value of σ_{ms}=403MPa, the compressive transformation stress would be 492.5 MPa, which means approximately 22% difference in the transformation stresses in tension and compression.

Although compressive loads are not present in the loading paths, shear loadings will results in normal compressive stress components in the material. This makes α an important parameter. Therefore, a parameter study was performed to investigate the effect of α in the overall response of the material model. In lack of an experimentally validated value, α was treated as a calibration parameter in uniaxial shear load case, so a series of FE simulations with different α values were performed in order to find the closest match between the simulated result and the experimental curves. This attempt was motivated by the fact that in pure shear load case, the material model, with an α value of 0, exhibits a significant overestimation of shear strains as shown in Figure 3.11. This figure also demonstrates the FE results of uniaxial shear loading with different α values in comparison with the experimental curves.

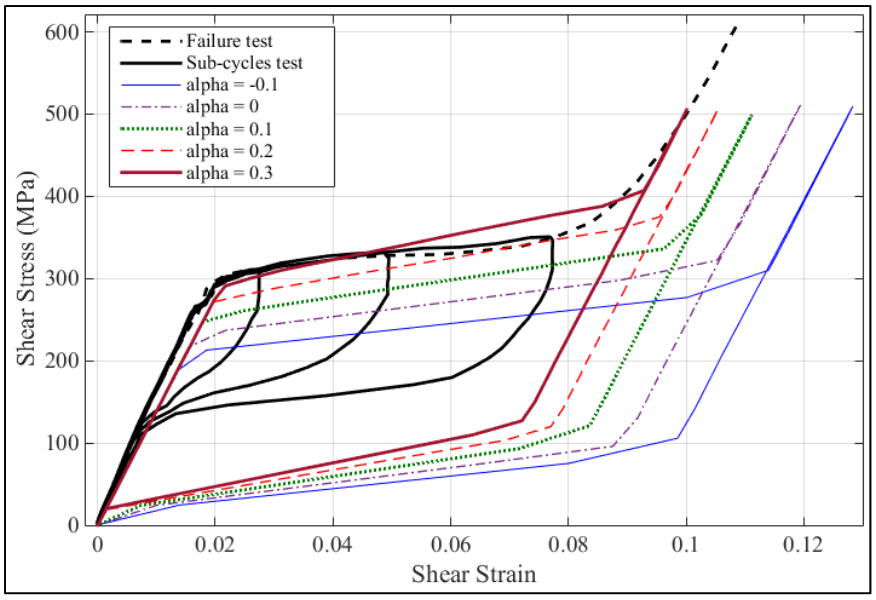

Figure 3.11 FE results with different α values compared with the experimental test under the uniaxial shear loading

As a result of these simulations, it was found that an α value of 0.3 leads to the closest prediction of the shear strain, however, the model tends to exhibit wider hysteresis cycle in all simulations.

Having found the α value that best matches the shear strain, a new set of simulations for multiaxial loading paths A and B were performed and the results were compared with the experimental curves, as well as ones generated by FE simulations with α value of 0. The results are demonstrated in Figure 3.12 andFigure 3.13.

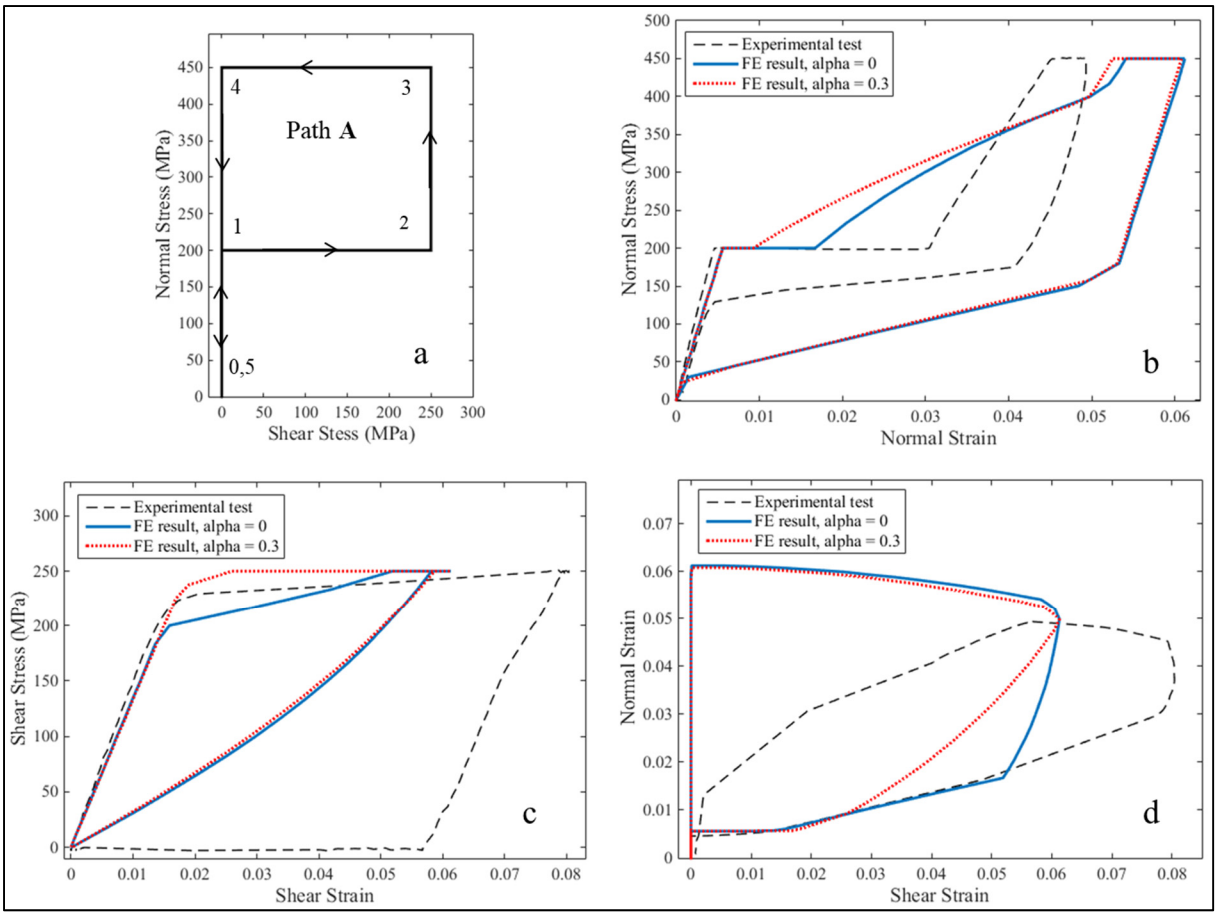

Figure 3.12 FE results with α values of 0 and 0.3 compared with the experimental test under the multiaxial loading path A. (a) Loading path, (b) Normal stress-strain response, (c) Shear stress-strain response, (d) Normal vs. shear strain response

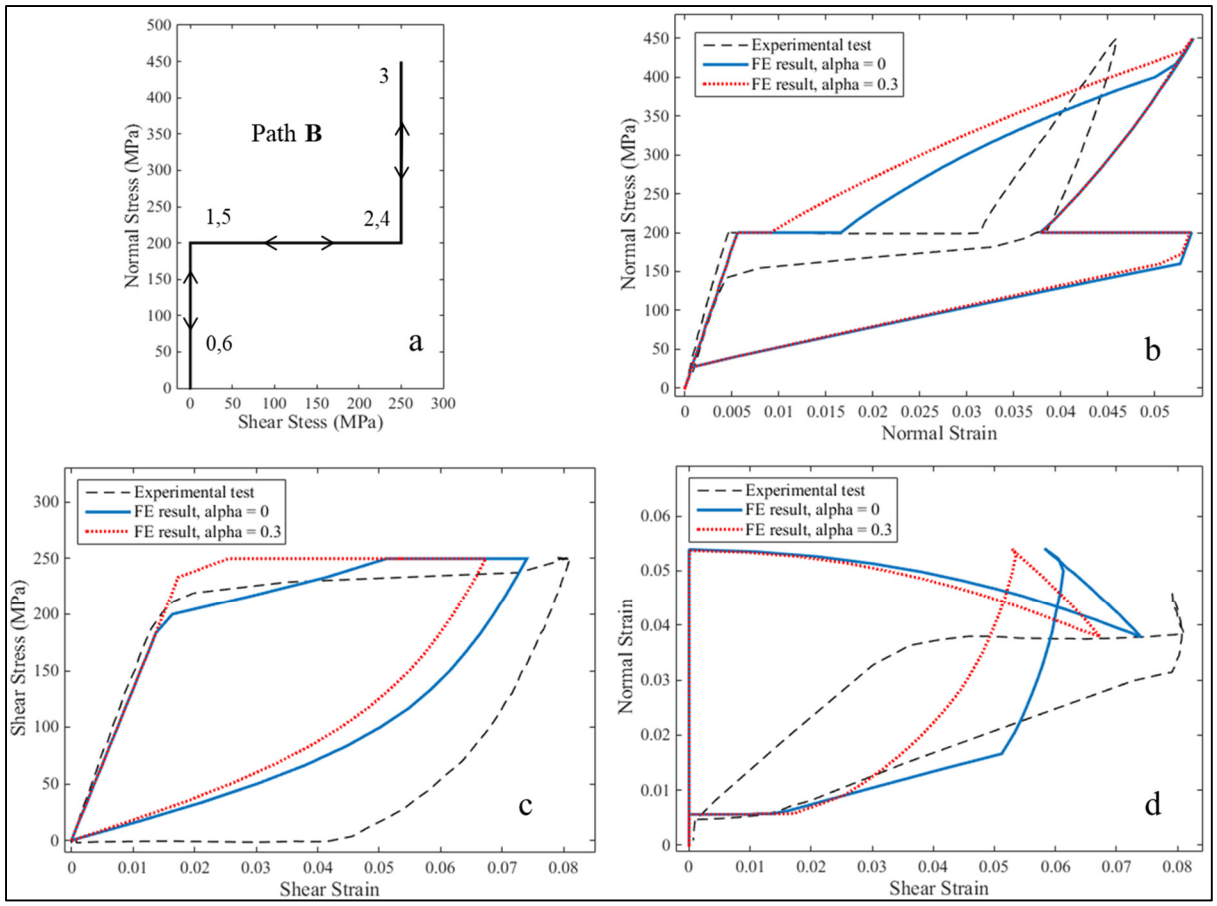

Figure 3.13 FE results with α values of 0 and 0.3 compared with the experimental test under the multiaxial loading path B. (a) Loading path, (b) Normal stress-strain response, (c) Shear stress-strain response, (d) Normal vs. shear strain response

From the comparisons made throughout this section, it is evident that Auricchio's SMA material model does not provide sufficient accuracy in reproducing the experimental test results under complex multiaxial loads with different loading paths.

An important observation was made regarding the uniaxial response of the material model: while this model tends to overestimate the shear strain under a uniaxial shear loading, the opposite happens when the model is subjected to multiaxial loadings, and the shear strains are underestimated. This indicates that the model behaves differently based on the type of loading.

The tension-compression asymmetry parameter α, was shown to be an influential factor in the model's response, especially under uniaxial shear loading. This can be explained knowing that, theoretically, a pure shear loading results in an equal amount of tensile and compressive principal stresses and variation in α value affects the amount of transformation caused by the compressive stress components. In this study, α was treated as a calibration parameter, and the overestimation of the shear strain under uniaxial shear loading was significantly reduced by increasing the value of this parameter to 0.3, but this value seems unrealistically high. It should be noted that a positive α value led to further underestimation of shear strain under multiaxial loading which was not desirable and the overall prediction of the model did not improve. Although the tension-compression asymmetry of the NiTi samples were not evaluated in this work, previous studies such as (Orgéas and Favier 1998, Lexcellent, Boubakar et al. 2006) suggest that NiTi alloys exhibit asymmetric behavior corresponding to positive α values which is in line with the calibrated positive value achieved in this work.

The martensite transformation in this model is driven by an internal variable accounting for the volumetric fraction of single variant martensite in the material. The changes in this variable are affected by a measure of stress, current temperature and material parameters taken from the uniaxial test. This variable is responsible for the partial path-dependent behavior of the model, but there are other factors involved behind the path dependency of SMAs as well. A major factor is the fact that the material structure contains regions with different crystallographic orientations favoring various martensite habit planes. This means that the amount of transformation in each region varies depending on their orientation with respect to the stress state.

This in turn creates different macroscopic responses of the material if non-proportional multiaxial loads with different sequences are applied. However, this model does not take into account the crystallographic orientation within the material, and the transformation thresholds are defined as scaler values unaffected by the direction. Another factor contributing to the inaccuracy of the model, to a lesser degree, is the fact that only one value is assumed by the

model for elastic modulus, while this value is significantly different between austenite and martensite.

The literature contains some examples of material modeling for SMAs, taking into account this orientational sensitivity and regional variation. For instance, the model suggested by Likhachev (Likhachev 1995), and later adapted for 1D modeling by Terriault and Brailovski (Terriault and Brailovski 2011, Terriault and Brailovski 2013) , divides the material domain into multiple regions of different crystallographic orientations, where the stress direction affects their rate of transformation. The transformation strain is then evolved by an averaged value of martensitic volume fraction over the whole domain. In a similar work by Patoor et al., different transformation behaviors in local regions were considered based on the difference in martensite variants, which were associated with multiple internal variables. A homogenized global constitutive model was then devised (Patoor, Eberhardt et al. 1996). Another example is the paper by (Richards, Lebensohn et al. 2013) where the martensitic transformation mechanisms are investigated in mesoscale for a single crystal and expanded to polycrystal structures. Finally, in a recent work, different imaging techniques were used to investigate the microstructure of NiTi alloys, the grains and their subdivision into different bands during transformation (Hsu, Polatidis et al. 2018).

It can be beneficial to further investigate these models and implement them into commercial finite element software to obtain a better predictive capability for SMA devices on which multiaxial loadings are applied.

3.3 Concluding Remarks

The main goal in this chapter was to investigate the accuracy of the material model for SMAs, currently implemented in commercial software, in reproducing the material response under complex loading conditions. To this end, thin-walled NiTi tubes were tested and characterized under uniaxial, as well as multiaxial loadings with two different paths, and a variety of experimental data were produced. An FE model based on the sample geometry was created

and the built-in constitutive model in Ansys FE software was assigned to the model. Simulations were then performed by applying the same loadings as the real tests. The results from the FE simulations were compared with those of the experimental tests.

While the constitutive model was able to provide a good prediction of the uniaxial response of the SMA NiTi sample, it was not able to closely predict the mechanical response of the material under multiaxial loads, nor did it exhibit the level of path dependency observed in the tests.

As more diverse applications of SMAs, such as porous structures, are emerging, there is an increasing need for modeling of SMA materials in complex loading situations. Although a large number of constitutive models are proposed in the literature, their commercial use in FE software is yet to occur. This study signifies the great need for implementing a numerically efficient and more accurate model into commercial software, which could facilitate more widespread use of SMA modeling in the industry.

CHAPTER 4

AN ALTERNATIVE SMA MATERIAL MODEL

When a porous metal is loaded, the material experiences a 3D, multiaxial stress state. Furthermore, in applications such as porous implants, due to the irregular nature of the applied forces, the material undergoes different loading paths. As discussed in Chapter 3, the Auricchio's model implemented in major commercial FE software such as Ansys, lacks in accuracy when multiaxial, path dependent response of SMAs is concerned, which highlights the need for a material model with better predictive capability.

To address the third objective of this thesis, pointed out in the Introduction, in this chapter we investigate a material model proposed by Likhchev (Likhachev 1995) which has the potential to improve upon the current model in terms of predicting the complex behaviors of SMAs and providing a promising solution for modeling of the SMA features in a straightforward and efficient way. This model was implemented in Matlab in order to evaluate its performance under different loading conditions.

First, a brief description of Likhachev's model will be provided. Then the response of the model will be studied under two types of load cases, namely, uniaxial and multiaxial. As for the multiaxial load cases, comparison was made between Likhachev's model and Auricchio's model against the experimental results acquired in Chapter 3.

Since the FE codes require the material models to receive strain and update the stress tensor as the output, it is necessary to formulate material models in strain-driven form. Therefore, different methods regarding strain-driven adaptation of this model will be explored.

4.1 Methodology

4.1.1 Thermodynamics of SMAs

The process of MT is driven by the free energy difference between the parent (austenite) and martensite phases. The free energy of austenite and martensite vary with different slopes with respect to temperature which are plotted schematically in Figure 4.1. As can be seen from the diagram, the difference between these two energies at a certain temperature, i.e. $\Delta G^{A\rightarrow M}$ or $\Delta G^{M\rightarrow A}$, provides the driving force behind the transformation in both directions. T_0 represents the thermodynamic equilibrium temperature which is usually defined as:

$$T_0 = (M_s + M_f + A_s + A_f)/4 \tag{4.1}$$

where M_s, M_f, A_s and A_f are the SMA characteristic or transformation temperatures that mark the onsets of different transformation stages defined below:

M_s: Martensite start temperature,

M_f: Martensite finish temperature,

A_s: Austenite start temperature,

A_f: Austenite finish temperature.

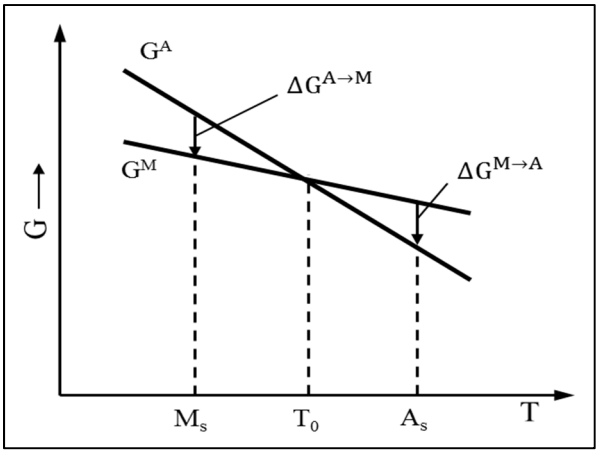

Figure 4.1 Free energy variation for austenite, G^A, and martensite, G^M, against temperature (Otsuka and Wayman 1999)

These four transformation temperatures have dependency on the applied stress which can be described by the Clausius-Clapeyron relation and coefficient β in Eq. (4.2) (Otsuka and Wayman 1999, Picornell, Pons et al. 2004):

$$\beta = \frac{d\sigma}{dT} = \frac{-\Delta H}{T_0 \varepsilon^{tr}} = \frac{-\Delta S}{\varepsilon^{tr}} \tag{4.2}$$

where σ is the stress, T is the temperature, ΔH is the enthalpy of transformation, ε^{tr} is the transformation strain, and ΔS is the entropy of transformation. Figure 4.2 shows a schematic phase diagram of an SMA where the slope β is indicated. From this diagram it is obvious that the transformation temperatures for an SMA are defined under a stress-free condition (σ=0), and as the stress is increased, these characteristic temperatures increase as well.

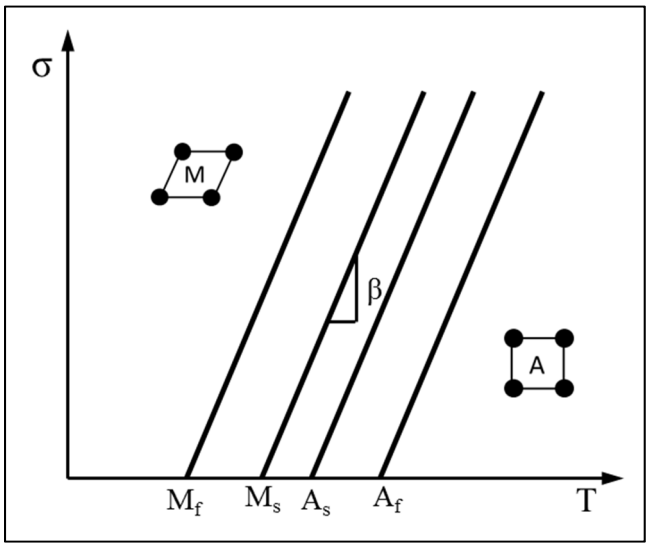

Figure 4.2 Schematic phase diagram of an SMA, showing the Clausius-Clapeyron coefficient β (Terriault and Brailovski 2011)

4.1.2 Likhachev's Model

A brief description of the model in 3D based on the adaptation by (Terriault and Brailovski 2013) is provided here. The original model is stress-driven and takes two control variables as thermomechanical load, namely, stress tensor σ_{ij} and temperature T, and the output is strain

tensor ε_{ij} which is additively decomposed to the elastic strain ε_{ij}^{el} and transformation strain ε_{ij}^{tr} shown in Eq. (4.3).

$$\varepsilon_{ij} = \varepsilon_{ij}^{el} + \varepsilon_{ij}^{tr} \qquad (4.3)$$
$$i = 1 \dots 3;\ j = 1 \dots 3$$

At any given state, the material is assumed to be a mixture of austenite and martensite phases, each having volume fractions of Φ_A and Φ_M, respectively. These volume fraction values range between 0 and 1, while satisfying the following condition as well:

$$\Phi_A + \Phi_M = 1 \qquad (4.4)$$

The elastic strain ε_{ij}^{el} can be calculated using the classical continuum mechanics and mixing rule in which the austenite and martensite contribute to the total elastic strain of the material proportional to their respective fractions:

$$\varepsilon_{ij}^{el} = \frac{\Phi_A}{E_A}\left[(1+\nu_A)\sigma_{ij} - \nu_A\sigma_{kk}\delta_{ij}\right] + \frac{\Phi_M}{E_M}\left[(1+\nu_M)\sigma_{ij} - \nu_M\sigma_{kk}\delta_{ij}\right] \qquad (4.5)$$
$$i,j,k = 1 \dots 3$$

where E_A, E_M, ν_A, ν_M, Φ_A and Φ_M are the Young's modulus, Poisson's ratio and volume fractions, with subscripts A and M denoting austenite and martensite, respectively, and δ_{ij} is the Kronecker tensor. To calculate the transformation tensor ε_{ij}^{tr}, the material is divided to N regions, each of which has their own crystallographic orientation in 3D, defined by an orientation tensor α_{ij}.

The orientations that are assigned to the regions are assumed to be uniformly distributed and are generated using the Euler angles γ, θ and ψ representing roll, pitch and yaw rotations of the

coordinate system around X, Y and Z axes. Each of these rotations are applied through rotation matrixes R_x, R_y, and R_z.

In order to create a uniform distribution of orientations, the three Euler angles and their range are defined as follows:

$$\begin{cases} \gamma = 2\pi x\,, & x \in [0,1] \\ \theta = \arcsin(y)\,, & y \in [0,1] \\ \psi = \pi(2z-1), & z \in [0,1] \end{cases} \tag{4.6}$$

where x, y and z can be randomly generated numbers between 0 and 1 to create the three angles. Alternatively, the numbers can be directly determined, equally spaced within the range. Having determined the three Euler angles the orientation tensor can be defined as:

$$\alpha_{ij} = R_x R_y R_z = \begin{bmatrix} \alpha_{11} & \alpha_{12} & \alpha_{13} \\ \alpha_{21} & \alpha_{22} & \alpha_{23} \\ \alpha_{31} & \alpha_{32} & \alpha_{33} \end{bmatrix} \tag{4.7}$$

where the components of α_{ij} are:

$$\begin{aligned} \alpha_{11} &= \cos\psi\cos\gamma - \cos\theta\sin\gamma\sin\psi \\ \alpha_{12} &= \cos\psi\sin\gamma + \cos\theta\cos\gamma\sin\psi \\ \alpha_{13} &= \sin\psi\sin\theta \\ \alpha_{21} &= -\sin\psi\cos\gamma - \cos\theta\sin\gamma\cos\psi \\ \alpha_{22} &= -\sin\psi\sin\gamma + \cos\theta\cos\gamma\cos\psi \\ \alpha_{23} &= \cos\psi\sin\theta \\ \alpha_{31} &= \sin\theta\sin\gamma \\ \alpha_{32} &= -\sin\theta\cos\gamma \\ \alpha_{33} &= \cos\theta \end{aligned} \tag{4.8}$$

Then the total transformation strain is achieved by averaging the contributions of all regions:

$$\varepsilon_{ij}^{tr} = \frac{1}{N}\sum_{n=1}^{N} \alpha_{pi}^{n}\, \alpha_{qj}^{n}\, d_{pq}\, \varphi^{n} \tag{4.9}$$

where d_{pq} is the distortion tensor which is a crystallographic characteristic of the martensite single crystal, and φ^n is the volume fraction of martensite in nth region. Therefore, the total volume fraction of martensite Φ_M will be the averaged value over all regions:

$$\Phi_M = \frac{1}{N}\sum_{n=1}^{N} \varphi^{n} \tag{4.10}$$

The martensite volume fraction in each region φ^n is the key variable that should be determined, and is calculated using the phase transformation kinetic rule, which defines a relation between the martensite volume fraction and the effective temperature T*. The effective temperature is a key concept of the Likhachev's model and is based upon the Clausius-Clapeyron relation. T* is defined as a function of the temperature, state of the stress, orientation of the region and the distortion tensor, and is obtained through the following equation:

$$T^{*} = T - \frac{T_0}{q_0}\, \alpha_{pi}\, \alpha_{qj}\, d_{pq}\, \sigma_{ij} \tag{4.11}$$

where q_0 is the heat exchange per unit volume during phase transformation, and T_0 is the thermodynamic equilibrium temperature defined in the Eq. (4.1). The transformation kinetic rule is shown in Figure 4.3. Having the effective temperature T* in each region and the previous value of φ^n, a unique updated value for φ^n can be found. It should be noted that φ_{max} can be assigned values more than 1 to account for the fact that in each region the phase transformation can occur in more than one direction with multiple martensite variants at the same time such that a region with more favorable orientation can expand beyond its original region volume and take up some space from less favorable regions. Also, φ_{min} can be assigned values greater than zero in order to account for the irreversible residual martensite transformation.

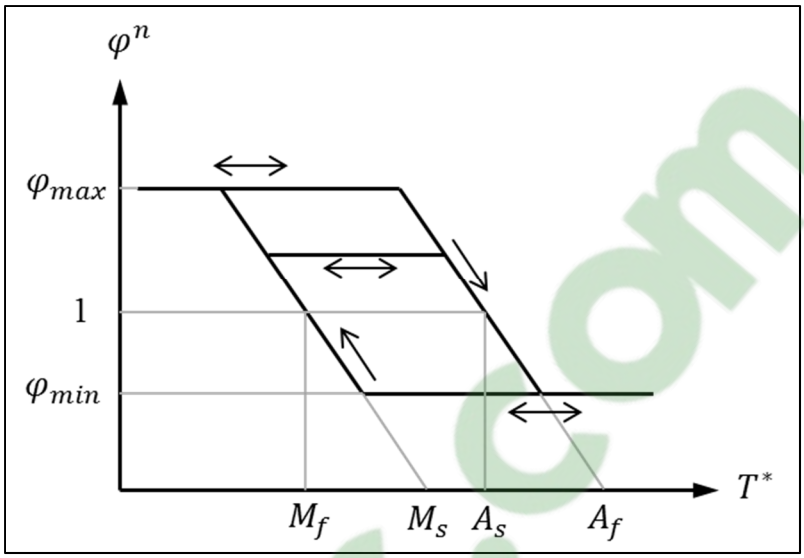

Figure 4.3 Kinetic rule for determining the martensite volume fraction of each region based on the effective temperature (Terriault and Brailovski 2013)

4.1.3 Uniaxial Loading

The Likhachev constitutive model in stress-driven form was implemented in Matlab. To obtain an initial evaluation of the model response, three uniaxial load cases were applied. The goal is to demonstrate the general superelastic response of the model, as well as its capability of generating the internal hysteresis loops. The uniaxial load cases are:

- Tensile loading with two inner loops
- Tensile and compressive loading with a single inner loop each
- Positive and negative shear loading, each with one inner loop

For these analyses, material parameters from (Terriault and Brailovski 2013) were used which are listed in Table 4.1. The distortion tensor included here is comprised of a single shear component of 0.1, which implies that the model should exhibit symmetrical tension-compression response.

Table 4.1 Material parameters used for the uniaxial analyses, taken from (Terriault and Brailovski 2013)

Material parameter	Symbol	Value	Units
Martensite start temperature	M_s	310	K
Martensite finish temperature	M_f	300	K
Austenite start temperature	A_s	320	K
Austenite finish temperature	A_f	330	K
Transformation heat per unit volume	q_0	150e6	J/m^3
Minimum volume fraction of martensite	φ_{min}	0	-
Maximum volume fraction of martensite	φ_{max}	10	-
Young's modulus of austenite	E_A	70e9	Pa
Young's modulus of martensite	E_M	50e9	Pa
Poisson's ratio of austenite	ν_A	0.33	-
Poisson's ratio of martensite	ν_M	0.33	-
Number of regions in the domain	N	1000	-
Distortion tensor	d	$\begin{bmatrix} 0 & 0.1 & 0 \\ 0.1 & 0 & 0 \\ 0 & 0 & 0 \end{bmatrix}$	-

The loadings were applied in a sequence of several time steps, and each time step was divided into 20 sub-steps to create enough data points. The applied stress history against the sub-steps are shown in Figure 4.4.

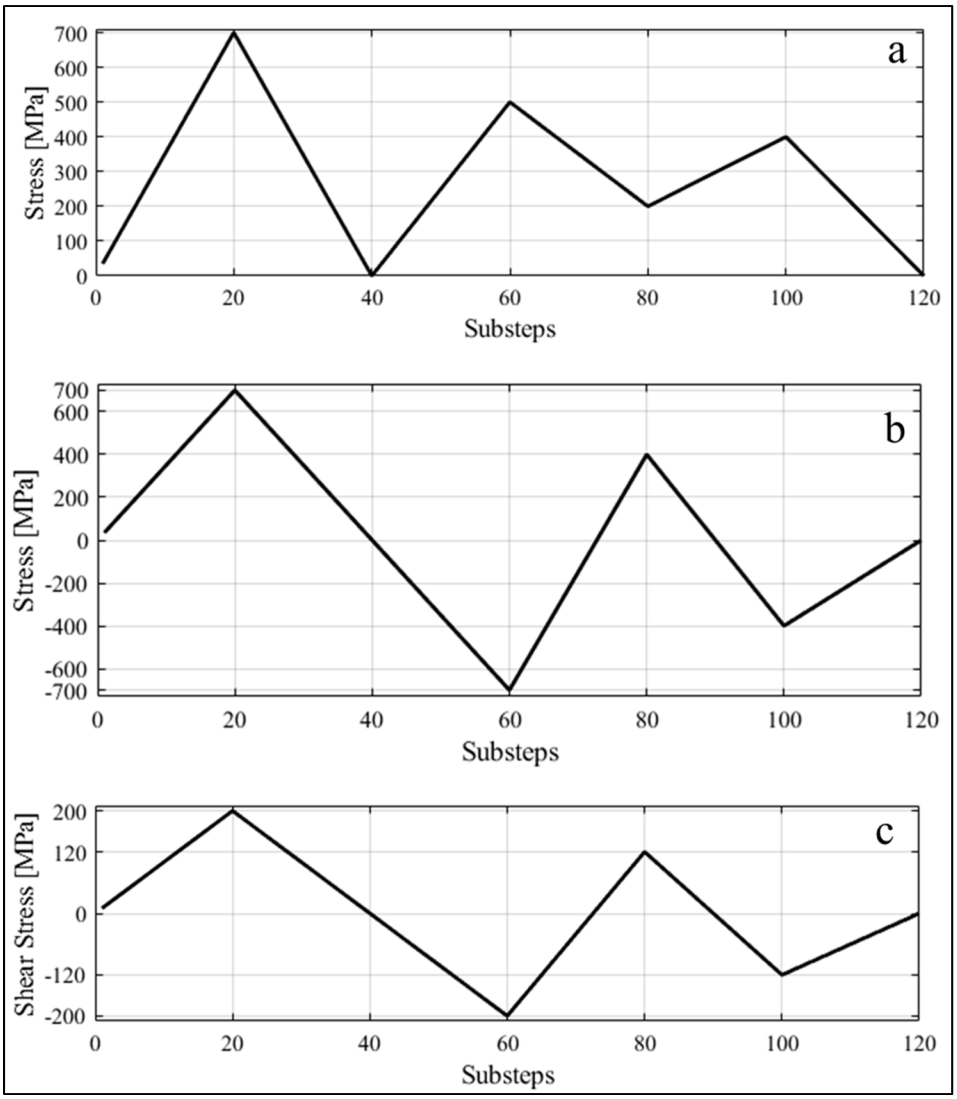

Figure 4.4 Uniaxial Loading sequences; (a): tensile loading with two inner loops (b): tensile and compressive loading with one inner loop each (c): positive and negative shear loading with one inner loop each

4.1.4 Multiaxial Loading

The multiaxial simulations were performed in order to compare the path-dependent response of the Likhachev's model with that of Ansys and the experimental test results under two multiaxial loading paths A and B described in the previous chapter; see Figure 3.3. The material parameters used in these analyses are based on the values obtained from the experimental tests. The Likhachev's model requires four transformation temperatures M_f, M_s,

A_s and A_f. Given the four transformation stresses from the experimental tests, a room temperature of T= 296 K (23 °C), and assuming a Clausius-Clapeyron coefficient of β= 5e6 Pa/K, the transformation temperatures can be estimated using the phase diagram depicted in Figure 4.2 as follows:

$$M_f = T - \frac{\sigma_{mf}}{\beta} \qquad (4.12)$$
$$M_s = T - \frac{\sigma_{ms}}{\beta}$$
$$A_s = T - \frac{\sigma_{as}}{\beta}$$
$$A_f = T - \frac{\sigma_{af}}{\beta}$$

A more realistic distortion tensor d was also used which was taken from the work by (Knowles and Smith 1981). The maximum martensite volume fraction φ_{max} was used as a tuning parameter to achieve the best curve fit to the experimental results. All the material parameters are listed in Table 4.2.

Table 4.2 Material parameters used for the multiaxial analyses

Material parameter	Symbol	Value	Units
Martensite start temperature	M_s	215.4	K
Martensite finish temperature	M_f	187.2	K
Austenite start temperature	A_s	262.2	K
Austenite finish temperature	A_f	290.4	K
Clausius-Clapeyron coefficient	β	5e6	Pa/K
Transformation heat per unit volume	q_0	57.3e6	J/m^3
Minimum volume fraction of martensite	φ_{min}	0	-
Maximum volume fraction of martensite	φ_{max}	2.4	-
Young's modulus of austenite	E_A	49e9	Pa
Young's modulus of martensite	E_M	23e9	Pa
Poisson's ratio of austenite	ν_A	0.33	-
Poisson's ratio of martensite	ν_M	0.33	-
Number of regions in the domain	N	1000	-
Distortion tensor	d	$\begin{bmatrix} -0.0337 & 0 & -0.0642 \\ 0 & 0.0763 & 0 \\ -0.0642 & 0 & -0.0418 \end{bmatrix}$	-

4.1.5 Strain-driven Formulations of Likhachev's Model

The calculation procedure within an FE program requires a material routine to receive the displacements and update the stress in return. Most constitutive models, however, are derived in stress-driven format, requiring additional calculations to adapt them to the FE framework. Many models in the literature make use of some form of iterative procedures, such as return-mapping technique. Here, we explore a non-iterative as well as an iterative formulation.

4.1.5.1 Non-iterative Formulation

A non-iterative strain-driven formulation of the Likhachev's model has the benefit of substantially decreasing the computational load, as the stress is calculated directly and there will be no iteration process and convergence criterion involved. Here, an attempt has been made to provide a non-iterative strain-driven adaptation of the Likhachev's model.

For this formulation, we consider the fact that in the original model, the regions are mathematically arranged in series system where the stress in each region is equal to the global stress, while each region's strain is determined individually, and contribute to the global strain. By turning to a strain-driven framework, we adopt a parallel arrangement of the regions, where the applied strain would be equal for all regions. It should be noted that within each region we still have the additive decomposition of strain to the elastic and transformation parts mentioned before in Eq. (4.3). Figure 4.5 shows these two arrangement types for N regions in the domain.

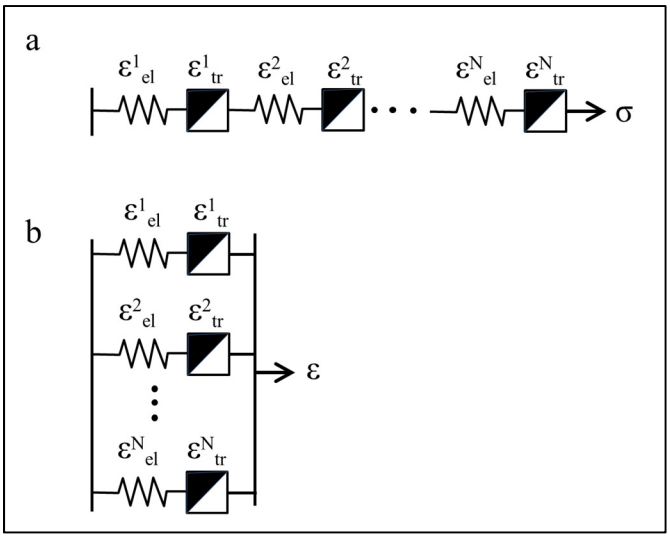

Figure 4.5 Schematic arrangement of N regions:
(a) Series (b) Parallel

In order to calculated the volume fraction of martensite φ^n in the nth region, the original model relied on determining the effective temperature T* which takes into account the Clausius-Clapeyron coefficient which is a measure of slope dσ/dT. Here, a similar concept is suggested in which a slope dε/dT will be established to formulate a modified effective temperature T_m^*. As a first step, the transformation stresses at a given temperature T in a uniaxial condition can be calculated by rearranging the relations in the Eq. (4.12) as follows:

$$\begin{aligned} \sigma_{mf} &= \left(T - M_f\right) \cdot \beta \\ \sigma_{ms} &= \left(T - M_s\right) \cdot \beta \\ \sigma_{as} &= \left(T - A_s\right) \cdot \beta \\ \sigma_{af} &= \left(T - A_f\right) \cdot \beta \end{aligned} \tag{4.13}$$

Having the Young's modulus for austenite and martensite, E_A and E_M, and the maximum tensile transformation strain, ε_{max}, and considering the schematic stress-strain curve depicted in Figure 4.6, the corresponding transformation strains can be calculated through the following equations:

$$\varepsilon_{Mf} = \varepsilon_{max} + \frac{\sigma_{Mf}}{E_M} \tag{4.14}$$

$$\varepsilon_{Ms} = \frac{\sigma_{Ms}}{E_A}$$

$$\varepsilon_{As} = \varepsilon_{max} + \frac{\sigma_{As}}{E_M}$$

$$\varepsilon_{Af} = \frac{\sigma_{Af}}{E_A}$$

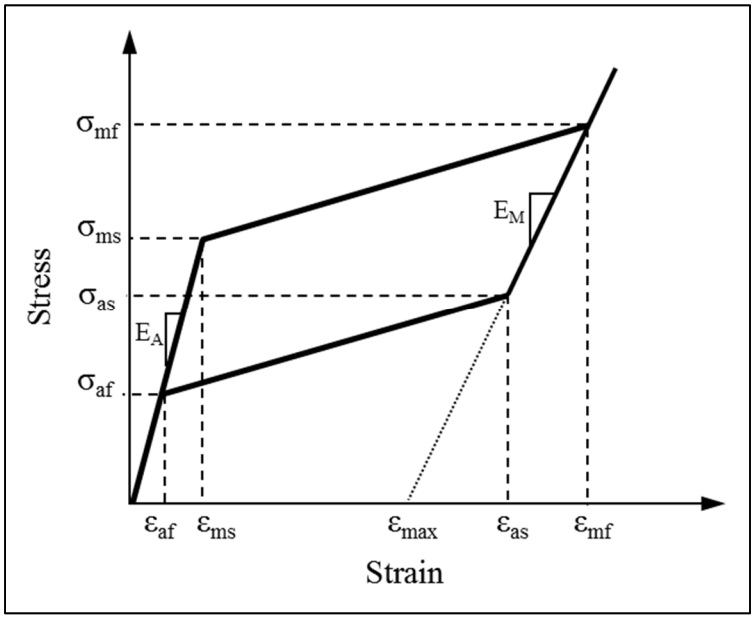

Figure 4.6 Schematic stress-strain curve of an SMA with transformation stresses and strains

At any two arbitrary temperatures above A_f, T_1 and T_2, one can plot the complete hysteresis cycle as shown in Figure 4.7.

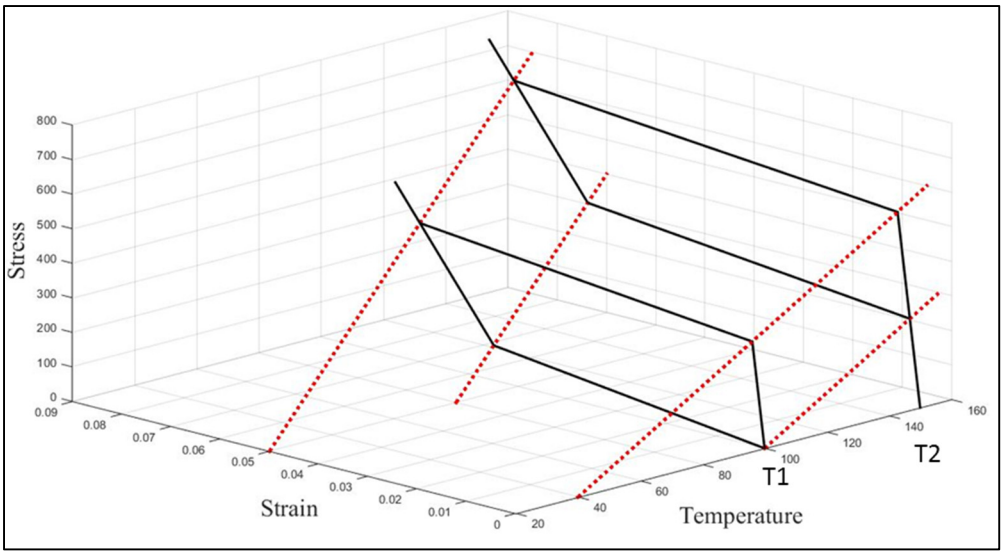

Figure 4.7 Two isothermal superelastic cycles at temperatures T1 and T2

For each of the curves an average of the transformation strains can be obtained as:

$$\varepsilon_0 = (\varepsilon_{mf} + \varepsilon_{ms} + \varepsilon_{as} + \varepsilon_{af})/4 \tag{4.15}$$

Which can loosely related to the thermodynamic equilibrium temperature T_0. Given this average strain at T_1 and T_2, namely, $\varepsilon_{0,1}$ and $\varepsilon_{0,2}$, a slope can be defined:

$$\rho = \frac{\varepsilon_{0,2} - \varepsilon_{0,1}}{T_2 - T_1} \tag{4.16}$$

Figure 4.8 shows the strain-temperature view of the plot in Figure 4.7 where the slope definition is depicted between two temperatures.

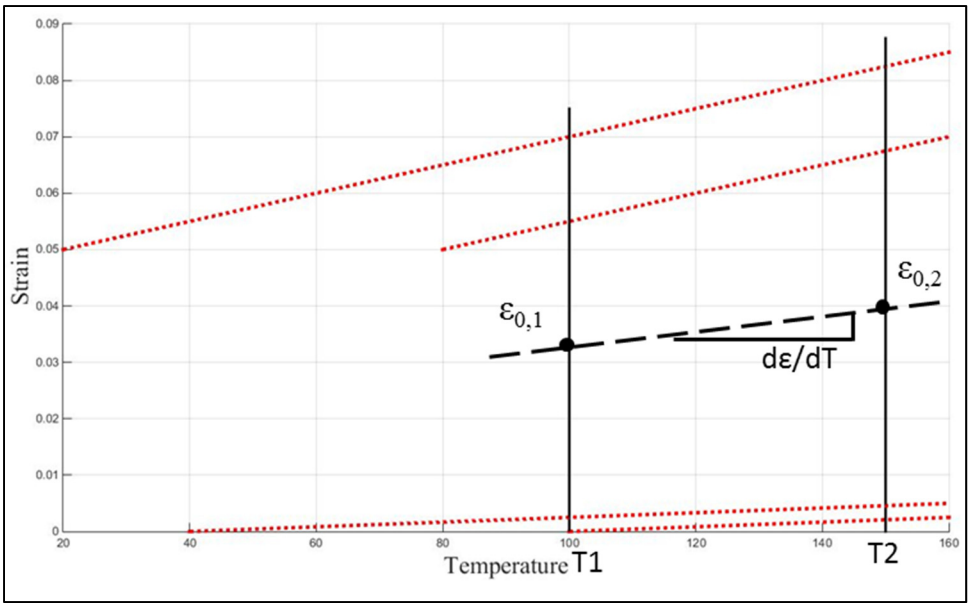

Figure 4.8 Definition of the slope ρ

Having defined the coefficient ρ, the modified effective temperature is defined as:

$$T_m^* = T - \frac{c}{\rho}\alpha_{pi}\alpha_{qj}d_{pq}\varepsilon_{ij} \tag{4.17}$$

where c is a tuning parameter used for curve fitting in the simulations. Using the Eq. (4.17), each region in the domain is assigned with an effective temperature. Consequently, the same transformation kinetic rule can be used to determine the volumetric fraction of martensite, φ^n.

An averaging over all the regions will give the total volumetric martensite fraction Φ_M using Eq. (4.10). Then the components of the transformation strain tensor ε_{ij}^{tr} are calculated using Eq. (4.9). Consequently, based on the additive decomposition of strains, the elastic strain is obtained:

$$\varepsilon_{ij}^{el} = \varepsilon_{ij} - \varepsilon_{ij}^{tr} \tag{4.18}$$

Similar to the Eq. (4.5), the expressions for compliance matrices of austenite and martensite, C_A and C_M, respectively are defined as follows:

$$C_A = \frac{1}{E_A}\begin{bmatrix} 1 & -\nu_A & -\nu_A & 0 & 0 & 0 \\ -\nu_A & 1 & -\nu_A & 0 & 0 & 0 \\ -\nu_A & -\nu_A & 1 & 0 & 0 & 0 \\ 0 & 0 & 0 & 2(1+\nu_A) & 0 & 0 \\ 0 & 0 & 0 & 0 & 2(1+\nu_A) & 0 \\ 0 & 0 & 0 & 0 & 0 & 2(1+\nu_A) \end{bmatrix} \tag{4.19}$$

$$C_M = \frac{1}{E_M}\begin{bmatrix} 1 & -\nu_M & -\nu_M & 0 & 0 & 0 \\ -\nu_M & 1 & -\nu_M & 0 & 0 & 0 \\ -\nu_M & -\nu_M & 1 & 0 & 0 & 0 \\ 0 & 0 & 0 & 2(1+\nu_M) & 0 & 0 \\ 0 & 0 & 0 & 0 & 2(1+\nu_M) & 0 \\ 0 & 0 & 0 & 0 & 0 & 2(1+\nu_M) \end{bmatrix}$$

The Voigt vector format of the elastic strain is

$$\varepsilon_v^{el} = \begin{bmatrix} \varepsilon_{11} \\ \varepsilon_{22} \\ \varepsilon_{33} \\ 2\varepsilon_{23} \\ 2\varepsilon_{13} \\ 2\varepsilon_{12} \end{bmatrix} \tag{4.20}$$

Finally the stress in vector form is calculated through the following equation:

$$\sigma_v = [\Phi_A C_A + \Phi_M C_M]^{-1}\, \varepsilon_v^{el} \tag{4.21}$$

4.1.5.2 Evaluation of Non-iterative Strain-driven Model

In order to assess its performance, this model was implemented in Matalab and a tensile-compressive load case was used to investigate the response of this strain-driven model. To this end, a comparison should be made between the stress output of the strain-driven model and the

stress input of the stress-driven model. First the tensile-compressive analysis with the stress-controlled model was performed with the applied stress history shown in Figure 4.9. Then the output strain tensor components were used as an input for the strain-driven model. The orientation matrices of the regions were assigned uniformly so that a comparison could be made on equal grounds between the two models. The material parameters from Table 4.1 was used, and the parameter c was adjusted a value of 5.3 in order to best match the curve from the stress-driven analysis. Ideally, the strain-driven model should be able to generate stresses as close to the applied stress as possible.

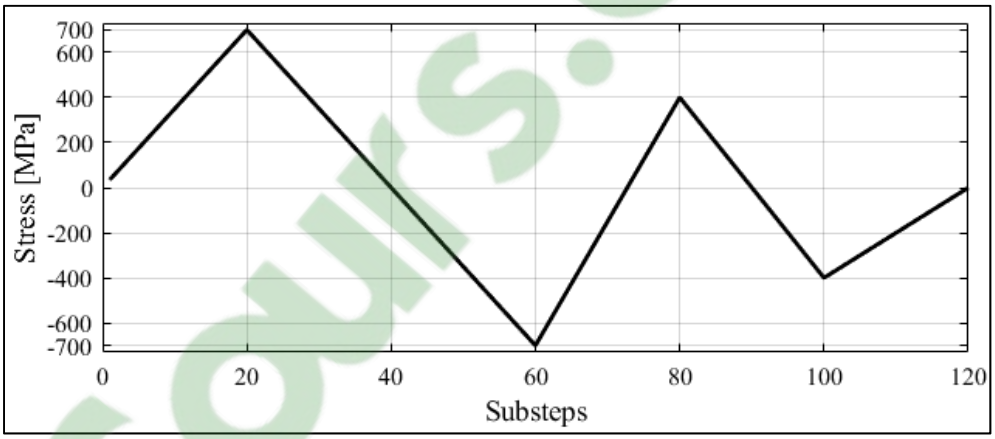

Figure 4.9 Stress history applied to the original Likhachev model

4.1.5.3 Iterative Formulation

Although iterative formulations are more computationally demanding, they can offer more robust performance and accurate response as they require achieving convergence within a determined tolerance in each time step, so the error is kept below a certain level throughout the whole analysis. A common iterative formulations is the return mapping technique, where for a given strain at time t_{n+1}, ε^{n+1}, corresponding stress and state variables at time t_{n+1} are approximated based on their values at time t_n. Usually, the iteration starts with calculating a trial stress, assuming fully elastic response, and then the strain is corrected iteratively to account for inelastic component of the strain.

Here, an iterative strain-driven formulation with slightly different approach is proposed which uses the concept of control feedback loop. The updated strain tensor ε_{ij}^{n+1} is considered as the set input value. The algorithm starts with a trial stress tensor σ^{trial}, which can be assumed to be the stress tensor at time t_n, in other words, $\sigma^{trial} = \sigma^n$. Based on the trial stress and the state variables, a trial strain tensor ε^{trial} is calculated. Consequently, and error tensor can be calculated as

$$\Delta_{ij} = \varepsilon_{ij}^{n+1} - \varepsilon_{ij}^{trial} \tag{4.22}$$

A numerical proportional-integral-differential (PID) control function is applied to the trial stress tensor in order to reduce the error to a value below a desired tolerance. In each iteration (k), the trial stress tensor is corrected as follows

$$\begin{aligned} \sigma_{ij}^{trial}|_k &= \sigma_{ij}^{trial}|_{k-1} + P + I + D \,, \\ P &= C_P \Delta_{ij}(t) \\ I &= C_I \int_0^t \Delta_{ij}(t) dt \\ D &= C_D \frac{d\Delta_{ij}(t)}{dt} \end{aligned} \tag{4.23}$$

where P, I and D are proportional, integral and derivative transfer functions, respectively, and C_P, C_I, and C_D are the corresponding coefficients for tuning whose values are chosen as a fraction of the austenite Young's modulus E_A. Figure 4.10 shows the block diagram of a PID control system in the time domain.

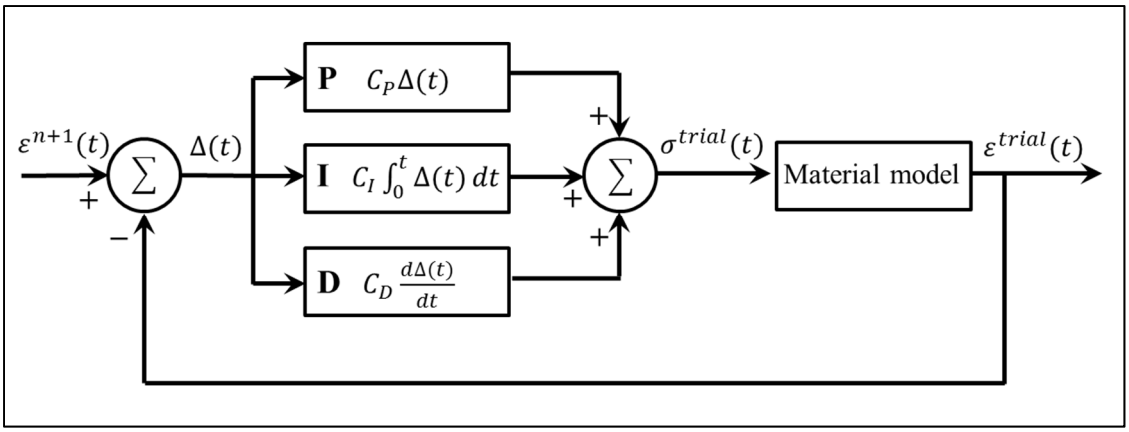

Figure 4.10 Schematic block diagram of PID control applied to the Likhachev model

As the progress of the control process is tracked by the iteration number k, discrete form of the time integral and derivative functions can numerically be estimated through Eq. (4.24).

$$I_{ij}^{k} = C_I \int_0^{k*Ts} \Delta_{ij}(t)dt \approx C_I \left[I_{ij}^{k-1} + \frac{\Delta_{ij}^{k} + \Delta_{ij}^{k-1}}{2} * Ts \right] \qquad (4.24)$$

$$D_{ij}^{k} = C_D \frac{d\Delta_{ij}(t)}{dt} \approx C_D \frac{\Delta_{ij}^{k} - \Delta_{ij}^{k-1}}{Ts}$$

where Ts is the time step which here is assigned a value of one. The iteration stops when a scalar measure of the error falls below the tolerance. This scalar measure is defined as the sum of the absolute value of the error tensor components. The tolerance was chosen as a fraction of the sum of d-tensor absolute component values:

$$\bar{d} = \sum_{j=1}^{3} \sum_{i=1}^{3} |d_{ij}| \qquad (4.25)$$

4.1.5.4 Evaluation of the Iterative Strain-driven Model

The Matlab implementation of the iterative strain-driven algorithm was evaluated under both uniaxial and multiaxial load cases. As for the uniaxial load case, the stress history shown in

Figure 4.9 was used, and for the multiaxial one, the loading paths A and B shown in Figure 3.3 were applied. The material parameters in Table 4.2 were used, and the coefficient C_P, C_I and C_D, as well as the tolerance were tuned in order to achieve the highest computational speed and accuracy. The values for the coefficients and the tolerance are listed in Table 4.3.

Table 4.3 Coefficients and tolerance value used for the iterative strain-driven model

Coefficient	Value
C_P	0.01 * E_A
C_I	0.0005 * E_A
C_D	0.0003 * E_A
Tolerance	0.0001 * $\bar{d}$

4.1.6 Calculation of the Tangent Stiffness Matrix

In order to implement a non-linear material model in an FE program, it is usually necessary to calculate a tangent modulus of tangent stiffness matrix. Since the stiffness of a non-linear material varies with respect to the strain, the FE software needs a tangent stiffness matrix at each time increment to assemble the element stiffness matrix. The tangent stiffness matrix $\boldsymbol{C}$ is defined as the Jacobian of stress with respect to strain. This matrix is usually derived analytically for material models that are based on strain energy functions, but that is not the case with Likhachev's model. Here a numerical method described by (Meier, Schwarz et al. 2014) is used where strain perturbations are used to estimate the tangent stiffness. This matrix is defined as:

$$\boldsymbol{C}_{ijkl} = \frac{d\sigma_{ij}}{d\varepsilon_{kl}} \approx \frac{\sigma_{ij}\left(\hat{\varepsilon}^{(kl)}\right) - \sigma_{ij}(\varepsilon)}{\Delta\varepsilon} \tag{4.26}$$

where $\Delta\varepsilon$ is a scalar value for the strain perturbation and $\hat{\varepsilon}^{(kl)}$ is the perturbed strain tensor with respect to the $(kl)^{th}$ component, calculated as:

$$\hat{\varepsilon}^{(kl)} = \varepsilon + \frac{\Delta\varepsilon}{2}\,(e_k \otimes e_l + e_l \otimes e_k) \tag{4.27}$$

Due to symmetry, only six strain perturbation components are needed in order to form the tangent modulus. By applying each strain perturbation, the material model will produce a stress response composed of six unique components, and then the $\boldsymbol{C}$ matrix with 36 components can be assembled.

4.1.7 Implementation of Likhachev's Model into Ansys

The iterative strain-driven formulation of the Likhachev's model, including the tangent stiffness calculation, was coded as a material subroutine for Ansys FE software with Fortran programming language. This implementation is done using one of Ansys' user-programmable features (UPF) which allows creating user-defined material models. After compiling, the developed code gets integrated into the Ansys software. Then the material model can be utilized in the analyses using APDL commands.

4.2 Results and Discussions

4.2.1 Uniaxial Response of Likhachev's Model

In order to demonstrate the superelastic response of the Likhachev's model in its original stress-driven form, this model was analyzed under three different uniaxial load cases shown in Figure 4.4. The results in form of stress-strain plots are shown in Figure 4.11 to Figure 4.13.

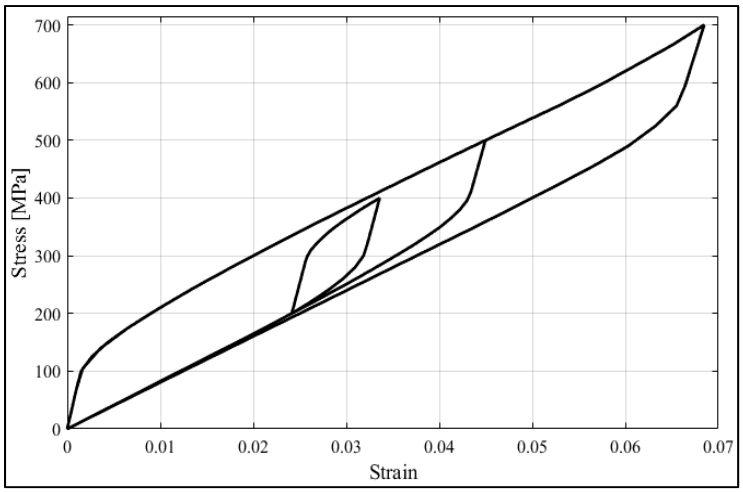

Figure 4.11 Superelastic response of the Likhachev's model under tensile loading with two inner loops

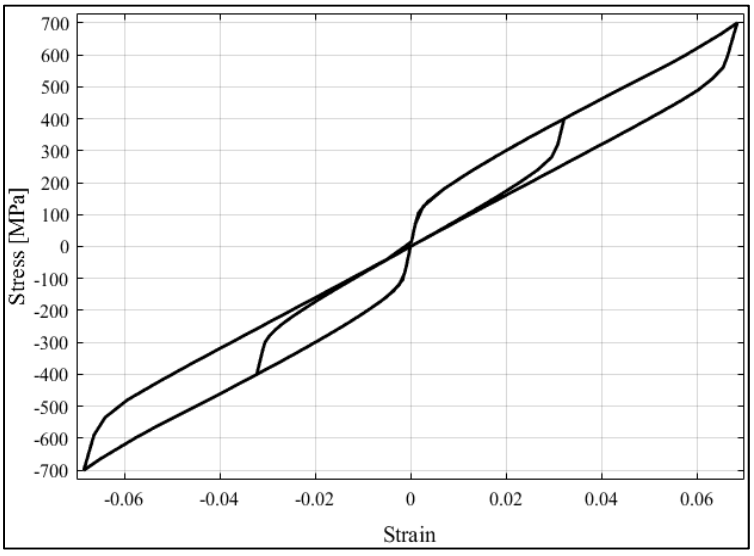

Figure 4.12 Superelastic response under tensile and compressive loading with an inner loop on each side

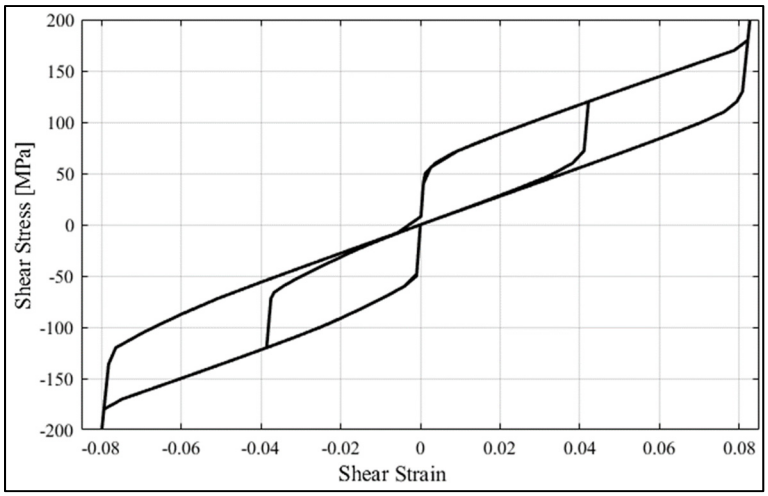

Figure 4.13 Superelastic response under positive
and negative shear loading with one inner loop each

AS can be seen from the stress-strain results, Likhachev's model is able to produce the full hysteresis cycle as well as the inner loops. Due to the assigned distortion tensor D, having a single shear component, the material response is symmetrical in both compression and tension. The same is true for the positive and negative shear stress.

4.2.2 Multiaxial Response of Likhachev's Model

The multiaxial path-dependent behavior of the Likhachev's model under two different loading paths are compared with that of the experimental results and Auricchio's model in Ansys. Figure 4.14 andFigure 4.15 show these comparisons for paths A and B, respectively.

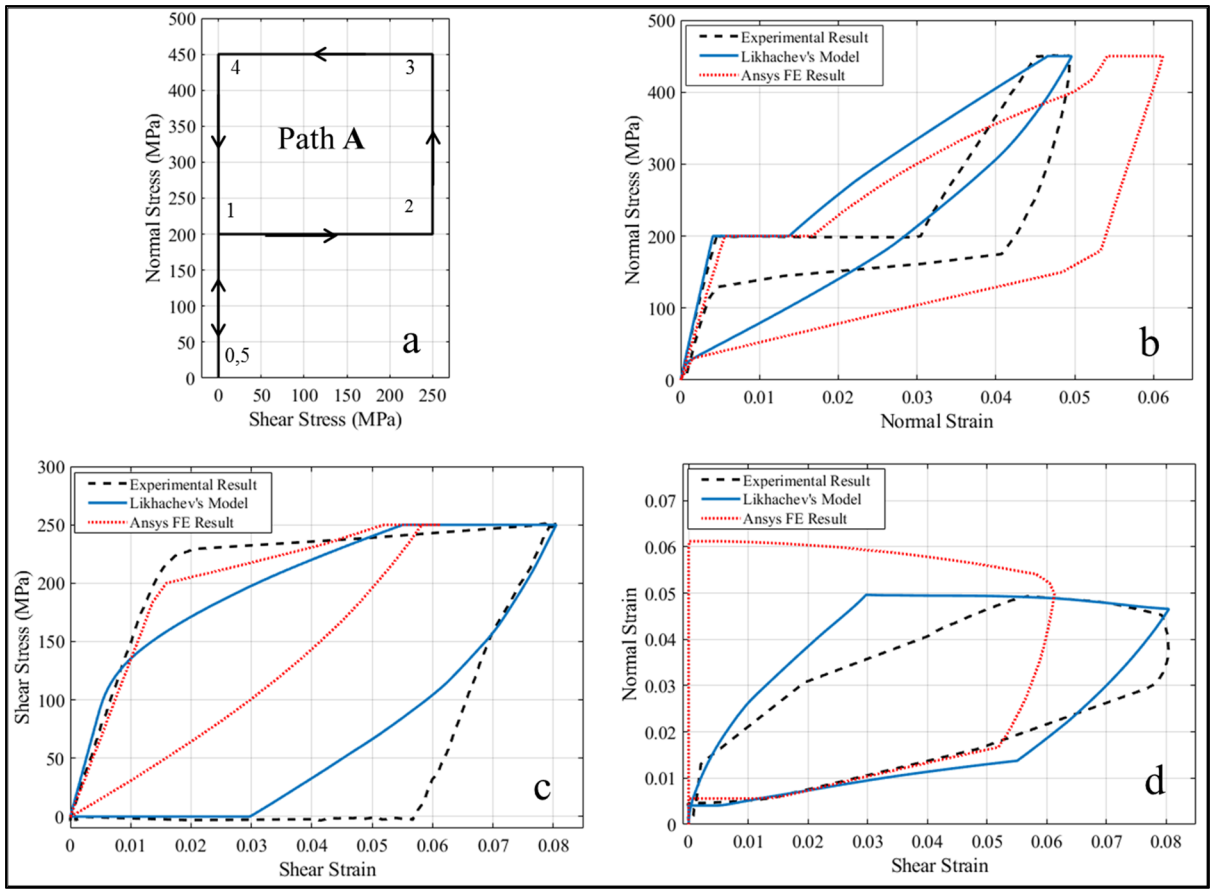

Figure 4.14 Likhachev's model response compared to Ansys FE results and experimental data under multiaxial load path A; (a) Loading path, (b) normal stress-strain response, (c) shear stress-strain response, (d) normal strain vs. shear strain response

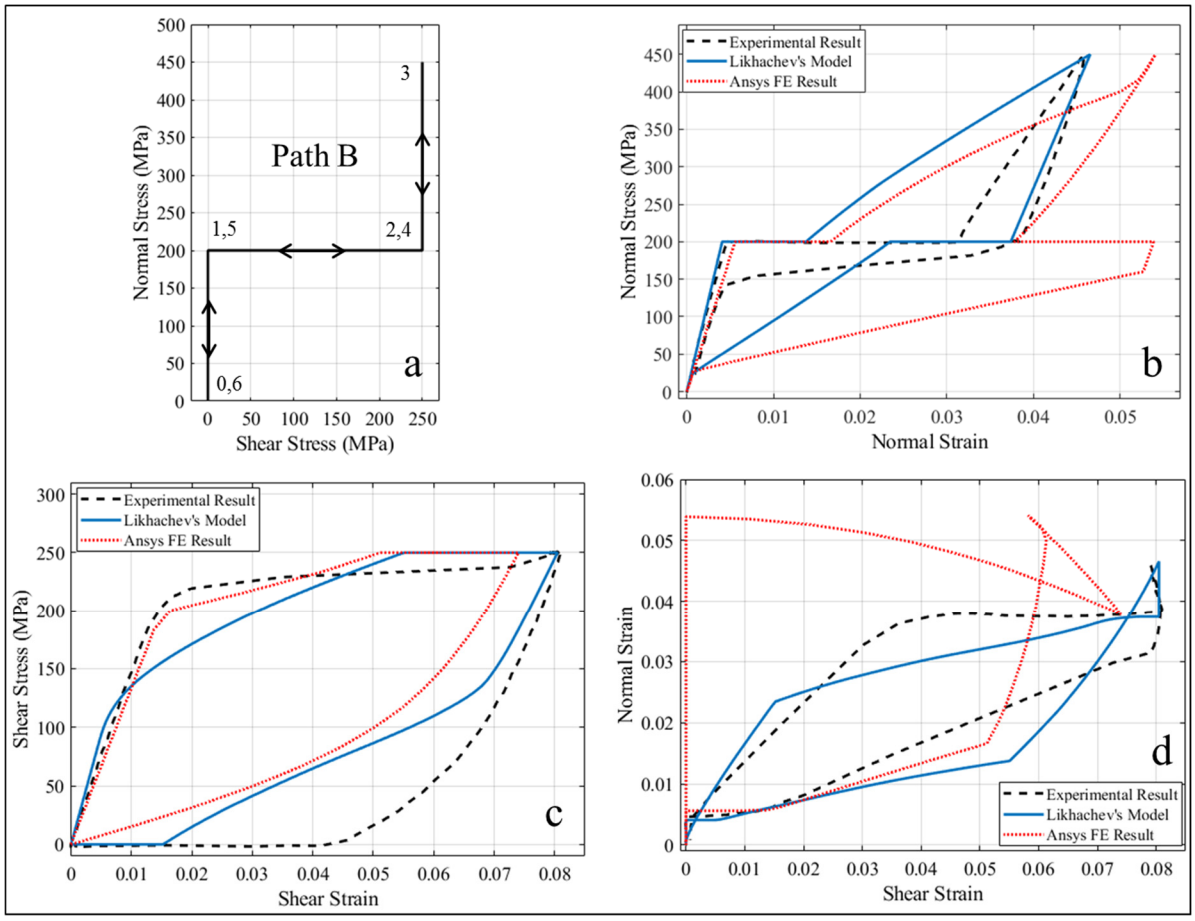

Figure 4.15 Likhachev's model response compared to Ansys FE results and experimental data under multiaxial load path B; (a) Loading path, (b) normal stress-strain response, (c) shear stress-strain response, (d) normal strain vs. shear strain response

As can be seen from the figures, the Likhachev's model offers an improvement over the Ansys FE results with Auricchio's material model, and can predict the path-dependent response of the NiTi samples in test results more closely. However, the agreement is still not perfect.

4.2.3 Analysis Results of Strain-driven Formulations

4.2.3.1 Non-iterative formulation

The non-iterative strain-driven formulation of the Likhachev's model was analyzed under a sequence of strain tensors obtained from the uniaxial tensile-compressive stress loading of the original stress-driven model (see Figure 4.9). The stress-strain plot of the analysis results of both original and strain-driven models are illustrated in Figure 4.16.

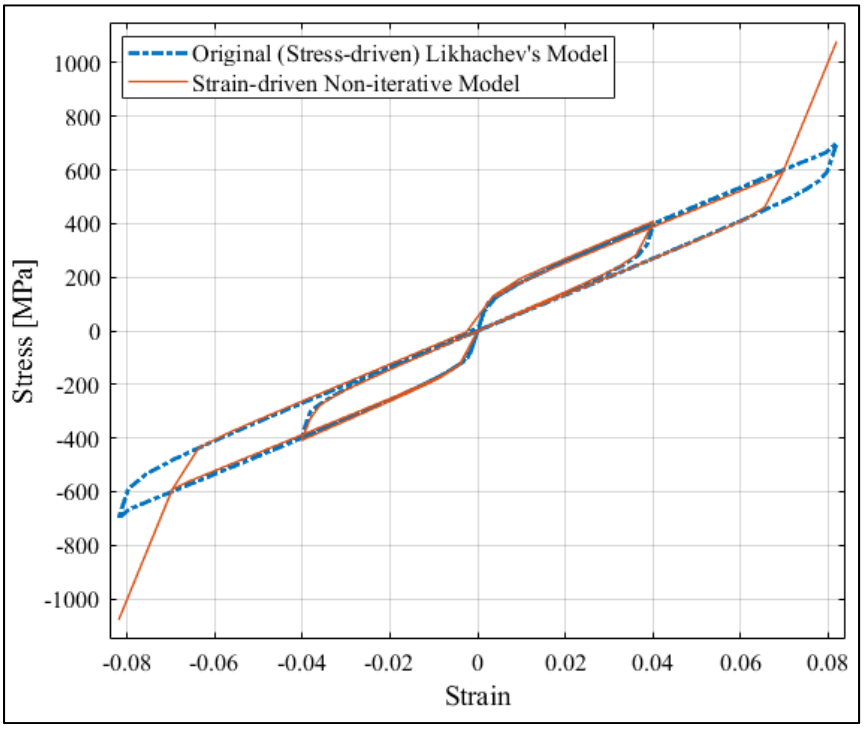

Figure 4.16 Superelastic response of the stress-driven Likhachev's model under uniaxial loading compared with the strain-driven non-iterative adaptation

In order to compare the stress output of the strain-driven model with the applied stress to the stress-driven model, the stress histories for both models are over imposed in Figure 4.17.

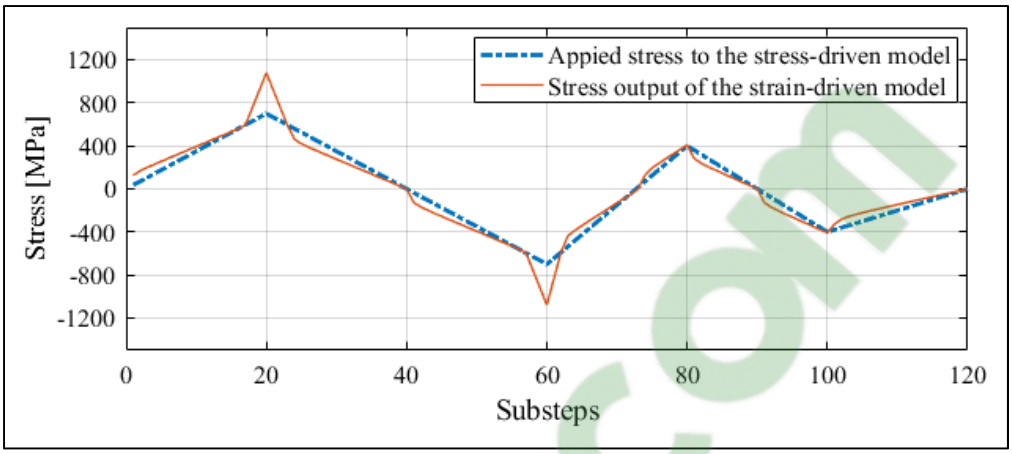

Figure 4.17 Comparison of stress history applied to the original Likhachev's model and the stress history obtained from the strain-driven adaptation

As can be seen from the analysis results, this non-iterative strain-driven adaptation of Likhachev's model is able to closely follow the response of the original model for the most part of the loading range, however, it starts to deviate at higher strain values where stresses are overestimated by the model, which implies that this model is best suited for limited range of strains.

4.2.3.2 Iterative Formulation

The iterative strain-driven model was analyzed under both uniaxial and multiaxial load cases. Figure 4.18 shows the uniaxial superelastic response of this model compared to the original one. Figure 4.19Figure 4.20 show this model's response under the multiaxial loading paths A and B, respectively.

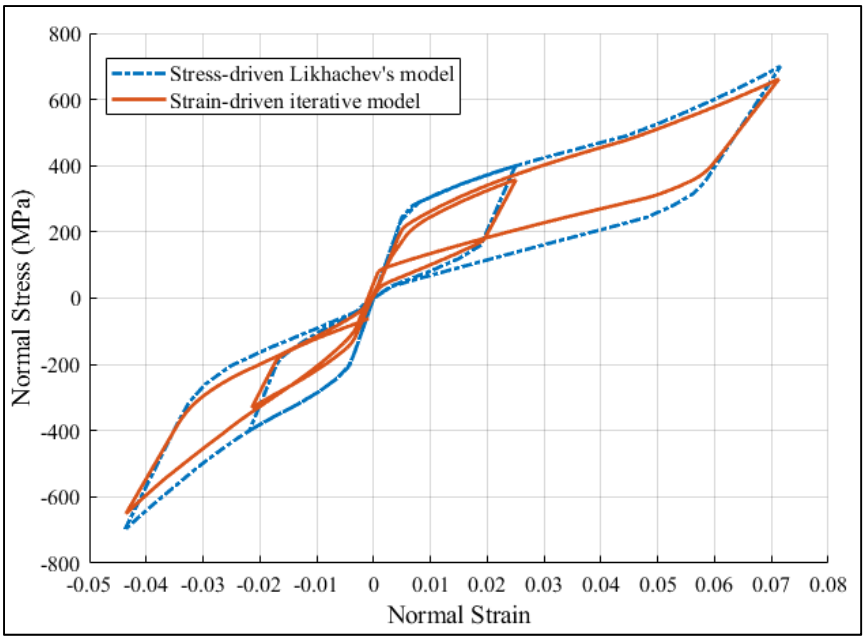

Figure 4.18 Superelastic response of the stress-driven Likhachev's model under uniaxial loading compared with the strain-driven iterative model

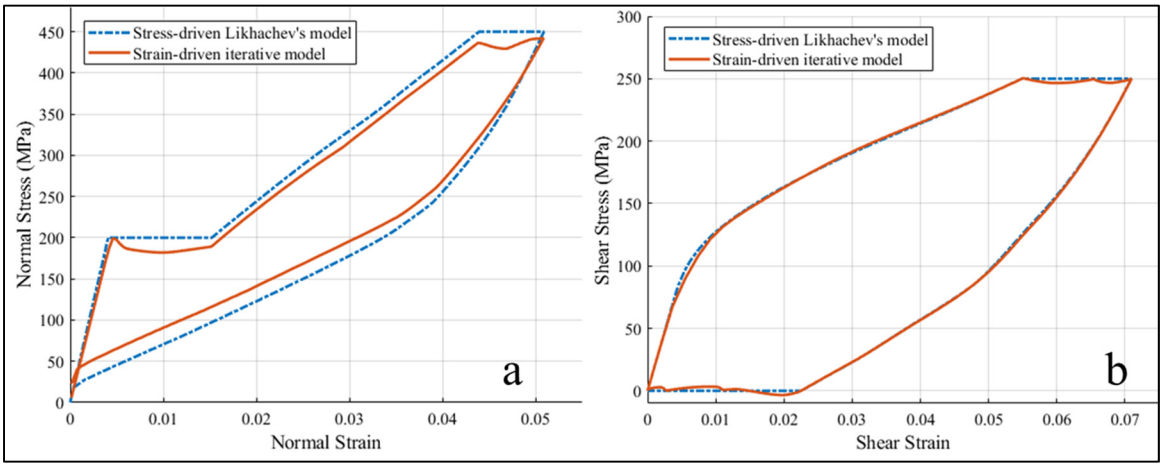

Figure 4.19 Superelastic response of the stress-driven Likhachev's model under multiaxial loading path A compared with the strain-driven iterative model; (a) normal (b) shear

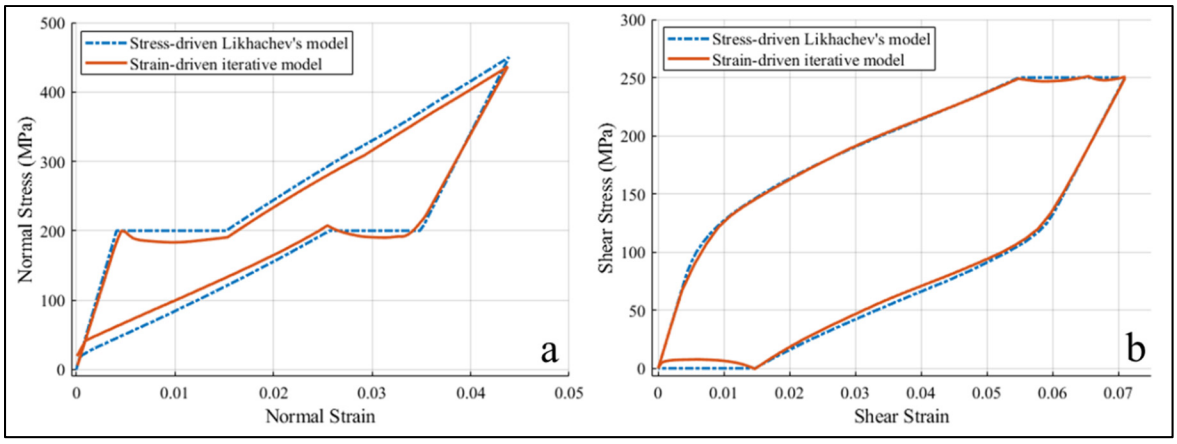

Figure 4.20 Superelastic response of the stress-driven Likhachev's model under multiaxial loading path B compared with the strain-driven iterative model; (a) normal (b) shear

As can be seen from these response plots, this strain-driven formulation of Likhachev's model is able to follow the response of the stress-driven model with good accuracy.

The accuracy of this model can further be improved by adding more strain data points in between the time steps rather than only the end of each step. The tolerance value can also be decreased at the expense of computation time.

Compared to the non-iterative strain-driven formulation, this formulation provides more robust and versatile performance, and can be used for any type of load case while the non-iterative model showed limitations in multiaxial load cases and large strains.

Regarding the simulation time, using the iterative model, it takes between 10 and 15 seconds to finish the whole 6 steps of path B analysis. This time depends on the analysis parameters such as number of substeps, number of the regions and the tolerance.

4.2.4 Ansys Implementation

The Ansys FE analyses using the implemented user-defined material subroutine based on the Likhachev's model faced convergence problem whenever the analysis passed the linear elastic

zone. The unconverged solution usually occurs when there is severe non-linearity or singularity in the element stiffness matrix, which in turn can indicate a problematic Jacobian (tangent) stiffness matrix. Looking into the tangent modulus generated throughout the analysis, it was found that the components of this matrix do indeed fluctuate during some analysis time steps. Figure 4.21 illustrates this fact more clearly, where two components of the tangent stiffness matrix are chosen and their values through the first three steps are plotted, which shows these fluctuations during the second time step. Considering the fact that during any time step the loading progression is linear and the increments within the steps are very small, any sudden change in the material behavior is unlikely, and a certain tangent stiffness components should as well be either constant or change linearly.

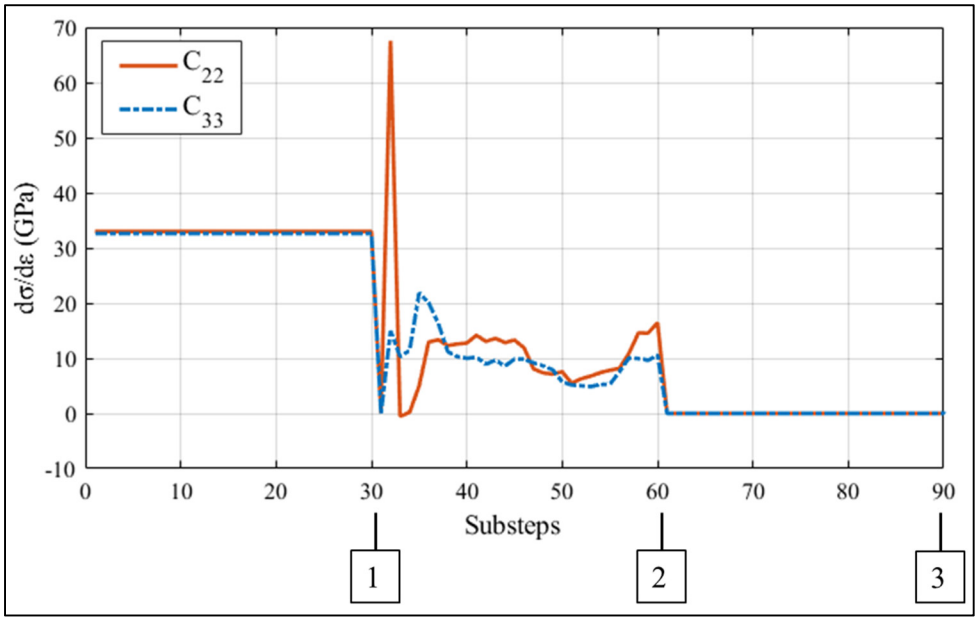

Figure 4.21 variations of tangent stiffness components C_{22} and C_{33} during the first three time steps of multiaxial load case, path B.

Taking into account the observations above one can draw the following conclusions:

- Since the same algorithm used for calculation of the main output stress tensors was used for the calculation of stress tensors resulted from the strain perturbations, these fluctuations occur only for the strain perturbations where only a single strain

component is changed while the rest of the components remain unchanged. This suggests that the fluctuations in the calculated stress components (hence the tangent modulus components should be originated from the non-unique stress values achieve through the iteration process.

- This non-unique stress results obtained from the Likhachev's model makes it a challenge to incorporate it, in its current form, into commercial FE software that usually require a tangent stiffness matrix along with the strain tensor.

4.3 Concluding Remarks

In this chapter, the Likhachev's model was studied as an alternative material model that can provide improved prediction of SMA response compared to the currently implemented material in the commercial FE software based on Auricchio's model.

Likhachev's model takes into account the crystallographic orientation of the martensite crystals by dividing the domain into a number of regions with different orientations and applying the concept of effective temperature in each region to control the martensitic transformation based on favorability of each region's orientation with respect to the state of stress. This provides a better ability to reproduce the multiaxial and path-dependent behavior of the SMAs.

This model was coded in Matlab and underwent a range of uniaxial loadings, as well as multiaxial load cases with different load paths, and its response was compared to the experimental data and the Ansys FE results with Auricchio's model. It was shown that Likhachev's model indeed predicts the multiaxial response of the NiTi SMA samples more closely compared to the Auricchio's model, although some discrepancies were still observed.

In the next part, two different approaches were presented for adapting the Likhachev's model from its original stress-driven into strain-driven formulation, which would make it suitable for FE implementation. In the first approach, a direct non-iterative reformulation of the Likhachev's model was developed which offered much faster computation, but was only

limited to uniaxial load cases. In the second approach, an iterative corrective scheme was used where the concept of a PID control function was introduced to achieve convergence. This formulation faced no limitation in terms of load cases and was able to closely track the response of the original stress-driven model.

FE programs usually require the material subroutines to provide a tangent modulus in addition to the strain tensor. An attempt was made to derive the tangent modulus. To this end, a numerical method was used where strain perturbations were applied to the model to generate the tangent modulus components at each time increment.

At the end, the iterative strain-driven form of the Likhachev's model was incorporated into the Ansys software as a material subroutine. However, FE analyses faced convergence issues. This problem was caused by some fluctuations in the tangent modulus which in turn were created due to the existence of non-unique stress values generated during the strain perturbations.

This problem signifies the fact that one should devise a mathematical scheme were the tangent stiffness matrix is derived consistently with the strain tensor which is the case with most other material models, where the tangent stiffness is derived from the underlying free energy or hardening function; see for example (Lagoudas, Hartl et al. 2012).

CONCLUSION

FE Analysis of Superelastic Lattice Structures

The purpose of the first part of this thesis was to provide a modeling and analysis framework for additively manufactured lattice structures with repeating unit cells, as the AM technologies have made it easier to produce porous parts with custom designed substructures to obtain desired mechanical behavior suited for certain applications.

FEM was used to analyze five different unit cells (spherical, diamond, TKDH, F2BCC, BCC) in Ansys with its built-in SMA material model. Since the unit cell type and porosity are the two major characteristics of the lattice structures, the impacts of these two factors on different mechanical properties were investigated which are as follows:

- Extent of reversible strain
- Apparent initial elastic modulus (EA)
- Volume fraction of transformed material in terms of austenite, martensite and mixed phases
- Strain energy absorption and dissipation

Reversible Strain: By applying the maximum reversible strain to the unit cells up to the plastic threshold, it was shown that all unit cells in all porosity levels (0 - 90%) exhibit superelastic behavior. For strut-based unit cells with porosities of 50% and below, the type of unit cell did not play a significant role in the extent of the reversible strain. However, as the porosity increases, the unit cell geometry becomes more influential.

The spherical unit cell is a special case, which has closed cell topology for lower porosities where it exhibits higher reversible strain than other strut-based unit cells but its strain tolerance significantly drops, as it becomes an open cell for porosities above 50%, where it shows the lowest strain values compared to all other unit cells. This is due to the thin walls and sharp edges around the edges of the open pores.

Apparent Elastic Modulus: Elastic modulus is an important metric in designing a porous structure. Here, the apparent elastic modulus at the beginning of the loading, representing E_A, was calculated for all unit cells in all porosities from 10 to 90%. These data provides a good comparison basis for choosing the unit cell type and porosity.

It was also shown that as the porosity increases, the range of variation of E_A between different unit cells increases exponentially. This underlines the fact that choosing the right type of the unit cell becomes increasingly important as the porosity increases, and a significant amount of material can be saved by choosing a certain unit cell type. For instance, the diamond unit cell with 80% porosity has a similar elastic modulus as a 70% BCC cell which means that 33% less material can be used.

Volume Fraction of Austenite, Martensite and Mixed phases: The percentage of the material in austenite, martensite and mixed phases were calculated based on the nodal stresses during the loading process for all unit cells and porosities.

Due to the existence of stress risers in the unit cell geometry, the material enters phase transformation at these locations much earlier than the rest of the geometry. In general, it was shown that only a small percentage of the material fully transforms into martensite, mostly well below 20%, before the maximum strain is reached. Although macroscopic superelastic response is observed, the small amount of transformation limits the superelastic behavior of the unit cell.

Strain Energy Absorption and Dissipation: Based on the apparent stress-strain curves, the strain energy absorption and dissipation were calculated. This provides useful information about the capacity of a porous material in applications such as shock absorption and vibration damping. Using an SMA in a porous structure is particularly beneficial, as it extends the range of reversible strain, hence the energy absorption. Furthermore, the hysteresis loop in the stress strain response means that the structure can dissipate far more energy in comparison to an elastic or hyperelastic material.

It was shown that addition of rounded edges to the geometry of the unit cells has a significant impact on the mechanical response of the unit cell. Since AM creates rounded edges, among other imperfections, it is of great importance to further investigate the effects of AM on the experimental results and their deviation from the simulated ones.

By investigating the dependency of the four above-mentioned mechanical parameters versus porosity and unit cell type, a designer can gain a clear picture of a suitable porous substructure that best fits a specific mechanical requirement. The set of analyses and post-processing routines presented here shall be considered as a framework, which was applied to only uniaxial loading and a select few unit cells. However, all these procedures can easily be expanded to various other loadings and unit cell types to suite a specific design requirement.

It should be noted that, since the FE simulations were carried out using Auricchio's model in Ansys, and the fact that this model was shown to have shortcomings in predicting the multiaxial and path-dependent response of SMAs, one should treat the analysis results with caution, until more accurate material models become available.

Experimental Characterization of NiTi SMA and Validation of the Material Model in the Current FE Software

In the second part of this thesis, the performance of Auricchio's material model (Auricchio, Taylor et al. 1997) was investigated which is currently implemented in commercial FE software such as Ansys and Abaqus. Specifically, the objective was to validate this model under multiaxial loading conditions with different loading paths, as the SMA used in a lattice structure undergoes three-dimensional stress states.

A series of experimental tests were carried out, where thin-walled NiTi tube samples were used and a number of uniaxial and multiaxial loadings were applied. The test results obtained from the uniaxial tests provided the material parameters required for the constitutive model in the

FE simulations. The multiaxial tests showed a clear path-dependent behavior of the NiTi SMA. The results from these tests were used for comparison against simulation results.

The FE analyses were performed in Ansys where the geometry of the test sample was created and similar load cases to that of the experimental tests were applied.

Comparing the FE analysis results with the experimental curves, it was shown that the Auricchio's model was able to predict the superelastic behavior of the SMA in uniaxial tensite test. However, this model did not provide a close prediction of the mechanical response of the material under multiaxial load cases. Furthermore, it captured only a limited amount of the path-dependent behavior observed in the experimental tests.

As several new applications of SMAs, such as porous structures, are emerging, there is an increasing need for modeling of SMA materials in complex loading conditions. A large number of constitutive models are proposed in the literature, however, their commercial use in FE software is yet to occur. This study underlines the great need for implementing a numerically efficient and more accurate model into commercial software, which could facilitate more widespread use of SMAs in the industry

An Alternative SMA material Model

In the third part of the thesis, the Likhachev's SMA model (Likhachev 1995) was investigated as a possible alternative to the Auricchio's model. This model was particularly chosen because it takes into account the crystallographic orientation of the martensite variants by introducing the concept of effective temperature and applying it to a number of regions in the domain. This model can predict main SMA behaviors such as SE, SME, TWSME and stress generation, and is also more practical as it requires few material parameters that can easily be determined through uniaxial tests.

By implementing this model in Matlab, a number of uniaxial and multiaxial load cases were tested on this model. The results were compared with the Auricchio's model against the experimental curves. It was shown that, under multiaxial load cases, Likhachev's model was able to predict the material response of the SMA more closely to the experimental curves, compared to that of the Auricchio's model.

The Likhachev's model originally has a stress-driven formulation, as it receives stress and temperature as thermomechanical loading, and calculates the strain tensor. However, FE codes usually require a material model to be in strain-driven form. Two different approaches were suggested here to adapt this model into a strain-driven formulation.

In the first approach, a direct non-iterative reformulation of the Likhachev's model was developed which offered much faster computation. However, it was functional in only uniaxial load cases.

In the second approach, an iterative corrective scheme was used where the concept of a PID control function was introduced to achieve convergence. This formulation could be used in all types of load cases without any limitations and was able to closely match the response of the original stress-driven model.

In the last part of this study, the possibility of calculating a tangent modulus (stiffness matrix) at each time increment was investigated, as this matrix is usually also required by the FE programs. Since in the original Likhachev's model the tangent modulus was not derived analytically, a numerical method was implemented here, where a series of strain perturbations were applied to the model in order to generate the tangent modulus components.

By implementing this numerical scheme in the Matlab simulations of the iterative strain-driven model, it was shown that the components of the tangent modulus fluctuate during some parts of the analysis. This indicates the existence of non-unique stress answers as a result of individual strain perturbations.

In many material models proposed in the literature, the tangent modulus is derived analytically from the underlying free energy or hardening function that defines the main behavior of the model, see for example (Lagoudas, Hartl et al. 2012). An analytical derivation of tangent modulus was not pursued in this work, however, the problem presented here highlights the need for devising a mathematical scheme in conjunction with Likhachev's model.

RECOMMENDATIONS

Based on the results obtained in this thesis, the following recommendations can be made:

1. In order to improve the modeling of porous SMAs produced by AM, it will be useful to study the impacts of manufacturing defects and imperfections in the geometry of unit cells, such as voids, uneven edges and rounded corners.

2. A material model for SMAs should be developed (or adapted) and experimentally validated so that it can predict the path-dependent mechanical response of SMAs under complex 3D stress states. This model should be strain-driven and ideally have a formulation that is not iterative.

LIST OF BIBLIOGRAPHICAL REFERENCES

Andani, M. T., et al. (2017). "Mechanical and shape memory properties of porous Ni50. 1Ti49. 9 alloys manufactured by selective laser melting." Journal of the mechanical behavior of biomedical materials **68**: 224-231.

ASTM-F2516-14 "F2516-14 (2014) Standard test method for tension testing of nickel-titanium superelastic materials." ASTM International, West Conshohocken.

Auricchio, F. (2001). "A robust integration-algorithm for a finite-strain shape-memory-alloy superelastic model." International Journal of Plasticity **17**(7): 971-990.

Auricchio, F., et al. (1997). "Shape-memory alloys: macromodelling and numerical simulations of the superelastic behavior." Computer methods in applied mechanics and engineering **146**(3): 281-312.

Azadi, B., et al. (2007). "Multi-dimensional constitutive modeling of SMA during unstable pseudoelastic behavior." International Journal of Solids and Structures **44**(20): 6473-6490.

Badiche, X., et al. (2000). "Mechanical properties and non-homogeneous deformation of open-cell nickel foams: application of the mechanics of cellular solids and of porous materials." Materials Science and Engineering: A **289**(1): 276-288.

Bansiddhi, A., et al. (2008). "Porous NiTi for bone implants: a review." Acta Biomaterialia **4**(4): 773-782.

Batdorf, S., et al. (1947). "Critical stress of thin-walled cylinders in torsion."

Betts, C., et al. (2014). "In situ microtensile testing and X-ray microtomography-based finite element modelling of open-cell metal foam struts and sandwich panels." The Journal of Strain Analysis for Engineering Design **49**(8): 592-606.

Bram, M., et al. (2011). "Mechanical properties of highly porous NiTi alloys." Journal of Materials Engineering and Performance **20**(4-5): 522-528.

Brinson, L. C., et al. (2004). "Stress-induced transformation behavior of a polycrystalline NiTi shape memory alloy: micro and macromechanical investigations via in situ optical microscopy." Journal of the Mechanics and Physics of Solids **52**(7): 1549-1571.

Chemisky, Y., et al. (2011). "Constitutive model for shape memory alloys including phase transformation, martensitic reorientation and twins accommodation." Mechanics of Materials **43**(7): 361-376.

Choi, S. and B. V. Sankar (2005). "A micromechanical method to predict the fracture toughness of cellular materials." International Journal of Solids and Structures **42**(5): 1797-1817.

Cisse, C., et al. (2016). "A review of constitutive models and modeling techniques for shape memory alloys." International Journal of Plasticity **76**: 244-284.

Comstock Jr, R., et al. (1996). "Modeling the transformation stress of constrained shape memory alloy single crystals." Acta Materialia **44**(9): 3505-3514.

Deshpande, V. and N. Fleck (2000). "Isotropic constitutive models for metallic foams." Journal of the Mechanics and Physics of Solids **48**(6): 1253-1283.

Diebels, S., et al. (2003). "Microscopic and macroscopic modelling of foams." PAMM **2**(1): 156-157.

Duerig, T., et al. (1999). "An overview of nitinol medical applications." Materials Science and` Engineering: A **273**: 149-160.

Egan, P. F., et al. (2017). "Computationally designed lattices with tuned properties for tissue engineering using 3D printing." PloS one **12**(8): e0182902.

Entchev, P. B. and D. C. Lagoudas (2002). "Modeling porous shape memory alloys using micromechanical averaging techniques." Mechanics of Materials **34**(1): 1-24.

Entchev, P. B. and D. C. Lagoudas (2004). "Modeling of transformation-induced plasticity and its effect on the behavior of porous shape memory alloys. Part II: porous SMA response." Mechanics of Materials **36**(9): 893-913.

Eshelby, J. D. (1957). The determination of the elastic field of an ellipsoidal inclusion, and related problems. Proceedings of the Royal Society of London A: Mathematical, Physical and Engineering Sciences, The Royal Society.

Evangelista, V., et al. (2010). "A 3D SMA constitutive model in the framework of finite strain." International Journal for Numerical Methods in Engineering **81**(6): 761-785.

Fazekas, A., et al. (2002). "Effect of microstructural topology upon the stiffness and strength of 2D cellular structures." International Journal of Mechanical Sciences **44**(10): 2047-2066.

Fischer, F. and K. Tanaka (1992). "A micromechanical model for the kinetics of martensitic transformation." International Journal of Solids and Structures **29**(14-15): 1723-1728.

Florence, C. and K. Sab (2006). "A rigorous homogenization method for the determination of the overall ultimate strength of periodic discrete media and an application to general hexagonal lattices of beams." European Journal of Mechanics-A/Solids **25**(1): 72-97.

Foroughi, B., et al. (2013). "Characterization and Simulation of Tensile Deformation of Non-Uniform Cellular Aluminium Until Damage." Advanced Engineering Materials **15**(4): 276-286.

Gibson, L. J. and M. F. Ashby (1999). Cellular solids: structure and properties, Cambridge university press.

Gotkhindi, T. P. and K. Simha (2015). "In-plane effective shear modulus of generalized circular honeycomb structures and bundled tubes in a diamond array structure." International Journal of Mechanical Sciences **101**: 292-308.

Grabe, C. and O. Bruhns (2009). "Path dependence and multiaxial behavior of a polycrystalline NiTi alloy within the pseudoelastic and pseudoplastic temperature regimes." International Journal of Plasticity **25**(3): 513-545.

Hartl, D., et al. (2009). "Use of a Ni60Ti shape memory alloy for active jet engine chevron application: I. Thermomechanical characterization." Smart Materials and Structures **19**(1): 015020.

Hsu, W.-N., et al. (2018). "Load path change on superelastic NiTi alloys: In situ synchrotron XRD and SEM DIC." Acta Materialia **144**: 874-883.

Huang, W. (2002). "On the selection of shape memory alloys for actuators." Materials & Design **23**(1): 11-19.

Iltchev, A., et al. (2015). "Computational homogenisation of periodic cellular materials: Application to structural modelling." International Journal of Mechanical Sciences **93**: 240-255.

Jani, J. M., et al. (2014). "A review of shape memory alloy research, applications and opportunities." Materials & Design **56**: 1078-1113.

Janus-Michalska, M. (2005). Elastic stiffness and yield strength of periodic closed-cell honeycombs. Shell Structures, Theory and Applications: Proceedings of the 8th International Conference on Shell Structures (SSTA 2005), 12-14 October 2005, Jurata, Gdansk, Poland, CRC Press.

Janus-Michalska, M. (2009). "Micromechanical model of auxetic cellular materials." Journal of Theoretical and Applied Mechanics **47**(4): 737-750.

Janus-Michalska, M. and R. Pęcherski (2003). "Macroscopic properties of open-cell foams based on micromechanical modelling." Technische Mechanik **23**(2-4): 234-244.

K.R. Mangipudi, S. W. v. B., P.R. Onck (2010). "The microstructural origin of strain hardening in two-dimensional open-cell metal foams." International Journal of Solids and Structures **47**(16): 16.

Khandelwal, A. and V. Buravalla (2009). "Models for shape memory alloy behavior: an overview of modeling approaches." The International Journal of Structural Changes in Solids **1**(1): 111-148.

Khodaei, H. and P. Terriault (2018). "Experimental validation of shape memory material model implemented in commercial finite element software under multiaxial loading." Journal of Intelligent Material Systems and Structures: 1045389X18781047.

Knowles, K. and D. Smith (1981). "The crystallography of the martensitic transformation in equiatomic nickel-titanium." Acta metallurgica **29**(1): 101-110.

Koehnen, P., et al. (2018). "Mechanical properties and deformation behavior of additively manufactured lattice structures of stainless steel." Materials & Design **145**: 205-217.

Kranz, J., et al. (2015). "Design guidelines for laser additive manufacturing of lightweight structures in TiAl6V4." Journal of Laser Applications **27**(S1): S14001.

Lagoudas, D., et al. (2012). "Constitutive model for the numerical analysis of phase transformation in polycrystalline shape memory alloys." International Journal of Plasticity **32**: 155-183.

Lagoudas, D. C., et al. (1996). "A unified thermodynamic constitutive model for SMA and finite element analysis of active metal matrix composites." Mechanics of Composite Materials and Structures **3**(2): 153-179.

Lagoudas, D. C. and E. L. Vandygriff (2002). "Processing and characterization of NiTi porous SMA by elevated pressure sintering." Journal of Intelligent Material Systems and Structures **13**(12): 837-850.

Lexcellent, C., et al. (2006). "About modelling the shape memory alloy behaviour based on the phase transformation surface identification under proportional loading and anisothermal conditions." International Journal of Solids and Structures **43**(3-4): 613-626.

Likhachev, V. (1995). "Structure-Analitycal Theory of Martensitic Unelasticity." Le Journal de Physique IV **5**(C8): C8-137-C138-142.

Liu, C. and Y. Zhang (2014). "MODELLING MECHANICAL BEHAVIOR OF ALUMINIUM FOAM UNDER COMPRESSIVE LOADING USING REPRESENTATIVE VOLUME ELEMENT METHOD."

Lu, Z. and G. Weng (1998). "A self-consistent model for the stress–strain behavior of shape-memory alloy polycrystals." Acta Materialia **46**(15): 5423-5433.

Maîtrejean, G., et al. (2013). "Density dependence of the superelastic behavior of porous shape memory alloys: Representative Volume Element and scaling relation approaches." Computational Materials Science **77**: 93-101.

Maîtrejean, G., et al. (2014). "Unit cell analysis of the superelastic behavior of open-cell tetrakaidecahedral shape memory alloy foam under quasi-static loading." Smart Materials Research **2014**.

McNANEY, J. M., et al. (2003). "An experimental study of the superelastic effect in a shape-memory Nitinol alloy under biaxial loading." Mechanics of Materials **35**(10): 969-986.

Meier, F., et al. (2014). "Numerical calculation of the tangent stiffness matrix in materials modeling." PAMM **14**(1): 425-426.

Michailidis, N., et al. (2008). "Investigation of the mechanical behavior of open-cell Ni foams by experimental and FEM procedures." Advanced Engineering Materials **10**(12): 1122-1126.

Morgan, N. (2004). "Medical shape memory alloy applications—the market and its products." Materials Science and Engineering: A **378**(1): 16-23.

Mori, T. and K. Tanaka (1973). "Average stress in matrix and average elastic energy of materials with misfitting inclusions." Acta metallurgica **21**(5): 571-574.

Murr, L. E., et al. (2012). "Next generation orthopaedic implants by additive manufacturing using electron beam melting." International journal of biomaterials **2012**.

Nemat-Nasser, S., et al. (2005). "Experimental characterization and micromechanical modeling of superelastic response of a porous NiTi shape-memory alloy." Journal of the Mechanics and Physics of Solids **53**(10): 2320-2346.

Nguyen, V.-D. and L. Noels (2014). "Computational homogenization of cellular materials." International Journal of Solids and Structures **51**(11): 2183-2203.

Niinomi, M. (2008). "Mechanical biocompatibilities of titanium alloys for biomedical applications." Journal of the mechanical behavior of biomedical materials **1**(1): 30-42.

Orgéas, L. and D. Favier (1998). "Stress-induced martensitic transformation of a NiTi alloy in isothermal shear, tension and compression." Acta Materialia **46**(15): 5579-5591.

Otsuka, K. and C. M. Wayman (1999). Shape memory materials, Cambridge university press.

Paiva, A. and M. A. Savi (2006). "An overview of constitutive models for shape memory alloys." Mathematical Problems in Engineering **2006**.

Panico, M. and L. Brinson (2007). "A three-dimensional phenomenological model for martensite reorientation in shape memory alloys." Journal of the Mechanics and Physics of Solids **55**(11): 2491-2511.

Panico, M. and L. Brinson (2008). "Computational modeling of porous shape memory alloys." International Journal of Solids and Structures **45**(21): 5613-5626.

Patoor, E., et al. (1996). "Micromechanical modelling of superelasticity in shape memory alloys." Le Journal de Physique IV **6**(C1): C1-277-C271-292.

Picornell, C., et al. (2004). "Stress-temperature relationship in compression mode in Cu-Al-Ni shape memory alloys." Materials transactions **45**(5): 1679-1683.

Popov, P. and D. C. Lagoudas (2007). "A 3-D constitutive model for shape memory alloys incorporating pseudoelasticity and detwinning of self-accommodated martensite." International Journal of Plasticity **23**(10): 1679-1720.

Ptochos, E. and G. Labeas (2012). "Elastic modulus and Poisson's ratio determination of micro-lattice cellular structures by analytical, numerical and homogenisation methods." Journal of Sandwich Structures and Materials: 1099636212444285.

Qidwai, M. and D. Lagoudas (2000). "Numerical implementation of a shape memory alloy thermomechanical constitutive model using return mapping algorithms." International Journal for Numerical Methods in Engineering **47**(6): 1123-1168.

Qidwai, M. A., et al. (2001). "Modeling of the thermomechanical behavior of porous shape memory alloys." International Journal of Solids and Structures **38**(48): 8653-8671.

Ravari, M. K. and M. Kadkhodaei (2015). "A Computationally Efficient Modeling Approach for Predicting Mechanical Behavior of Cellular Lattice Structures." Journal of Materials Engineering and Performance **24**(1): 245-252.

Reedlunn, B., et al. (2014). "Tension, compression, and bending of superelastic shape memory alloy tubes." Journal of the Mechanics and Physics of Solids **63**: 506-537.

Reyes, A., et al. (2003). "Constitutive modeling of aluminum foam including fracture and statistical variation of density." European Journal of Mechanics-A/Solids **22**(6): 815-835.

Richards, A. W., et al. (2013). "Interplay of martensitic phase transformation and plastic slip in polycrystals." Acta Materialia **61**(12): 4384-4397.

Ryhänen, J., et al. (1998). "In vivo biocompatibility evaluation of nickel-titanium shape memory metal alloy: Muscle and perineural tissue responses and encapsule membrane thickness." Journal of Biomedical Materials Research: An Official Journal of The Society for Biomaterials, The Japanese Society for Biomaterials, and the Australian Society for Biomaterials **41**(3): 481-488.

Simone, A. and L. Gibson (1998). "Effects of solid distribution on the stiffness and strength of metallic foams." Acta Materialia **46**(6): 2139-2150.

Simoneau, C., et al. (2014). "Modeling of metallic foam morphology using the Representative Volume Element approach: Development and experimental validation." International Journal of Solids and Structures **51**(21): 3633-3641.

Sittner, P., et al. (1995). "Experimental study on the thermoelastic martensitic transformation in shape memory alloy polycrystal induced by combined external forces." Metallurgical and Materials Transactions A **26**(11): 2923-2935.

Šittner, P. and V. Novák (2000). "Anisotropy of martensitic transformations in modeling of shape memory alloy polycrystals." International Journal of Plasticity **16**(10): 1243-1268.

Smith, M., et al. (2013). "Finite element modelling of the compressive response of lattice structures manufactured using the selective laser melting technique." International Journal of Mechanical Sciences **67**: 28-41.

Sonon, B., et al. (2015). "An advanced approach for the generation of complex cellular material representative volume elements using distance fields and level sets." Computational Mechanics **56**(2): 221-242.

Sullivan, R. M., et al. (2008). "A general tetrakaidecahedron model for open-celled foams." International Journal of Solids and Structures **45**(6): 1754-1765.

Terriault, P. and V. Brailovski (2011). "Modeling of shape memory alloy actuators using Likhachev's formulation." Journal of Intelligent Material Systems and Structures: 1045389X11401450.

Terriault, P. and V. Brailovski (2013). Implementation of Likhachev's model into a finite element program. Materials Science Forum, Trans Tech Publ.

Terriault, P. and V. Brailovski (2017). "Influence of boundary conditions on the simulation of a diamond-type lattice structure: A preliminary study." Advances in Materials Science and Engineering **2017**.

Thierry, B., et al. (2002). "Nitinol versus stainless steel stents: acute thrombogenicity study in an ex vivo porcine model." Biomaterials **23**(14): 2997-3005.

Thiyagasundaram, P., et al. (2011). "Fracture toughness of foams with tetrakaidecahedral unit cells using finite element based micromechanics." Engineering Fracture Mechanics **78**(6): 1277-1288.

Torra, V., et al. (2014). "On the NiTi wires in dampers for stayed cables." Smart Struct Syst **13**(3): 353-374.

Tsuda, M., et al. (2010). "Homogenized elastic–viscoplastic behavior of plate-fin structures at high temperatures: Numerical analysis and macroscopic constitutive modeling." International Journal of Mechanical Sciences **52**(5): 648-656.

Ushijima, K., et al. (2013). "Prediction of the mechanical properties of micro-lattice structures subjected to multi-axial loading." International Journal of Mechanical Sciences **68**: 47-55.

Wilkes, K. E. and P. K. Liaw (2000). "The fatigue behavior of shape-memory alloys." JOM **52**(10): 45-51.

Williams, E. and M. H. Elahinia (2008). "An automotive SMA mirror actuator: modeling, design, and experimental evaluation." Journal of Intelligent Material Systems and Structures **19**(12): 1425-1434.

Xiao, Z., et al. (2018). "Evaluation of topology-optimized lattice structures manufactured via selective laser melting." Materials & Design **143**: 27-37.

Xu, S., et al. (2016). "Design of lattice structures with controlled anisotropy." Materials & Design **93**: 443-447.

Yan, C., et al. (2012). "Evaluations of cellular lattice structures manufactured using selective laser melting." International Journal of Machine Tools and Manufacture **62**: 32-38.

Zhao, Y. and M. Taya (2007). "Analytical modeling for stress-strain curve of a porous NiTi." Journal of applied mechanics **74**(2): 291-297.

Zhu, H., et al. (1997). "Analysis of the elastic properties of open-cell foams with tetrakaidecahedral cells." Journal of the Mechanics and Physics of Solids **45**(3): 319-343.